# Characterization of Single Nanoparticles

by

Steven Jones
BSc, University of Victoria, 2015

A Thesis Submitted in Partial Fulfillment
of the Requirements for the Degree of

MASTER OF APPLIED SCIENCE

in the Department of Electrical and Computer Engineering

# Supervisory Committee

Characterization of Single Nanoparticles

by

Steven Jones
BSc, University of Victoria, 2015

**Supervisory Committee**

Dr. Reuven Gordon, (Department of Electrical and Computer Engineering)
**Supervisor**

Dr. Geoffrey Steeves, (Department of Physics and Astronomy)
**Outside Member**

# Abstract

**Supervisory Committee**
Dr. Reuven Gordon, (Department of Electrical and Computer Engineering)
**Supervisor**
Dr. Geoffrey Steeves, (Department of Physics and Astronomy)
**Outside Member**

Optical trapping is a method which uses focused laser light to manipulate small objects. This optical manipulation can be scaled below the diffraction limit by using interactions between light and apertures in a metal film to localize electric fields. This method can trap objects as small as several nanometers. The ability to determine the properties of a trapped nanoparticle is among the most pressing issues to the utilization of this method to a broader range of research and industrial applications. Presented here are two methods which demonstrate the ability to determine the properties of a trapped nanoparticle.

The first method incorporates Raman spectroscopy into a trapping setup to obtain single particle identification. Raman spectroscopy provides a way to uniquely identify an object based on the light it scatters. Because Raman scattering is an intrinsically weak process, it has been difficult to obtain single particle sensitivity. Using localized electric fields at the trapping aperture, the Raman integrated trapping setup greatly enhances the optical interaction with the trapped particle enabling the required sensitivity. In this work, the trapping and identification of 20 nm titania and polystyrene nanoparticles is demonstrated.

The second method uses an aperture assisted optical trap to detect the response of a magnetite nanoparticle to a varying applied magnetic field. This information is then used to determine the magnetic susceptibility, remanence, refractive index, and size distribution of the trapped particle.

# Table of Contents

# List of Figures

# Acknowledgments

Thank you to everyone in the lab, it has really been a pleasure to get to know you all.

I want to thank Dr. Steeves for being on my committee, as well as for his support since my undergrad. Thank you to all of the UVic physics department; from lab instructors to professors, I have always valued their devotion to the students.

A special thanks to Dr. Reuven Gordon. I sincerely appreciate the opportunities you provided me with; and have thoroughly enjoyed my time working for you.

Cheers,
Steve

Thanks to:

Daniel
Darren
Emilio
Haitian
Lewis
Ryan
Travis

# Dedication

To my parents.

# Chapter 1 – Introduction

Throughout history, humans have always used electromagnetic (EM) radiation to perceive the world. Sight, arguably the sense humans rely on most, is an evolutionary adaptation that allows the eye to detect a specific range of frequencies in the electromagnetic spectrum – *i.e.* visible light. An electromagnetic wave is an oscillation in electric and magnetic fields; this oscillation propagates forward at the speed of light ($\approx 3 \times 10^8$ m/s in vacuum). The properties of EM waves are determined by their frequency ($f$) or wavelength ($\lambda$) which are intimately tied together *via* the following equation:

$$c = \lambda f \tag{1.1}$$

Depending on the frequency/wavelength, the interactions between light and matter can vary drastically. For example, visible light consists of wavelengths on the order of $\lambda \approx 400 \times 10^{-9}$ m (violet) to $\lambda \approx 700 \times 10^{-9}$ m (red); while the EM waves used to send signals to your car radio have wavelengths on the order of $\lambda \approx 100$ m (AM radio) to $\lambda \approx 1$ m (FM radio).

For scientists, light is a particularly useful tool for probing the characteristics of a substance. Optical microscopes for instance, allow scientists to image objects that are far too small to be seen with the naked eye. In a complementary class of optical methods, known as spectroscopy, scientists can observe the response of an object to different frequencies of incident light, and ascertain the molecular structure, temperature, and other properties from this information. As technology progresses, scientists continue to probe ever smaller molecules of interest. At present, optical methods are adept at characterizing molecules as small as several microns ($\sim 10^{-6}$ m); and cutting edge research is being conducted to push these capabilities into the nano regime ($\sim 10^{-9}$ m).

The remainder of this Chapter will provide some insight into current optical techniques that are employed to characterize or observe small molecules of interest. This Chapter will also present the current limitations of the methods and where there is room for improvement. The overall goal being considered in this thesis is efficient nanoparticle detection / sensing platforms, with the ultimate intention being to present a platform that is capable of single particle sensitivity and selectivity.

## 1.1 Optical Sensing

This Section introduces some notable label free optical techniques that are commonly used for sensing nanoscale particles. These techniques are, in general, complementary with respect to the properties of the analyte that the methods are able to resolve.

### 1.1.1 Dynamic Light Scattering

Dynamic light scattering is a method that uses fluctuations in the scattered intensity of coherent monochromatic light by an ensemble of small particles to determine the diffusion coefficient, and size distribution of the particles[1–4]. For particles much smaller than the wavelength of the incident light, the radiation scattered by the particle is effectively isotropic[3]. As a result, the intensity as measured at a specific scattering angle is dependent on the position of all of the particles involved. Over time the measured intensity of light will fluctuate due to changes in the position of the particles which is caused by Brownian motion. By taking the autocorrelation of the scattered intensity, the rate of Brownian motion can be determined. For a dilute solution of disperse nanoparticles the time constant of the exponential decay of the autocorrelation signal is inversely proportional to the diffusion coefficient, which is itself inversely proportional to the radius of the particle[3–6].

Dynamic light scattering is a useful technique to characterize the physical properties of a solution of nanoparticles in an *in situ* environment. By modifying the experiment, this technique can easily be extended to measured temperature effects on the diffusion coefficient, as well as to determine the extent of particle aggregation over time. While useful, this method requires a large amount of *a priori* knowledge of the particles being measured and their surrounding environment. Additionally, because the method relies on the intrinsic Brownian motion of the particles, dilute concentrations must be used so that interparticle collisions do not dominate particle motion. This method is not applicable to single particles.

### 1.1.2 Surface Plasmon Resonance Sensors

When monochromatic light in the visible frequency range interacts with the interface between a noble metal and a dielectric, surface waves of charge density oscillations are able to propagate[7,8]. These surface waves are known as surface plasmon polaritons. The coupling condition required for the formation of a surface wave is extremely sensitive to the electrical permittivity of the surrounding dielectric (typically a liquid)[7,9]. Changes in the coupling condition can be detected as a shift in the absorption spectra of the incident light – typically in terms of angle of incidence for monochromatic light, or in terms of wavelength for a fixed angle of incidence[10–14]. The most common form of this type of sensor is called the Kretschmann configuration, show in Figure 1.

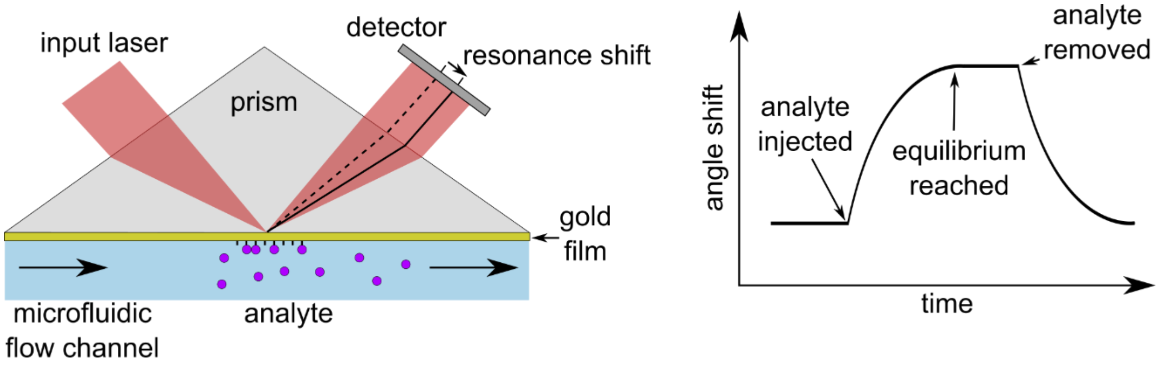

**Figure 1** – Kretschmann configuration of a surface plasmon resonance sensor. Left: schematic diagram of the measurement apparatus. Monochromatic light is focused onto a thin gold film *via* a prism. Surface plasmons are excited for a specific angle of incidence corresponding to an absorption peak as measured by the detector. As the analyte bonds to the functionalized surface of the gold, the effective index of the dielectric changes causing a shift in the plasmon resonance. Right: the angle of incidence corresponding to surface plasmon excitation as a function of time as the analyte if injected into the channel, saturates the sensing region, and is subsequently removed.

In the Kretschmann configuration a monochromatic light source is used to illuminate a thin noble metal film (typically gold) at a variety of angles of incidence. The coupling condition in this neutral configuration results in a narrow range of angles of incidence being absorbed by the metal in the form of a surface plasmon. In the typical implementation, the surface of the gold on the side of the microfluidic flow channel is functionalized to promote the desired analyte to bind to the surface. As the concentration of the analyte in the flow channel is increased, the binding rate to the surface also increases resulting in a change in the effective permittivity of the dielectric. This change in permittivity alters the coupling condition and results in a shift of the absorption spectrum (see Figure 1 right). As more analyte is flowed into the channel, the interaction between analyte and functionalized gold surface will reach equilibrium where binding and unbinding events occur at the same rate. Following this period, the analyte will be flushed out of the channel and the system is reset.

Because of the ability of this method to easily probe the binding affinity between the analyte and the functionalization of the surface, it has found a plethora of applications within biology[15–18]. Surface plasmon resonance based sensors are a simple and relatively cheap testing apparatus. The method is often employed on ensembles; however recent advances in the field have shown the potential for single particle sensitivity[19]. Despite the high level of sensitivity and simple implementation, this method suffers from a lack of selectivity in terms of its ability to isolate single molecules for individual analysis.

### 1.1.3 Spectroscopy

Spectroscopy is an extremely useful and broad sensing technique that can provide complex information about the energy states of a molecule. Light interacting with a molecule will cause transitions between energy states which affects the transmitted or scattered signal. The energy of a molecule is defined by the electric, vibrational, and rotational energy states in descending order of energy magnitude. Probing the electronic energy states can provide information about the bonding between atoms in a molecule; while probing the vibrational states details the molecular structure and can act as a unique spectral fingerprint. For the purpose of this thesis the scope will be restricted to spectroscopic techniques that probe the vibrational modes of a molecule.

The energy of vibrational transitions in molecules typically corresponds to optical frequencies in the infrared region[20]. The two main spectroscopic methods used to probe the vibrational modes of molecules are infrared (IR) spectroscopy, and Raman spectroscopy. In IR spectroscopy a broad spectrum of IR light is radiated towards the analyte. The frequencies of light which correspond to vibrational transitions will be absorbed by the molecules and appear as absorption peaks in the transmission spectra. In Raman spectroscopy a monochromatic source is used to excite the analyte. Some of the scattering events will cause vibrational transitions and therefore the scattered light will gain or loose energy accordingly. These scatting events corresponds to spectral peaks that are shifted relative to the excitation frequency. While both IR and Raman spectroscopy deal with vibrational energy states they are in fact complimentary as certain vibrational modes are IR active while others are Raman active (and some are active in both)[20,21]. A more detailed investigation of the phenomena involved in Raman scattering is presented in Section "2.5 Raman Spectroscopy".

Spectroscopy is an incredibly powerful technique in terms of the amount of information it can provide; however, it is also often a relatively weak process. Particularly in the case of nanoparticles, where the analyte is significantly smaller than the wavelength of incident light and the interaction cross section becomes quite small. As a result, spectroscopic techniques have typically been employed on ensembles. Modern advances to these techniques will be discussed in the following Section which show the ability to reach single particle sensitivity.

## 1.2 Nanostructured Enhancements

Presented here are current methodologies being employed to improve the abilities of some of the aforementioned optical sensing techniques. These methods primarily utilize nanostructures in noble metals to cause extreme electric field localization. This Section serves to present the current state of a select group of optical techniques which are progressing towards the ultimate limit of single particle sensitivity and selectivity. For a more thorough description of the interaction between electromagnetic waves and metal/dielectric interfaces see Section "2.3 Plasmons".

### 1.2.1 Localised Surface Plasmon Resonance Sensors

Similar to the surface waves that were described in Section "1.1.2 Surface Plasmon Resonance"; metallic nanoparticles can also exhibit plasmonic resonances. These plasmonic resonances create intense electric field enhancements and simultaneously localize the electric field to small, subwavelength regions. A more thorough description of this phenomenon is presented in Section "2.3.2 Localized Surface Plasmons Resonances". Because of these resonances, the metallic nanoparticles are extremely susceptible to changes in their surrounding and can be implemented as an effective small area sensing platform. The basic design of such a sensing apparatus is presented in Figure 2.

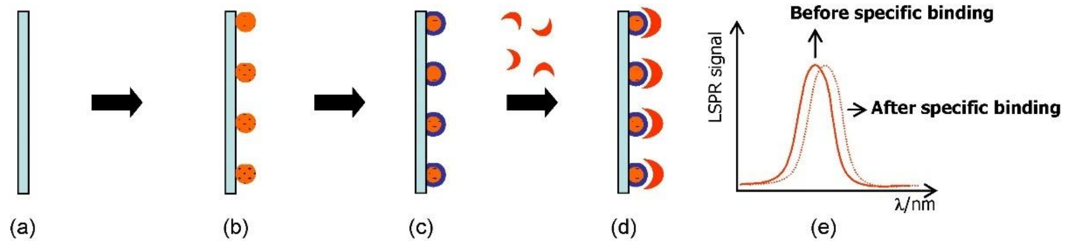

**Figure 2** – Diagram illustrating the preparation and operation of a localized surface plasmon resonance (LSPR) based biosensor based on changes in the surrounding dielectric permittivity. a) and b) metal nanoparticles are deposited onto a substrate. c) nanoparticles are functionalized to bind with desired analyte. d) analyte binds to nanoparticles causing a frequency shift in the plasmonic resonance – shown in e). This figure has been reprinted with permission from[22].

Recent advances in nanofabrication technologies have enabled advanced shapes such as stars or pyramids to be utilized for plasmonic resonance based sensing applications[23–26]. These complex nanoparticle shapes permit even larger electric field enhancements and localization. This technique is of current interest for biological applications due to its high sensitivity and low sample volume required[22,27]. These devices have been shown to detect analytes with extremely low concentrations in the nanomolar or subnanomolar ranges[28,29]. The small concentration and potential for single particle sensitivity make LSPR based sensing devices an intriguing technology for investigating small molecule interactions. Recent demonstrations of single biological particle detection with surface plasmon resonance based sensors include the detection of viruses and virus like particles[30–33], and the detection of DNA functionalized gold nanoparticles[19,34].

### 1.2.2 Surface Enhanced Raman Spectroscopy

Similar to the other methods presented in this Section, the field localization caused by plasmonic effects can also increase the intensity of the intrinsically weak Raman scattering signal[20,35,36]. Because of the small particle sizes with respect to the excitation light, the Raman scattering cross section is particularly small for low concentration nanoparticle analytes. By using nanostructured metals, plasmonic effects can increase the interaction between the electric field and the analyte. This effect is enhanced further if the particle can be localized to the immediate vicinity of the electric field enhancement. A more detailed explanation of the phenomenon is presented in Section “2.5.1 Surface Enhanced Raman Spectroscopy”. Recent works have demonstrated nanoplasmonic platforms that increase the Raman interaction, resulting in a single particle sensitivity[37].

### 1.2.3 Extraordinary Optical Transmission

For a periodic array of nanoapertures in a thin metal film, at certain frequencies the transmission through the array is much greater than predicted by classical electromagnetism[38,39]. This phenomena, known as extraordinary optical transmission (EOT), has been directly observed to occur as the result of plasmonic effects[40]. The spectral location of the transmission resonances is defined by the periodicity of the arrays[41]. The ability to tune the transmission properties of the array makes EOT based sensing platforms an intriguing option for nanoscale optical sensing. Past works have shown the ability for these structures to be employed in refractive index sensing (*i.e.* SPR)[42,43], as well as in spectroscopic applications[44–46].

## 1.3 Optical Trapping

In order to isolate a single particle (single particle selectivity), a method has been developed that uses purely optical forces to manipulate small particles, *i.e.* optical trapping[47]. The physical phenomena that govern this process are detailed in Section “2.2 Rayleigh Scattering” and Section “2.4 Optical Trapping”. Due to the minute nature of optical forces, this method has historically been relegated to the micro regime. This is due to the fact that micron sized particles are small enough to be easily influenced, yet large enough to interact strongly with light. It is currently of great interest to advance the method of optical trapping towards the nanoscale. For the purposes of this work, focus is placed on the forefront of this research field as it applies to objects with nanoscale dimensions.

The method of optical trapping has been used to investigate the Brownian motion of trapped nanoparticles[48], plasmonic coupling between gold nanospheres[49], and nonlinear trapping effects from optical forces[50]. Optical traps have also been demonstrated to directly manipulate nanostructures; one example is an optically driven rotary motor that is capable of spinning at frequencies up to 42 kHz[51]. Trapped particles can also be optically excited such as the generation of unconverted photons from $KNbO_3$ nanowires[52]. By using multiple trapping frequencies, optical trapping setups have been used to passively sort gold nanoparticles based on their size[53]. In biological applications, low power optical traps have been utilized to observe single molecule protein binding kinetics, and probe low frequency vibrational modes of proteins[54,55]. Perturbations of the method have also been developed, such as holographic optical traps and optoelectronic traps, which demonstrate the ability for high throughput nanoassembly and fabrication[56,57].

## 1.4 Contributions of this Thesis

In this thesis, work is presented which simultaneously demonstrates single particle sensitivity and isolation, allowing for data to be obtained from an individual analyte nanoparticle. Building on prior experiments, which have used the method of aperture assisted optical trapping to manipulate and detect small objects, presented here are two new methods that are able to independently determine the characteristic properties of an isolated nanoparticle. In the first work, an apparatus is developed which looks at the reflection of light by a nanoparticle to obtain information about the vibrational modes of its constituent molecules. In this way, a “spectral fingerprint” of the molecule is obtained, this enables the unique identification of the molecular structure of the particle. In the second method, a superparamagnetic nanoparticle is subjected to varying applied magnetic fields while in an optical trap. By observing the response of the particle to the applied magnetic field, the complex refractive index, magnetic susceptibility, remanence, and size distribution can be determined. The methods presented here allow researchers new avenues to identify and characterize individual nanoparticles in a label free method with a minimum of *a priori* knowledge of the properties of the analyte.

The following Chapter will build the necessary theoretical foundation required to understand the experimental results presented in this work. Following the theory, an outline of the techniques used in aperture assisted trapping will be detailed. In Chapter 4 and 5, two methods for label free characterization of individual nanoparticles will be presented. Chapter 4 deals specifically with an experimental demonstration of plasmon enhanced Raman spectroscopy on an individually trapped nanoparticle; the spectra for two different material nanoparticles is presented. In Chapter 5, the method of optical trapping magnetic field (OTMF) is reported. In OTMF an external magnetic field is applied to a trapped magnetic nanoparticle, by varying the magnetic field and observing the influence on the trapped particle, characteristic properties of the magnetic nanoparticle are ascertained. Following the conclusion (Chapter 6), a brief forecast on the future of aperture assisted trapping is discussed is Chapter 7.

# Chapter 2 – Theory

## 2.1 Introduction

In this Chapter the underlying principles of the techniques used in this work will be described. The ultimate goal is to outline how optical methods can be used to isolate and characterize nanoparticles. Optical trapping is a method that uses the intensity profile of light to manipulate small objects. This phenomenon is based on the conservation of momentum that occurs as light is scattered by a particle; and by the relationship between the optical response of the particle and that of the surrounding medium (characterized by the dielectric permittivity). The interaction between light and subwavelength particles is described in Section “2.2 Rayleigh Scattering”.

In Section “2.3 Plasmons,” the interaction between light and noble metals at optical frequencies will be detailed. The interesting features of this interaction results from charge density oscillations on a metal’s surface and are influenced by the surrounding dielectric. Extreme field localization is associated with plasmon oscillations which can be further enhanced by small metallic particles and structures. The effects of these plasmon resonances are integral to the aperture assisted trapping works presented here.

Section “2.4 Optical Trapping” presents the basic principles of optical trapping and how this phenomenon can be understood. In order to trap dielectric nanoparticles, complimentary methods must be employed. Such methods include aperture assisted trapping which can be visualized by analysing Bethe’s theory of transmission through small holes.

Finally, in Section “2.5 Raman Spectroscopy,” a method of using the scattering of light by a molecule as a spectral fingerprint is analyzed. This form of spectroscopy is based on transitions between the vibrational modes of a molecule. Raman spectroscopy allows scientists to noninvasively identify the molecular structure of a particle based on the scattered light. This spectral fingerprint is an extraordinarily useful technique and its efficiency can be greatly enhanced by using plasmons to localize the electric field to subwavelength dimensions.

## 2.2 Rayleigh Scattering

Rayleigh scattering is a domain of electromagnetic theory that is concerned with the interaction of light with subwavelength particles, specifically for elastic scattering events (as opposed to inelastic scattering such a Raman scattering as described in “2.5 Raman Spectroscopy”). In the context of optical trapping there are two main components of optical forces that must be considered: scattering force, and gradient force. Using Rayleigh scattering theory this thesis will outline how optical forces act on small dielectric spheres as an illustrative example for how light can be used to manipulate subwavelength particles.

### 2.2.1 Scattering Force

Consider a small sphere which is illuminated by a collimated beam of monochromatic, linearly polarized light. In the case where the sphere is small enough, at any instant in time the electric field surrounding the sphere is approximately constant across its volume. This approximation implies that the interaction is effectively electrostatic in nature. The sphere becomes polarized as the electrons are displaced from their equilibrium position around their respective nuclei. In this case the interior of the sphere experiences a uniform electric field (see Figure 3) according to:[58]

$$E_{\text{internal}} = \left(\frac{3\epsilon_{\text{particle}}}{\epsilon_{\text{particle}} + 2\epsilon_{\text{med}}}\right)E_0 \tag{2.2.1}$$

Here, $E_0$ is the amplitude of the incident electric field and $E_{\text{internal}}$ is the amplitude of the electric field within the sphere. $\epsilon_{\text{med}}$ and $\epsilon_{\text{particle}}$ are the dielectric permittivities of the surrounding medium and sphere respectively.

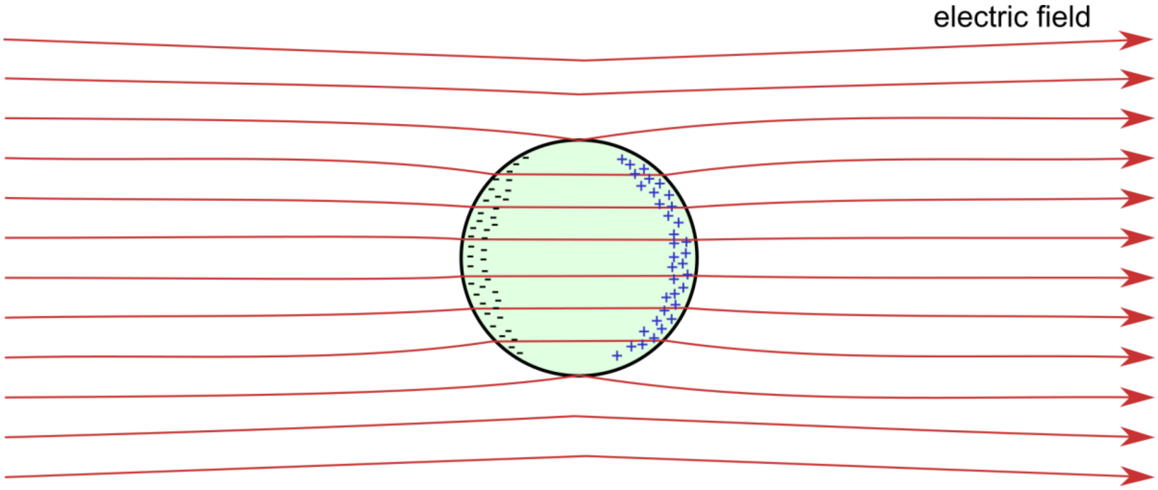

**Figure 3** – Dipole moment induced in a subwavelength dielectric sphere by an applied electric field. Notice the electric field lines are parallel within the sphere, *i.e.* constant E-field.

The displacement of the electrons within the sphere from their equilibrium positions' results in an induced dipole moment of the sphere. The external electric field is a superposition of the field in the absence of the sphere, and the field radiating from an electric dipole placed at the centre of the sphere. The dipole moment induced in the sphere is given by[59]

$$p = \alpha E_0 \quad \text{where} \quad \alpha = 4\pi\epsilon_{\text{med}} r^3 \left(\frac{\epsilon_{\text{particle}} - \epsilon_{\text{med}}}{\epsilon_{\text{particle}} + 2\epsilon_{\text{med}}}\right) \tag{2.2.2}$$

Here, $p$ is the dipole moment induced in a dielectric sphere of radius $r$, and $\alpha$ is the polarizability of the sphere. For an applied electric field oscillating in a sinusoidal fashion, the dipole moment of the spherical dielectric particle acts as an electric dipole oscillating at the frequency of the incident light. The scattering intensity is given by:[58]

$$I = \frac{16\pi^4 r^6}{R^2\lambda^4}\left(\frac{\epsilon_{\text{particle}} - \epsilon_{\text{med}}}{\epsilon_{\text{particle}} + 2\epsilon_{\text{med}}}\right)^2 \sin^2(\theta) I_0 \qquad (2.2.3)$$

Where $R$ is the distance from the centre of the sphere (dipole) to the point where the intensity is measured, and $\theta$ is the angle between the vector $\vec{R}$ and the axis of electric polarization (see Figure 4).

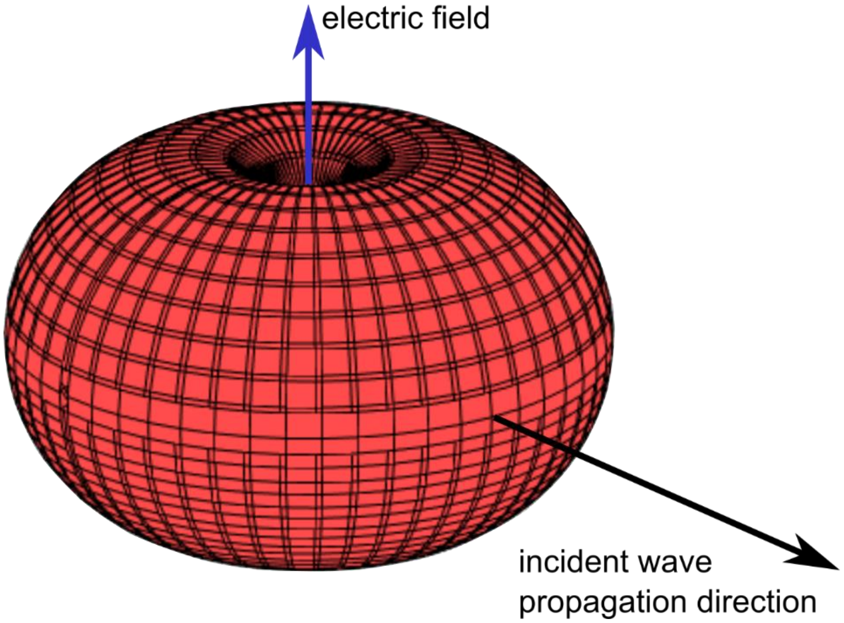

**Figure 4** – Radiation pattern of dielectric sphere (dipole). The radial distance from any point on the surface of the wavefront (red surface) to the origin, is proportional to the intensity scattered in that direction.

By integrating equation 2.2.3 over the surface of a sphere of radius $R > r$ we can obtain the total power radiated by the sphere, *i.e.*

$$\boldsymbol{P}_{\text{scattered}} = \int I \cdot dS_r = \int_0^{2\pi}\int_0^{\pi} \frac{16\pi^4 r^6}{R^2\lambda^4}\left(\frac{\epsilon_{\text{particle}} - \epsilon_{\text{med}}}{\epsilon_{\text{particle}} + 2\epsilon_{\text{med}}}\right)^2 \sin^2(\theta) I_0 \cdot R^2 \sin(\theta) d\theta d\phi$$

$$\boldsymbol{P}_{\text{scattered}} = \frac{128\pi^5 r^6}{3\lambda^4}\left(\frac{\epsilon_{\text{particle}} - \epsilon_{\text{med}}}{\epsilon_{\text{particle}} + 2\epsilon_{\text{med}}}\right)^2 I_0 \tag{2.2.4}$$

Under this electric dipole approximation, the scattered power is radiating isotropically. As a result, the total flux pattern of electromagnetic radiation has changed. Conservation of momentum thus requires that the particle move in parallel with the initial path of the light. The force acting on the particle due to scattering is[59–61]

$$F_{\text{scattered}} = \frac{\sqrt{\epsilon_{\text{med}}/\epsilon_0}}{c} \cdot \boldsymbol{P}_{\text{scattered}} \tag{2.2.5}$$

$$F_{\text{scattered}} = \frac{128\pi^5 r^6}{3\lambda^4}\frac{\sqrt{\frac{\epsilon_{\text{med}}}{\epsilon_0}}}{c}\left(\frac{\epsilon_{\text{particle}} - \epsilon_{\text{med}}}{\epsilon_{\text{particle}} + 2\epsilon_{\text{med}}}\right)^2 I_0 \tag{2.2.6}$$

Or as it is more colloquially written, in terms of the refractive index:

$$F_{\text{scattered}} = \frac{128\pi^5 r^6}{3\lambda^4}\frac{n_{\text{med}}}{c}\left(\frac{m^2 - 1}{m^2 + 2}\right)^2 I_0 \quad \text{where} \quad m = \frac{n_{\text{particle}}}{n_{\text{med}}} = \sqrt{\frac{\epsilon_{\text{particle}}}{\epsilon_{\text{med}}}} \tag{2.2.7}$$

The important factor to observe here is that the scattering pressure (force per unit area) is proportional to the incident intensity, and to $(r/\lambda)^4$. This implies that as the particles radius is scaled below the wavelength of incident light, the magnitude of the scattering force will diminish rapidly.

### 2.2.2 Gradient Force

Continuing with the Rayleigh description of light interacting with subwavelength particles, we can investigate how the induced dipole moment of the particle interacts with the intensity distribution of light, known as the gradient force. The force that the particle experiences is ultimately the Lorentz force, *i.e.*[62,63]

$$F = (p \cdot \nabla)E + \frac{dp}{dt} \times B \quad \text{with} \quad p = \alpha E \tag{2.2.8}$$

$$F = \alpha\left((E \cdot \nabla)E + \frac{\partial E}{\partial t} \times B\right) \tag{2.2.9}$$

To realize this relationship in a more descriptive form we use the following vector identity in conjunction with Faraday's law from Maxwell's equations[63]

$$\nabla(A \cdot B) = A \times (\nabla \times B) + B \times (\nabla \times A) + (A \cdot \nabla)B + (B \cdot \nabla)A \tag{2.2.10}$$

with $A = B = E$ this becomes:

$$\frac{1}{2}\nabla E^2 = E \times (\nabla \times E) + (\mathrm{E} \cdot \nabla)\mathrm{E} \tag{2.2.11}$$

$$\text{Faraday's law} \quad \nabla \times E = -\frac{\partial B}{\partial t} \tag{2.2.12}$$

Using Faraday's law and the above vector identity, the force on the particle can be simplified to

$$F = \frac{1}{2}\alpha\nabla E^2 + \alpha\frac{\partial}{\partial t}(E \times B) \tag{2.2.13}$$

By taking the time average of the above expression we get

$$F_{\mathrm{grad}} = \langle F \rangle = \frac{1}{4}\alpha\nabla|E|^2 + \alpha\mu_0\frac{\partial I_0}{\partial t} \tag{2.2.14}$$

For the case of time-constant optical intensities, this reduces to[61]

$$F_{\mathrm{grad}} = \frac{1}{4}\alpha\nabla E^2 \quad \text{with} \quad \alpha = 4\pi\epsilon_{\mathrm{med}}r^3\left(\frac{\epsilon_{\mathrm{particle}} - \epsilon_{\mathrm{med}}}{\epsilon_{\mathrm{particle}} + 2\epsilon_{\mathrm{med}}}\right) \tag{2.2.15}$$

This formula describes the way in which a subwavelength particle responds to spatially varying electric field intensity distributions. The term in brackets in the polarizability expression (equation 2.2.14) is known as the Clausius-Mossotti factor and illustrates how the polarizability of a particle is influenced by the surrounding medium. For the case of a dielectric particle with higher relative permittivity, the gradient force acts to pull the particle to regions of higher electric field intensities. This situation can be thought of as a particle of higher optical density being swept towards higher electric fields, while less optically dense materials are expelled from those regions. From the analytical form of the gradient force, we can see that it is proportional to the third power of the particles radius. When compared to the scattering force, which is proportional to the sixth power of the particles radius (and inversely proportional to the fourth power of the wavelength) we can see that for deeply subwavelength particles, the gradient force becomes dominant.

## 2.3 Plasmons

The field of plasmonics is relatively new, having only been developed into its current form around the 1970's[64]. The effects of plasmonics however, have been observed for centuries, with artists incorporating trace amounts of metallic nanoparticles into glass to create unique and visually stunning effects[65] (see Figure 5). In its essence, plasmonics is a theory which describes collective electron density oscillations in a noble metal under the influence of electromagnetic radiation. The first experimental observation of plasmonic effects took place in 1902 when examining the diffraction of light by metal grating, a phenomena which could not be explained for more than half a century[65,66]. Since its initial development the field of plasmonics has matured into an extensive engineering and research area which describes the unique electric field distributions that occur at metal-dielectric interfaces around the visible frequency range[67–70].

**Figure 5** – Lycurgus cup, a Roman artifact dating back to the 4th century AD. The glass contains trace amount of silver and gold nanoparticles which exhibit plasmon resonances, thereby affecting the transmission and reflection of light. The image on the left shows the cup transmitting light, while the figure on the right is viewed mainly through reflection. Reprinted with permission from[71].

To understand plasmonic interactions we must first describe the way in which a noble metal optically responds to light as a function of frequency. Specifically, we must define the permittivity $\epsilon(\omega)$ as a function of frequency. In order to describe the permittivity, we start our analysis by considering the free electron gas model of noble metals. In this approximation the electron motion is defined by the following second degree differential equation[7]

$$m\frac{d^2x}{dt^2}+m\gamma\frac{dx}{dt}=-eE \tag{2.3.1}$$

Where $m$ is the mass of the electrons, $x$ is their position, $\gamma$ is a damping factor resulting from collisions, $e$ is the charge of an electron, and $E$ is the applied electric field. By assuming the form for the applied electric field, *i.e.* $E(t) = E_0\mathrm{e}^{-i\omega t}$, the motion of electrons can be written as

$$x(t) = \frac{e}{m(\omega^2 + i\gamma\omega)} E_0 \mathrm{e}^{-i\omega t} \tag{2.3.2}$$

The polarization density ($P = qd$) can then be described by

$$P = -Nex = -\frac{Ne^2}{m(\omega^2 + i\gamma\omega)} E \tag{2.3.3}$$

Here, $N$ is the density of electrons. The displacement field in this case becomes

$$D = \epsilon_0 E + P = \epsilon_0 \left(1 - \frac{\omega_p^2}{\omega^2 + i\gamma\omega}\right) E \quad \text{with} \quad \omega_p = \sqrt{\frac{Ne^2}{\epsilon_0 m}} \tag{2.3.4}$$

The constant $\omega_p$ is known as the plasma frequency. Using an alternate definition for the displacement field, $D = \epsilon_0 \epsilon_r(\omega) E$, we define the dielectric function of this free electron gas

$$\epsilon_r(\omega) = 1 - \frac{\omega_p^2}{\omega^2 + i\gamma\omega} \tag{2.3.5}$$

For real metals, the above relation must be adjusted to account for the response to frequencies much greater than the plasma frequency[7], *i.e.*

$$\epsilon_r(\omega) = \epsilon_\infty - \frac{\omega_p^2}{\omega^2 + i\gamma\omega} \tag{2.3.6}$$

Here we have arrived at the Drude model for the dielectric response of a metal which is our starting point for the investigation of plasmonic effects.

The simplest type of plasmonic resonance is called a volume plasmon and is possible for the case of a free electron gas with negligible damping. At the plasma frequency the dielectric response of an ideal metal is exactly zero (*i.e.* $\epsilon_r(\omega_p) = 0$ for $\gamma = 0$). Therefore, the displacement field is also zero causing the polarization and electric field to be related by:

$$P = -\epsilon_0 E \quad \text{or} \quad E = -\frac{P}{\epsilon_0} \tag{2.3.7}$$

In other words, the field induced within the material is a pure depolarization field and the collective charge density oscillations of the electron gas are exactly out of phase with the incident electric field.

### 2.3.1 Surface Plasmon Polaritons

A more interesting and useful example of plasmon oscillations occurs at the interface between a metal and a dielectric. In this situation photons can be coupled to plasma oscillations in the metal allowing a type of surface wave to propagate[7]. To start our analysis we first present Maxwell's equations in their differential form, *i.e.*[63]

$$\text{Gauss' law} \quad \nabla \cdot D = \rho_{ext} \tag{2.3.8a}$$

$$\text{no name} \quad \nabla \cdot B = 0 \tag{2.3.8b}$$

$$\text{Faraday's law} \quad \nabla \times E = -\frac{\partial B}{\partial t} \tag{2.3.8c}$$

$$\text{Ampere's law with Maxwell's correction} \quad \nabla \times H = J_{ext} + \frac{\partial D}{\partial t} \tag{2.3.8d}$$

Where $D = \epsilon_0 E + P$. By assuming no external charges or currents ($\rho = 0,\ J = 0$) and combining the curl equations with the vector identity $\nabla \times \nabla \times E = \nabla(\nabla \cdot E) - \nabla^2 E$ (equation 2.2.10) we obtain:

$$\nabla\left(-\frac{1}{\epsilon} E \cdot \nabla\epsilon\right) - \nabla^2 E = -\mu_0 \epsilon_0 \epsilon_r \frac{\partial^2 E}{\partial t^2} \tag{2.3.9}$$

If the permittivity is translationally invariant (*i.e.* $\nabla\epsilon = 0$) this results in the standard wave equation for electromagnetism[7]

$$\nabla^2 E = \frac{\epsilon}{c^2}\frac{\partial^2 E}{\partial t^2} \tag{2.3.10}$$

By assuming the form of the applied electric field as a plane wave (*i.e.* $E \sim \mathrm{e}^{-i\omega t}$) and making use of the definition for the wave vector ($k_0 = 2\pi/\lambda_0 = \omega/c$) then the wave equation simplifies to:

$$\nabla^2 E + \epsilon k_0^2 E = 0 \tag{2.3.11}$$

To investigate the electromagnetic interactions at a metal-dielectric interface we define a system with light propagating in the x-direction, and where a metal exists for all $z < 0$ ($\epsilon_r$ defined by Drude model), and a dielectric for all $z > 0$ ($\epsilon_r =$ constant). The z-component of the wave equation is

$$\frac{\partial^2 E}{\partial z^2} + k_z^2 E = \frac{\partial^2 E}{\partial z^2} + (\epsilon k_0^2 - k_x^2)E = 0 \tag{2.3.12}$$

We can also now write Faraday's law and Ampere's law from Maxwell's equations as

$$\nabla \times E = i\omega\mu_0 H \quad \text{and} \quad \nabla \times H = -i\omega\epsilon_0\epsilon_r E \tag{2.3.13}$$

Note that by virtue of the problem definition, the system is translationally invariant along the y-axis, and therefore all derivatives with respect to $y$ are exactly zero. For this system of equations there are two forms of the solution, one corresponding to TM propagating waves where $E_x, E_z,$ and $H_y$ are all non-zero, and another for TE propagating waves with $H_x, H_z,$ and $E_y$ all non-zero. For the case of TE polarization it can be shown that no surface modes exist and thus for the study of surface plasmon polaritons we will restrict further analysis to the TM case[7].

For TM propagating waves, the system is defined by the following equations

$$\frac{\partial^2 H_y}{\partial z^2} + (\epsilon k_0^2 - k_x^2)H_y = 0 \tag{2.3.14a}$$

$$E_x = -\frac{i}{\omega\epsilon_0\epsilon_r}\frac{\partial H_y}{\partial z} \tag{2.3.14b}$$

$$E_z = -\frac{k_x}{\omega\epsilon_0\epsilon_r}H_y \tag{2.3.14$c$}$$

Solving the above equations and then applying boundary conditions at $z = 0$ we obtain

$$H_y = C_0\mathrm{e}^{i(k_x x - k_z z)} \tag{2.3.15a}$$

$$E_x = C_0\frac{ik_z}{\omega\epsilon_0\epsilon_r}\mathrm{e}^{i(k_x x - k_z z)} \tag{2.3.15b}$$

$$E_z = -C_0\frac{k_x}{\omega\epsilon_0\epsilon_r}\mathrm{e}^{i(k_x x - k_z z)} \tag{2.3.15c}$$

It is important to note that both $\epsilon_r$ and $k_z$ are functions of $z$ and have a discrete discontinuity at the boundary $z = 0$. Explicitly, for the problem defined here this implies

$$\epsilon_r(z < 0) = \epsilon(\omega) \quad \text{(Drude model)}$$

$$\epsilon_r(z > 0) = \text{constant}$$

$$k_{z,z<0} = \sqrt{\epsilon_{r,z<0}k_0^2 - k_x^2} \tag{2.3.16a}$$

$$k_{z,z>0} = \sqrt{\epsilon_{r,z>0}k_0^2 - k_x^2} \tag{2.3.16b}$$

$$\frac{k_{z,z<0}}{k_{z,z>0}} = -\frac{\epsilon_{r,z<0}}{\epsilon_{r,z>0}} \tag{2.3.16c}$$

Using these results we are able to obtain the dispersion relation for surface plasmons at this metal dielectric interface (see Figure 6).

$$k_x = k_0\sqrt{\frac{\epsilon_a\epsilon_b}{\epsilon_a + \epsilon_b}} \tag{2.3.17}$$

Where $\epsilon_a$ and $\epsilon_b$ are the relative permittivities of the materials for $z < 0$ and $z > 0$ respectively (note that $\epsilon_a = \epsilon_{r,z<0}(\omega)$ is frequency dependent).

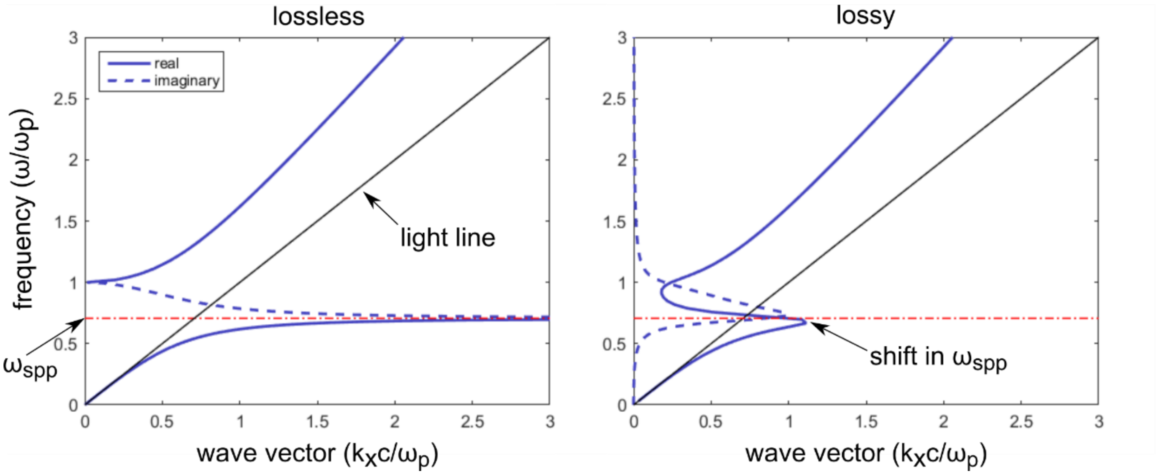

**Figure 6** – Dispersion relation for metal-dielectric interface using the Drude model[7] ($\epsilon_\infty = 1$, $\epsilon_{r,z>0} = 1$). Left figure indicates the ideal lossless case, while the figure on the right includes losses ($\gamma = 0.1$). The solid blue lines correspond to the real part of the propagation wave vector while the dashed blue lines are the imaginary part. The red line indicates the lossless surface plasmon polaritons frequency, and the solid black line is the light line showing the dispersion relation for a plane wave propagating in a vacuum ($\epsilon_r = 1$).

Figure 6 shows the relation between the propagation wave vector ($k_x$) and the applied electromagnetic frequency relative to the plasma frequency. At the resonance frequency of equation 2.3.17, waves are able to propagate with a disproportionately large wave vector along the metal-dielectric interface. As this surface plasmon wave propagates, the electric field intensity is confined close to the surface of the metal. For frequencies significantly above the plasma frequency the metal acts as a dielectric.

### 2.3.2 Localized Surface Plasmons Resonances

For the case of isolated or partially isolated subwavelength metallic particles, another interesting phenomenon is observed. To understand this, we look at the dipole moment induced in a small metallic sphere, *i.e.*

$$p = \alpha E_0 \quad \text{where} \quad \alpha = 4\pi\epsilon_{\text{med}} r^3 \left(\frac{\epsilon_{\text{particle}} - \epsilon_{\text{med}}}{\epsilon_{\text{particle}} + 2\epsilon_{\text{med}}}\right) \tag{2.3.18}$$

Where $\epsilon_{\text{particle}}$ and $\epsilon_{\text{med}}$ are the permittivities of the metallic nanoparticle and surrounding dielectric medium respectively.

For the case of metallic nanoparticles, we observe that their dielectric permittivity can take on negative values, and as $\epsilon_{\text{particle}} \rightarrow -2\epsilon_{\text{med}}$ (known as the Fröhlich condition[72]) the polarizability and therefore induced dipole moment approaches infinity in the lossless case. Damping of charge density oscillations in the metal prevents infinite values from being obtained in reality, but this serves to illustrate the extreme electric field enhancements that these particles are able to provide. As an extension of this, metallic nanoparticles that are nearby can strongly couple to one another, further extending the electric field enhancement capabilities (see Figure 7)[73].

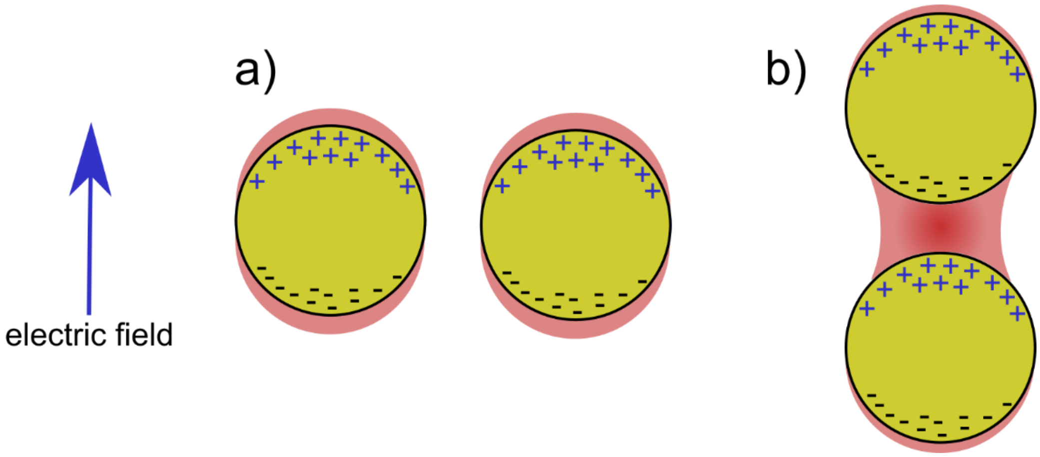

**Figure 7** – Coupling between nearby nanoparticles and relative field enhancement with respect to electric field orientation. a) shows two small metallic particles with their relative position vector perpendicular to the applied electric field and negligible coupling. b) indicates the case where the nanoparticles are orientated in parallel with the applied electric field and a large electric field enhancement is observed between the two particles, known as a plasmonic “hot spot”.

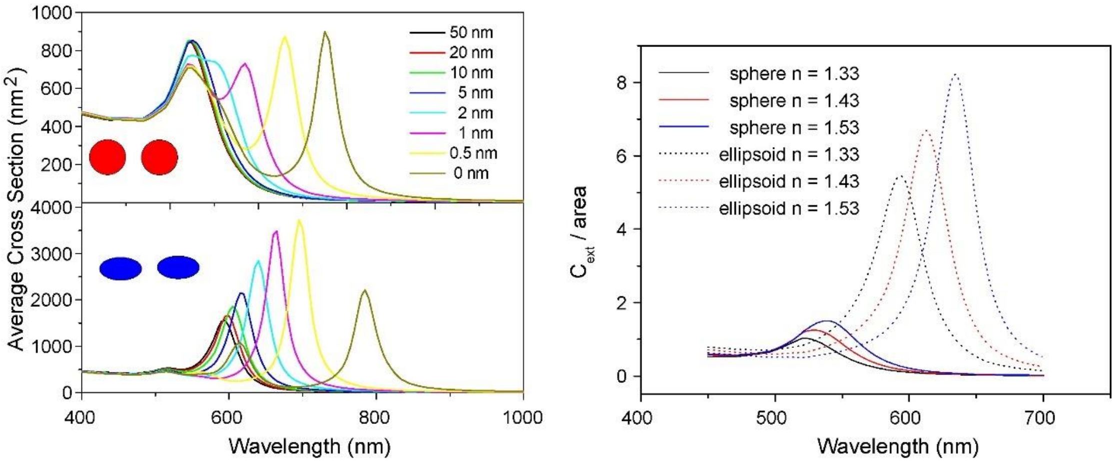

**Figure 8** – Plasmonic resonances for gold nanoparticles as function of interparticle distance. Left: average optical cross section for coupled gold nanoparticles (20 nm spheres – top/red, ellipsoids with aspect ration = 2 – bottom/blue). Right: total cross section normalized to physical cross section for gold nanospheres and ellipsoids in various dielectric mediums. Reprinted with permission from[22].

In the subwavelength approximation, the metallic sphere is treated as a dipole with interaction cross sections given by:[8]

$$\sigma_{\text{scattering}} = \frac{3}{2\pi}\left(\frac{\omega}{c}\right)^4 \left(\frac{\epsilon_{\text{med}}}{\epsilon_0}\right)^2 V^2 \frac{\left(\epsilon'_{\text{particle}} - \epsilon_{\text{med}}\right)^2 + \left(\epsilon''_{\text{particle}}\right)^2}{\left(\epsilon'_{\text{particle}} + 2\epsilon_{\text{med}}\right)^2 + \left(\epsilon''_{\text{particle}}\right)^2} \tag{2.3.19a}$$

$$\sigma_{\text{extinction}} = \frac{9\omega}{c}\left(\frac{\epsilon_{\text{med}}}{\epsilon_0}\right)^{\frac{3}{2}} V \frac{\epsilon''_{\text{particle}}}{\left(\epsilon'_{\text{particle}} + 2\epsilon_{\text{med}}\right)^2 + \left(\epsilon''_{\text{particle}}\right)^2} \tag{2.3.19b}$$

$$\sigma_{\text{absorbed}} = \sigma_{\text{extinction}} - \sigma_{\text{scattering}} \tag{2.3.19c}$$

Where $\sigma$ denotes the respective cross sections for scattering, extinction, and absorption, $V$ is the volume of the particle, and $\epsilon'$, $\epsilon''$ denote the real and imaginary components of the permittivity. As shown above, when the real part of the permittivity of the particle approaches negative two times that of the surrounding medium, the interaction with light increases drastically. This condition for this phenomenon is similar in form to the condition of surface plasmons presented earlier.

## 2.4 Optical Trapping

### 2.4.1 Introduction

Optical trapping is a method by which electromagnetic radiation can be used to impart a force on a particle in such a way that the particle is localized in two or three dimensions. The concept of optical trapping can be understood for larger particles using the ray optics model. Consider a situation where a photon of light scatters off of a particle. Because photons carry linear momentum, any change in the direction of photons will require a force to be imparted on the particle such that momentum is conserved, a phenomenon commonly known as radiation pressure. In a similar way, angular momentum can also be exchanged between a particle and photon[51,74]. The theoretical understanding of these optical forces was developed during the 19th century[75,76].

The first demonstration of radiation pressure used thermal light sources to deflect a mirror attached to a torsion balance from its equilibrium position[77–79]. At the time it was believed that due to the minuteness of these forces they could not be utilized in any practical applications[79,80]. It was not until the advent of the laser that optical forces had the magnitude necessary to be utilized as an effective tool. In 1970 Arthur Ashkin *et al.* developed the first experimental realization of optical trapping[47,60,81,82]. Since then the method of optical trapping has found a plethora of applications in manipulation[51,83–85], assembly[53,56,86], and sensing[49,54,87–89] of micro and nanoscale objects.

Shown in Figure 9a) is a plot of the typical forces a particle will experience due to optical interactions when located at or near the beam waist of a highly focused laser beam. The two main components of the total optical force are the scattering and gradient force. In the ray optics approximation (which applies to particles with size much greater than trapping wavelength) the scattering force is due to high angle scattering events (reflection), where photons will *push* the particle along the direction of the laser beam's k-vector. Conversely the gradient force pulls or pushes the particle depending on if it focuses or defocuses the light. The gradient force can be visualized as a result of refraction using the ray optics approximation as shown in Figure 9b). The total force (dashed black line in Figure 9a)) is the sum of both the scattering and gradient forces, anywhere that the total force is zero and surrounded by restoring forces is theoretically a potential trapping location. Figure 9 c) shows a schematic diagram indicating several different particle locations and the forces acting on the particle.

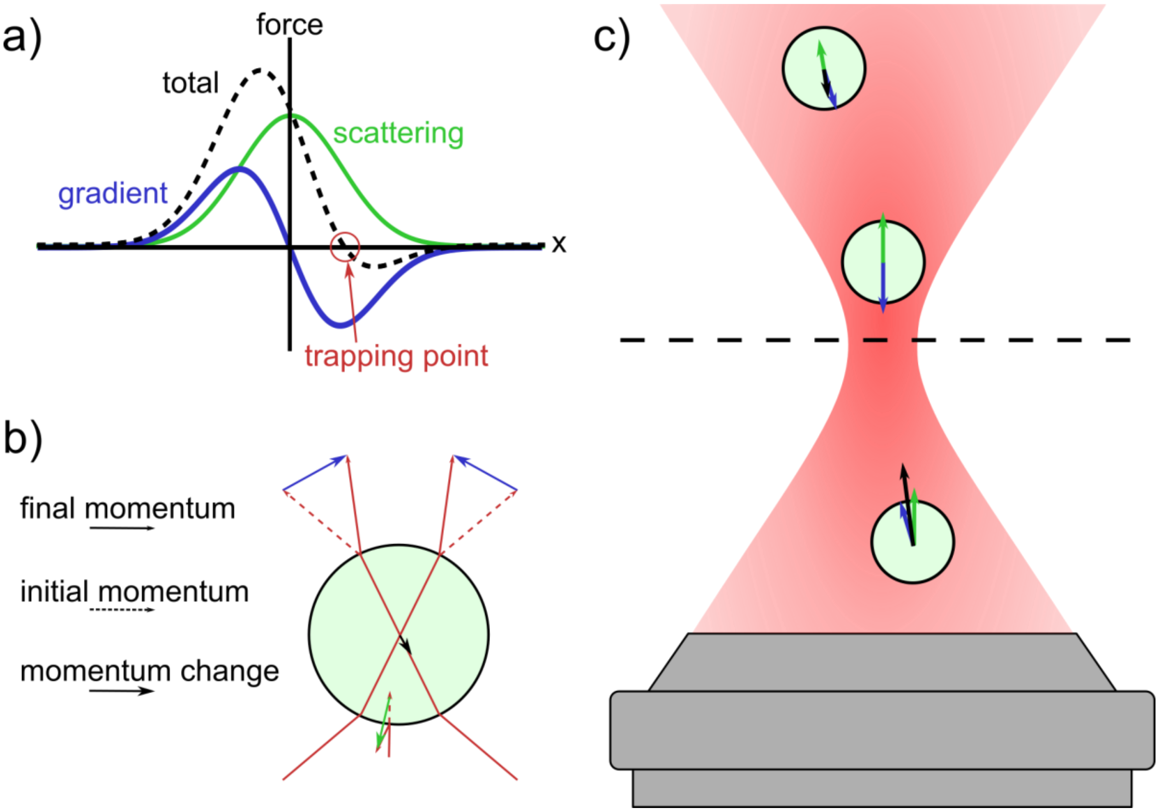

**Figure 9** – a) graph showing the forces acting on a particle in an optical trapping configuration for a Gaussian beam profile. The point x = 0 at the intersection of the axis, coincides with the centre of the focused beam waist (dashed line in c)). b) a simplified force vector diagram of the ray-model approximation to trapping forces, the length of each vector indicates the relative intensity of that interaction. c) a schematic diagram of an optical trapping configuration. The circles are particles near the beam waist showing relative intensities of scattering, gradient, and net forces for each particle. The particle just above the dashed line indicates the stable trapping position as indicated in a).

For Rayleigh particles, that are much smaller than the trapping wavelength, significantly greater optical powers are required for a stable free-space trap and the interactions are governed by the subwavelength quasi-static methods developed in Section “2.2 Rayleigh Scattering”. The reason for requiring higher optical intensities for smaller particles (even through scattering forces are negligible), is due to an increase in Brownian motion at smaller size scales[90]. For a spherical dielectric particle in an optical trap, the trapping potential is[91]

$$U = \frac{2\pi n_{\mathrm{med}} r^3}{c}\left(\frac{n_{\mathrm{particle}} - n_{\mathrm{med}}}{n_{\mathrm{particle}} + 2n_{\mathrm{med}}}\right) I \qquad (2.4.1)$$

Where $n_{\mathrm{med}}$ and $n_{\mathrm{particle}}$ are the refractive index of the surrounding medium and particle respectively, $r$ is the particle radius, and $I$ is the intensity of light. In order for an optical trap to be stable, the potential well of the trapping force must significantly exceed the thermal kinetic energy of the particle so that the particle is not lost due to Brownian motion. As can be seen in the equation above, the trapping potential is proportional to the particles radius cubed. This implies that if the radius of the particle is reduced by one order of magnitude, then the intensity of the trapping laser must be increased by three orders of magnitude to maintain the same trapping potential. For these reasons it is exceedingly difficult to trap most dielectric particles on the nanometer scale without using excessive laser powers which would damage the particle, particularly in the case of biological samples.

To resolve this limitation, researchers have turned to new trapping techniques such as aperture assisted trapping. This method enables the effective trapping of dielectric and biological particles in the nanometre regime. The following sections serve to provide some insight into the phenomena that permits aperture assisted trapping to be an effective optical tool.

### 2.4.2 Bethe’s Aperture Theory

To understand how an aperture can be used to trap subwavelength particles, we must know how the apertures themselves interact with light. The theoretical understanding for subwavelength aperture transmission characteristics was developed by Hans Bethe in 1944[92]. Bethe's initial work used a quasi-static approximation to the transmission of a plane wave through a subwavelength circular aperture in an infinitely thin perfect electrical conductor film. In this approximation, the circular aperture is replaced with a magnetic dipole. The power radiated (**$P$**) by the dipole is given by:[93]

$$\boldsymbol{P} = \frac{Z_0 k^4}{12\pi} |p_m|^2 \quad \text{with} \quad p_m = \alpha_m H_0 \tag{2.4.2}$$

Here, $Z_0$ is the impedance of free space, $k = 2\pi/\lambda$ is the wave vector, and $p_m$ is the magnetic dipole moment of the aperture. For a circular aperture of radius $r_a$ in a thin perfect electrical conductor, the net magnetic polarizability is[94]

$$\alpha_m = \frac{8r_a^3}{3} \tag{2.4.3}$$

The transmission through the aperture is then half of the total power radiated by the dipole, *i.e.*

$$T = \frac{128 Z_0 \pi^3}{27} \frac{r_a^6}{\lambda^4} H_0 \tag{2.4.4}$$

As can be seen above, the transmission through the aperture is proportional to the sixth power of the radius of the aperture. When normalized to the area of the aperture the transmittance is proportional to $\left(\frac{r}{\lambda}\right)^4$, indicating a rapid decrease in transmittance as the aperture is scaled below the wavelength of incident light. In the case where the refractive index of the aperture and surrounding medium is replaced from material 1 to material 2, the relative change in transmission is

$$\frac{T_2}{T_1} = \left(\frac{\lambda_1}{\lambda_2}\right)^4 = \left(\frac{n_2}{n_1}\right)^4 \tag{2.4.5}$$

The above equation indicates how increasing the effective index of the medium can cause a large increase in transmission as illustrated in Figure 10.

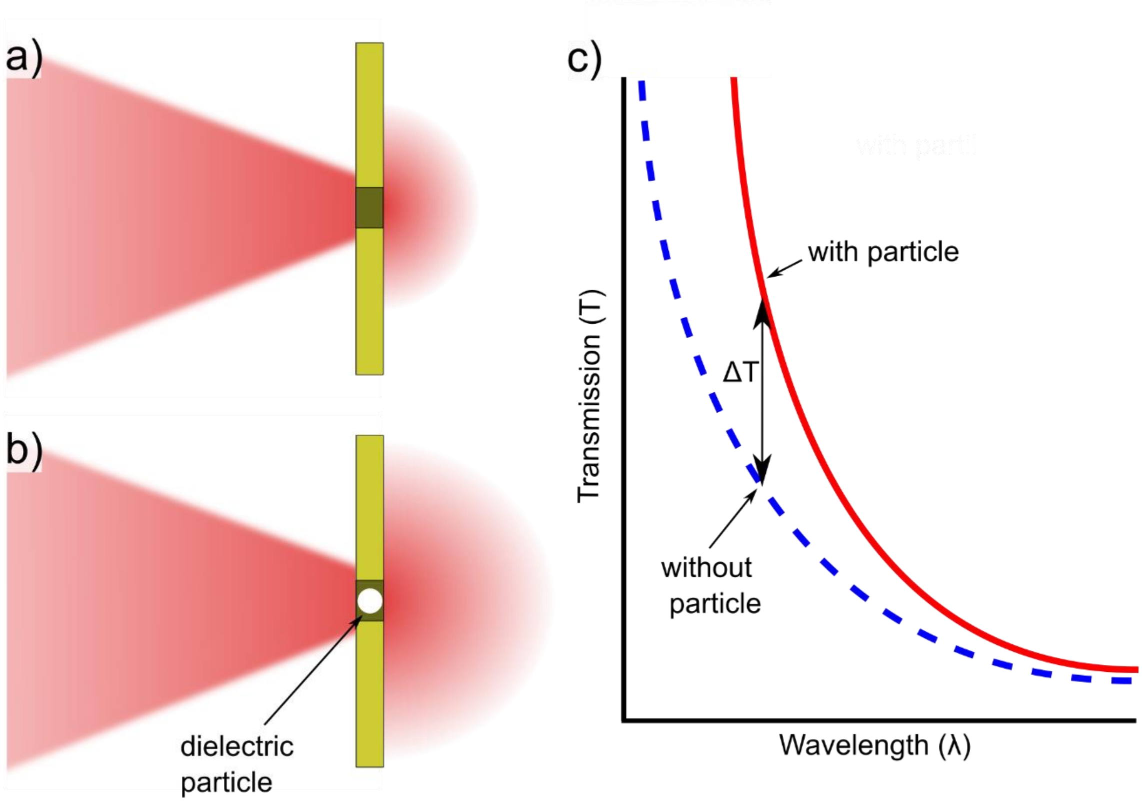

**Figure 10** – Illustrative example of transmission change through a subwavelength aperture upon dielectric loading which increases the effective refractive index. a) and b) show the transmission through the aperture without and with an embedded particle respectively. c) indicates the transmission curves as a function of wavelength.

Work has been conducted to extend this theoretical approximation to real metallic films at visible frequencies where the perfect electrical conductor and infinitely thin approximations become invalid. Experimental evidence shows a strong correlation for these real apertures when compared to the theory developed by Bethe as shown in Figure 11 below[95]. This implies that although the axioms assumed in Bethe’s theory are unrealistic, the conclusions drawn qualitatively agree well with the observations for transmission through a subwavelength hole in a real metal film.

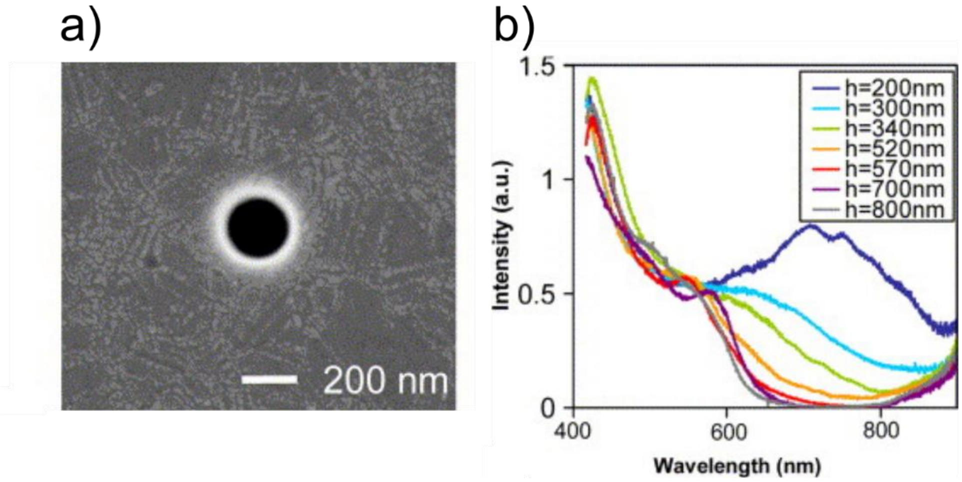

**Figure 11** – Transmission properties of cylindrical holes milled in suspended gold films. a) scanning electron microscope image of subwavelength aperture in gold film. b) transmission spectra at normal incidence for hole diameter d = 270 nm and for hole depth h as indicated. Reprinted with permission from[95].

### 2.4.3 Aperture Trapping

Extending the principles that were developed by Bethe, the forces which occur when a particle enters the aperture have been investigated[50,96]. In 2009 the method of self induced back-action (SIBA) was introduced as a method for nanoaperture based trapping[97–99]. The method of SIBA introduces several advantages when compared to trapping without the aid of an aperture. As an extension from Bethe's theory, the presence of a particle (with greater dielectric constant than the surrounding medium, *i.e.* $\epsilon_{\text{particle}} > \epsilon_{\text{med}}$) will increase the effective index of the aperture's surrounding and cause an increase in the transmission. If the particle were to be perturbed from the inside of the aperture, the transmission would be reduced and the decrease in momentum carried by the light through the aperture would be imparted on the particle. From an experimental standpoint, these trapping apertures are often one-sided, and constructed in such a way that the displacement of a particle from the aperture will cause a restoring force to push the particle back into the aperture.

An additional enhancement factor, due to a metallic aperture, results from localized plasmon resonances generated at “hot spots” within the aperture that cause an increase the local field strength. This enhancement factor can greatly reduce the power requirement for stable nanoparticle trapping as well as confines those fields to a region well below the diffraction limit. This subwavelength confinement of light creates a higher degree of localization in the trap. Due to the evanescent nature of plasmons this effect increases the electric field gradient and therefore the gradient force. Yet another advantage to trapping with apertures in metal films is the inherent ability of the film to act as a heat sink to reduce the local temperture[100,101].

## 2.5 Raman Spectroscopy

The discovery of Raman spectroscopy was originally performed by Sir Chandrasekhara Venkata Raman in 1928, and earned him the Nobel prize in physics in 1930. Raman spectroscopy is a method used for observing the spectral fingerprint of a molecule’s vibrational modes as a result of inelastic collisions between the particle and incident light. Essentially, a molecule is in a specific energy state at any point in time, which consists of its electronic, vibrational, and rotational energy states. For Raman spectroscopy we are mainly concerned with transitions between vibrational states/modes of the particle. To conceptualize the meaning of a vibrational state or mode, we first consider a classical view of a simple diatomic molecule[20]. In this classical approximation we consider two masses connected by a spring as shown in Figure 12.

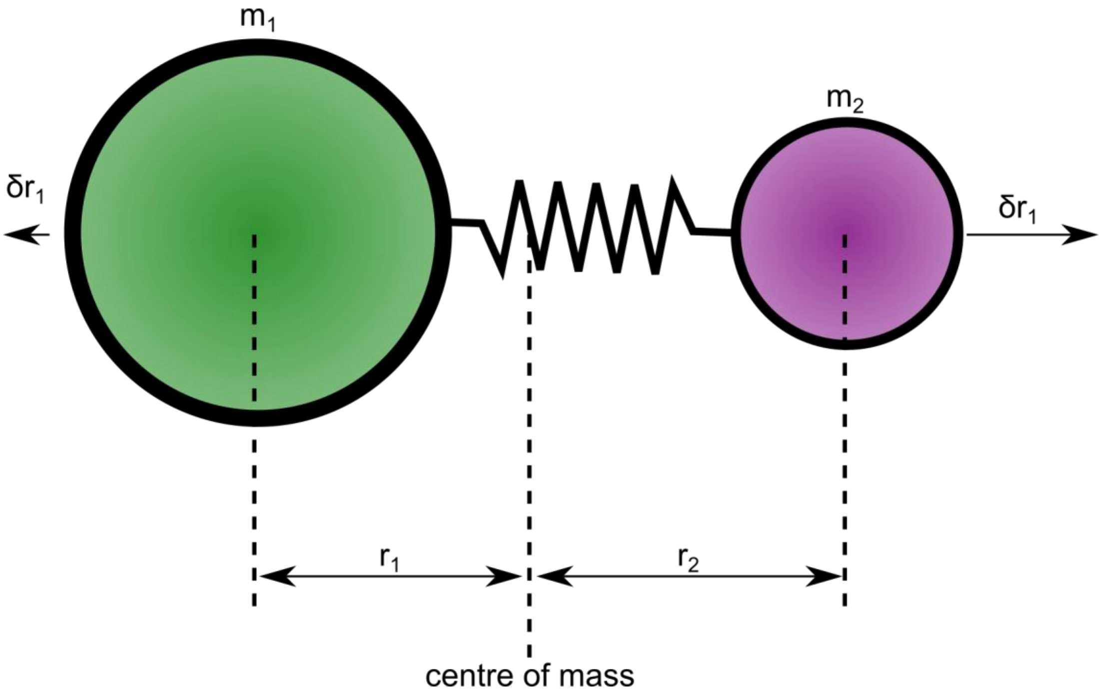

**Figure 12** – Classical approximation to a diatomic molecule.

Here, the distance from each particle to the centre of mass is governed by the equation

$$m_1 r_1 = m_2 r_2 \tag{2.5.1}$$

To analyze the vibrational modes, we next consider that each of these particles is perturbed from their equilibrium position by a small displacement, *i.e.*

$$m_1(r_1 + \mathrm{\delta r}_1) = m_2(r_2 + \delta r_2) \tag{2.5.2}$$

By taking the difference between these two equation we are able to define a relationship between the displacements from equilibrium and the masses of the two particles

$$\delta r_1 = \left(\frac{m_2}{m_1}\right)\delta r_2 \quad \text{and} \quad \delta r_2 = \left(\frac{m_1}{m_2}\right)\delta r_1 \tag{2.5.3}$$

For small perturbations from equilibrium the restoring force can be considered linear as given by Hooke’s law and defined by the spring constant *k*. The restoring force due to this small perturbation is then given by

$$F = -k(\delta r_1 + \delta r_2) = -k\left(\frac{m_1 + m_2}{m_2}\right)\delta r_1 = -k\left(\frac{m_1 + m_2}{m_1}\right)\delta r_2 \tag{2.5.4}$$

Then, by applying Newton's second law of motion $F = ma = m\frac{d^2x}{dt^2}$ we have derived two second order differential equations governing the motion of each particle

$$m_1\frac{d^2\delta r_1}{dt^2} = -k\left(\frac{m_1 + m_2}{m_2}\right)\delta r_1 \quad \text{and} \quad m_2\frac{d^2\delta r_2}{dt^2} = -k\left(\frac{m_1 + m_2}{m_1}\right)\delta r_2 \tag{2.5.5}$$

Adding these two equations of motion yields

$$\frac{m_1 m_2}{m_1 + m_2}\left(\frac{d^2\delta r_1}{dt^2} + \frac{d^2\delta r_2}{dt^2}\right) = -k(\delta r_1 + \delta r_2)$$

At this point we define the reduced mass $\mu$ and total displacement $\delta r$ to obtain the single variable second degree differential equation of motion as:

$$\mu\frac{d^2\delta r}{dt^2} = -k\delta r \tag{2.5.6}$$

Upon inspection, this equation is identified as a simple harmonic oscillator with solution $\delta r = \delta r_{\text{max}}\sin(\omega t + \phi)$ and vibrational frequency $f = \frac{\omega}{2\pi} = \frac{1}{2\pi}\sqrt{k/\mu}$. The potential energy of this system is linearly related to the spring constant according to the following relation[20]

$$U = \frac{1}{2}k\delta r^2 = \frac{1}{2}k\delta r_{\text{max}}\sin^2(\omega t + \phi) = \frac{1}{2}\mu(\omega\delta r_{\text{max}})^2\sin^2(\omega t + \phi) \tag{2.5.7}$$

Similarly, the kinetic energy is defined as

$$T = \frac{1}{2}\mu\left(\frac{d\delta r}{dt}\right)^2 = \frac{1}{2}\mu(\omega\delta r_{\text{max}})^2\cos^2(\omega t + \phi) \tag{2.5.8}$$

Resulting in a total vibrational energy of

$$E = U + T = \frac{1}{2}\mu(\omega\delta r_{\text{max}})^2 = \text{constant} \tag{2.5.9}$$

Thus as we can see for this classical example, a diatomic molecule with a specified vibrational frequency $f$ corresponds to a state with constant energy $E$. At this point we must take a departure from the classical analogy because it begins to deviate from reality. The classical model implies a continuum of energy states which is not observed experimentally.

To understand a more complete picture of the oscillating diatomic molecule we must employ quantum mechanics by solving the Schrödinger equation under the same potential[20,102,103].

$$\frac{d^2\psi}{d\delta r^2}+\frac{8\pi^2\mu}{h^2}\left(E-\frac{1}{2}k\delta r^2\right)\psi=0 \tag{2.5.10}$$

Under the condition that $\psi$ must be single valued, continuous, and finite, the resulting eigenvalues of the Schrödinger equation (which corresponds to observable energy states) is given by (see "Appendix A" for more details)[20]:

$$E_v=hf\left(v+\frac{1}{2}\right) \tag{2.5.11}$$

The frequency of vibration in this case is the same natural frequency as that obtained by the classical approximation. In the above equation the vibrational quantum number $v$ is included which must be greater than or equal to zero and can only hold integer values. The inclusion of the vibrational quantum number implies discrete energy levels, as opposed to the continuum of energy states allowed by classical mechanics.

Although this quantum mechanical model is more complete, it still does not fully describe the reality of the situation. This is because the spring model of the potential energy is an inadequate approximation to the internuclear forces present. A real diatomic model has a potential energy curve which can accurately be approximated by the Morse potential, defined by[20]

$$U = D_e\left(1 - \mathrm{e}^{-\beta\delta r}\right)^2 \tag{2.5.12}$$

Where $D_e$ is the disassociation energy (energy required to completely separate the particles), and $\beta$ is an empirical measure of the curvature of the potential well. In Figure 13 the energy states for a diatomic molecule are illustrated on the left, indicating the difference in magnitude between electronic, vibrational, and rotational energy states. On the right is a diagram of the Morse potential defining the energy spacing of successive vibrational states. Notice for the Morse potential that energy states are discrete but approach a continuum as the energy approaches the disassociation energy.

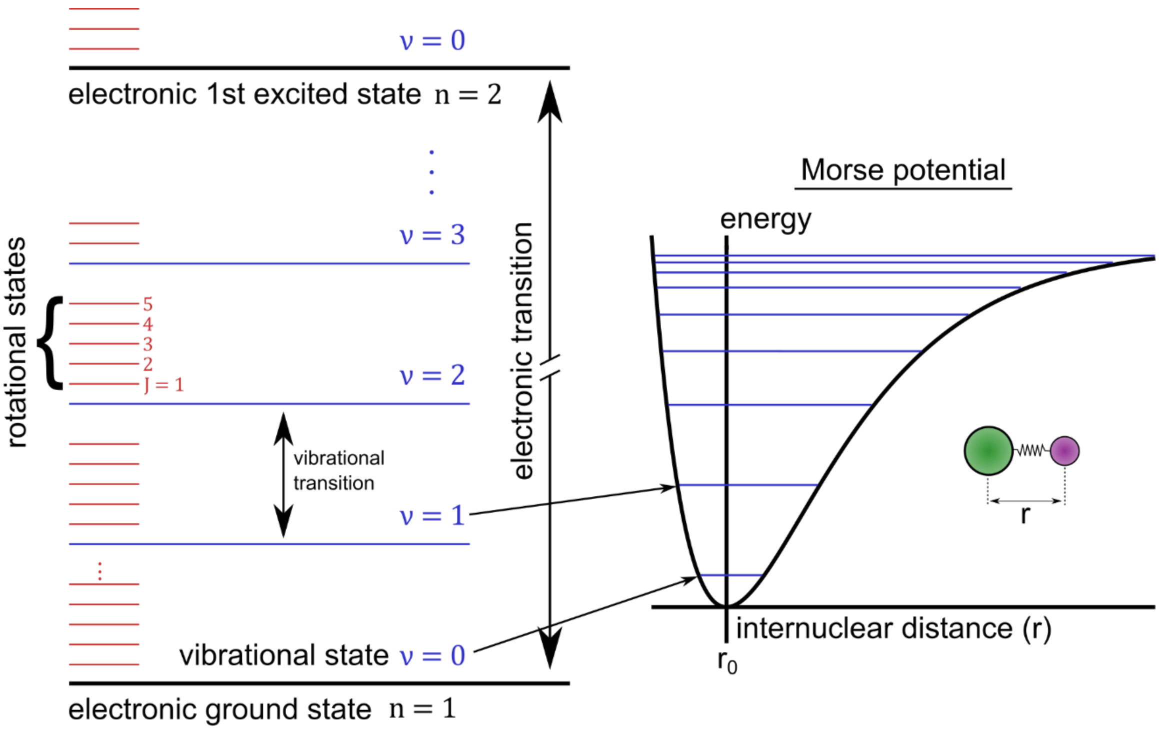

**Figure 13** – Energy level diagram (left) for a diatomic molecule indicating electronic, vibrational, and rotations energy states. The distribution in energy of these vibrational states follows a Morse potential as indicated on the right.

To understand how transitions between vibrational states effects the scattering of light, we use classical electromagnetic theory to examine the vibrational modes' effect on the polarizability of a molecule[20]. The excitation light source can be described as an electromagnetic wave oscillating with frequency $f_0$

$$E = E_0 \cos(2\pi f_0 t) \tag{2.5.13}$$

The dipole moment induced on a particle interacting with this wave is given by

$$p = \alpha E = \alpha E_0 \cos(2\pi f_0 t) \tag{2.5.14}$$

For a molecule vibrating at frequency $f_m$ as described previously, the polarizability ($\alpha$) of the particle, can have its vibrational dependence approximated as the first two terms of a Taylor series polynomial, *i.e.*

$$\alpha = \alpha_0 + \delta r \left( \frac{\partial \alpha}{\partial \delta r} \right|_{\delta r = 0} \tag{2.5.16}$$

Specifically, this equation defines which vibrational modes are "Raman active", *i.e.* they result in inelastic scattering events that are due to a change the polarizability of the molecule as it vibrates. The dipole moment of the particle then becomes:

$$\begin{aligned} p = \alpha E_0 \cos(2\pi f_0 t) &= \alpha_0 E_0 \cos(2\pi f_0 t) + \delta r \left( \frac{\partial \alpha}{\partial \delta r} \right|_{\delta r = 0} E_0 \cos(2\pi f_0 t) \\ &= \alpha_0 E_0 \cos(2\pi f_0 t) + \left( \frac{\partial \alpha}{\partial \delta r} \right|_{\delta r = 0} E_0 \delta r_{\mathrm{max}} \cos(2\pi f_0 t) \cos(2\pi f_m t) \end{aligned} \tag{2.5.17}$$

Finally, the net dipole moment of the particle is

$$p = \alpha_0 E_0 \cos(2\pi f_0 t) + \frac{1}{2} \left( \frac{\partial \alpha}{\partial \delta r} \right|_{\delta r = 0} E_0 \delta r_{\mathrm{max}} [\cos(2\pi [f_0 + f_m]) + \cos(2\pi([f_0 - f_m])] \tag{2.5.18}$$

The first term in the above expression describes a dipole oscillating at the incident frequency which corresponds to Rayleigh scattering. The second term, which is dependent on the polarizability being perturbed by the vibration of the molecule, is the Raman scattering with frequency $f_0 - f_m$ (Stokes shift) and $f_0 + f_m$ (anti-Stokes). Here we can see how inelastic collisions due to polarizability changes resulting from molecular vibrations cause a shift in the frequency (and therefore energy) of the scattered light.

To understand which vibrational modes are Raman active we perform normal mode analysis on the vibrations of a simple $CO_2$ molecule to understand its effect on polarizability. For any molecule consisting of $N$ atoms, the molecule has $3N$ degrees of freedom[20]. Of these $3N$ degrees of freedom, three correspond to translational freedom, and three correspond to rotational freedom (or two in the case of linear molecules). Therefore, for an N atom molecule there are $3N$-6 degrees of vibrational freedom (or $3N$-5 for linear molecules). For the case of $N$=2 (diatomic molecule), this corresponds to 1 degree of vibrational freedom as discussed earlier. For $N$=3, such as for a linear $CO_2$ molecule this results in 4 degrees of vibrational freedom as shown in Figure 14.

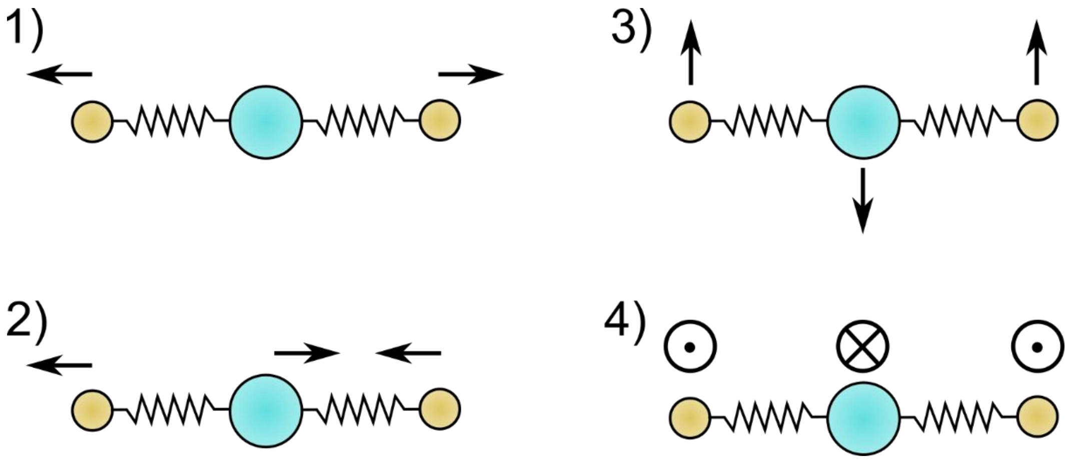

**Figure 14** – Normal modes of vibration for a $CO_2$ molecule. Note that vibrational modes 3 and 4 correspond to the same molecular vibration rotated by $90°$[20].

In order to understand which vibrational modes are Raman active we must look at the polarizability of the molecule as it goes through each vibrational mode (see Figure 15). As defined by the dependence of the polarizability on the displacement from equilibrium, *i.e.* $\alpha = \alpha_0 + \delta r \left(\frac{\partial \alpha}{\partial \delta r}\right)_{\delta r = 0}$, a vibrational mode is only Raman active if the derivative of the polarizability is non-zero when evaluated at its equilibrium internuclear separation. This implies that even if the polarizability of the molecule changes throughout its vibration, it is only Raman active if the polarizability is different at the maximum and minimum displacements from equilibrium. Figure 15 shows the polarizability ellipsoids for a $CO_2$ molecule as it goes through its vibrational modes, only vibrational mode 1 is Raman active as this is the only mode where the polarizability is not symmetric about its equilibrium separation distance.

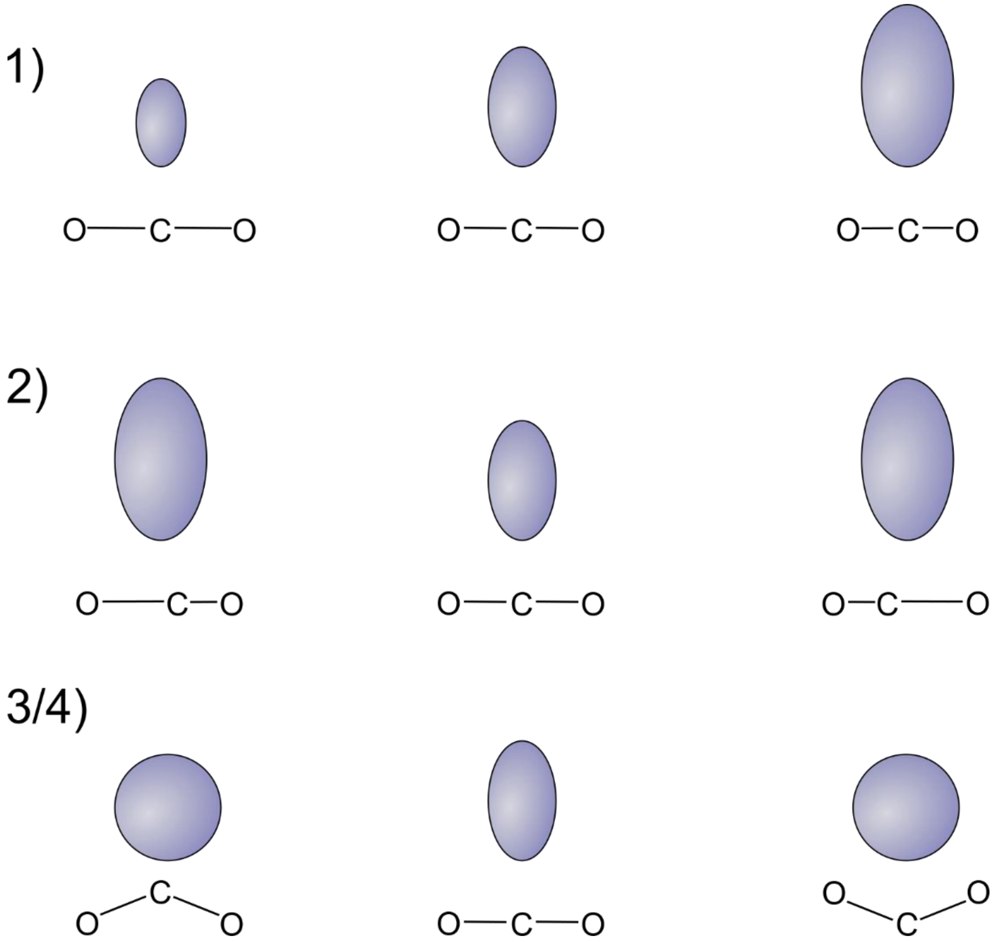

**Figure 15** – Polarizability changes of $CO_2$ molecule as it goes through its normal modes of vibrations[20]. Ellipsoids indicate polarizability of molecule for the configurations shown below. Numbers correspond to the vibrational modes shown in Figure 14. Only vibrational mode 1 in Raman active.

The classical analysis of molecular vibrations and their effects on optical scattering enables us to understand which vibrational modes are Raman active and how these cause a frequency shift in the scattered light; however, it does not explain why scattering events corresponding to $f_0 + f_m$ are found experimentally to be significantly less likely than those corresponding to $f_0 - f_m$. To understand why certain Raman transitions, occur more prominently than others we must return to a quantum mechanical view of the system.

In regular Raman spectroscopy the excitation wavelength is chosen to be significantly below the energy required for electronic energy level transitions. As a result, the molecules involved in the scattering event will be elevated to a virtual state and immediately relax to one of their vibrational eigenstates (see Figure 16). Statistically, most molecules will initially be in their lowest energy or "ground" state as governed by the Maxwell-Boltzmann distribution law given below[20,104].

$$\frac{N_1}{N_0} = \mathrm{e}^{\frac{-\Delta E}{k_b T}} \tag{2.5.19}$$

Here, $N_0$ and $N_1$ correspond to the number of molecules in the $v = 0$, and $v = 1$ states respectively. $\Delta E$ is the energy level difference between the vibrational states, $k_b$ is Boltzmann's constant, and $T$ is the absolute temperature in Kelvin.

As a result, in most scattering collisions of this type, the molecule is initially in its ground state and relaxes back to this same state (after excitation) in what is known as an elastic collision or Rayleigh scattering, where the scattered photon has the same energy as the incident photon. For a small number of scattering events an inelastic collision occurs where the molecule is initially in the ground state but after scattering is in an excited state, thereby retaining some of the energy of the incident photon. The scattered photons in these event will be red-shifted and have lower energy than their incident counterparts. When observing the scattering event with a spectrometer, this will correspond to a peak at a lower frequency than the incident laser line known as a "Stokes peak". For another small subset of these scattering collisions the molecule is initially in an excited state but after the scattering collision relaxes to the ground state, and hence by conservation of energy, the scattered photon has an increased frequency which is observed as an anti-Stokes peak as indicated in Figure 16.

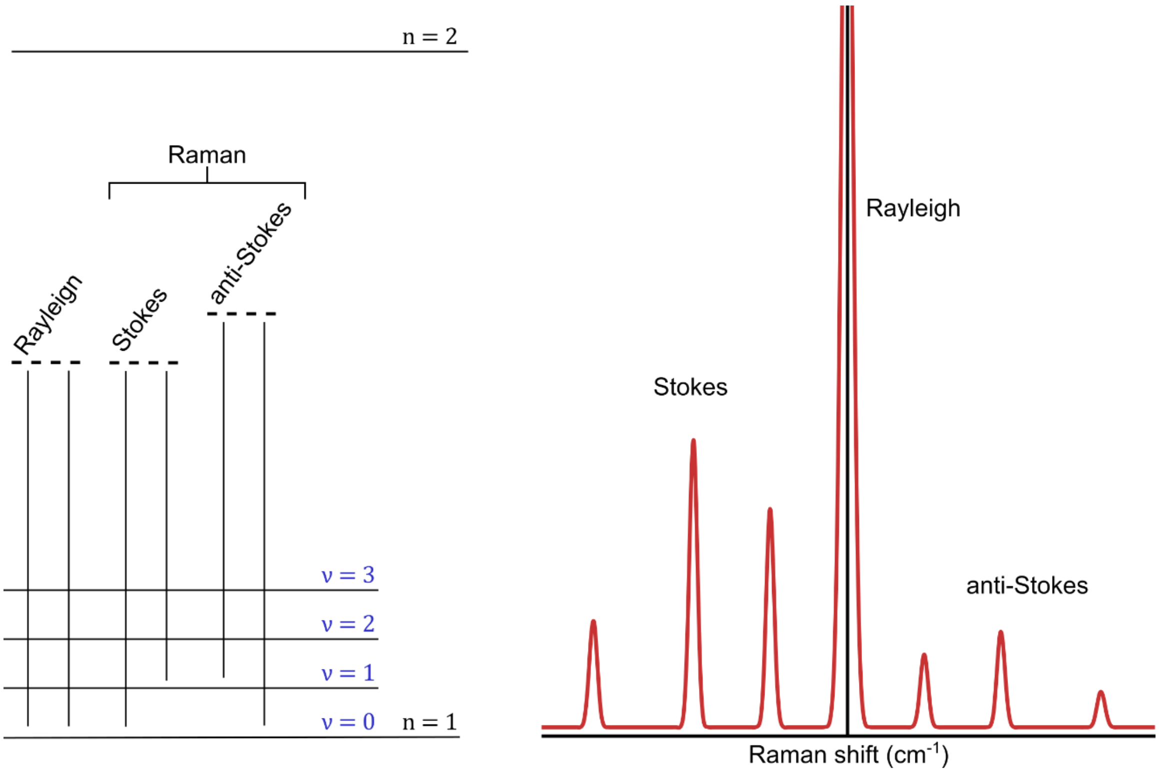

**Figure 16** – Energy level diagram (left) of a molecule undergoing Raman scattering. The blue $\boldsymbol{v}$’s indicate vibrational energy states and the black n’s are for electronic energy states. Dashed lines indicate a virtual energy state. On the right is an illustration of a hypothetical Raman spectra indicating the shift in frequency (energy) of inelastic scattering events corresponding to Stokes and anti-Stokes spectral peaks. The central peak labeled “Rayleigh” corresponds to elastic scattering events and has the same frequency as the excitation source.

### 2.5.1 Surface Enhanced Raman Spectroscopy

Due to the relatively small cross section of Raman scattering events researchers have sought ways to amplify these signals. One particularly useful method of increasing the rate of Raman active transitions is by employing plasmons to enhance the electric fields of the excitation laser such that the increased interaction between the confined electric fields and the analyte molecule leads to an increased rate of Raman scattering events. The degree of Raman enhancement in Surface Enhanced Raman Scattering (SERS) is due to two effects, first the enhancement of the local electric fields, and secondly due to the enhancement of radiation from the molecule, *i.e.*

$$\text{Enhancement Factor} = Q_{\text{Loc}} \times Q_{\text{Rad}} \tag{2.5.20}$$

Typically, it is assumed that $Q_{\text{Loc}} \approx Q_{\text{Rad}}$, and the total enhancement factor is

$$\text{Enhancement Factor} = \frac{|E_{\text{Loc}}|^4}{|E_{\text{Inc}}|^4} \tag{2.5.21}$$

Where $E_{\text{Loc}}$ is the localized electric field at the analyte location, and $E_{\text{Inc}}$ is the incident electric field amplitude. This is known as the "$|E|^4$-approximation", and is accurate in most situations[35].

# Chapter 3 – Methods

## 3.1 Introduction

In this Chapter the methods used in aperture assisted trapping are presented. First, the general optical setup used for trapping is detailed. Following this is a brief introduction into the trapping aperture design and fabrication. Finally, the techniques used to prepare the desired analyte for trapping, execute the trapping experiment, and acquire data are demonstrated.

## 3.2 Experimental Setup

The basis of an optical trapping setup is essentially a modification to an inverted microscope as shown in Figure 17. The sample, shown in the centre of Figure 17, consists of the solutions of nanoparticles to be trapped and the trapping aperture (see Section "3.4 Sample Preparation"). The sample is held in place by a 3-axis stage between two microscope objectives. The trapping laser ("laser diode" in Figure 17) is launched from the right hand side of the figure towards a dichroic mirror where it is reflected into the high numerical aperture (NA) condenser objective. The trapping laser is focused to a diffraction limited spot that is aligned with the trapping aperture. The light which is transmitted through the aperture is collected by another objective and reflected by a secondary dichroic mirror towards a photodiode for detection. After the trapping laser is initially launched its polarization is controlled by a half wave plate and it is expanded by a Galilean beam expander until the beam spot fills the back aperture of the condenser objective. Simultaneously, the light from a white light emitting diode is transmitted through the upper dichroic mirror and through the sample before being directed towards a camera for imaging. The imaging of the sample by the camera is used to visually align the laser with the trapping apertures.

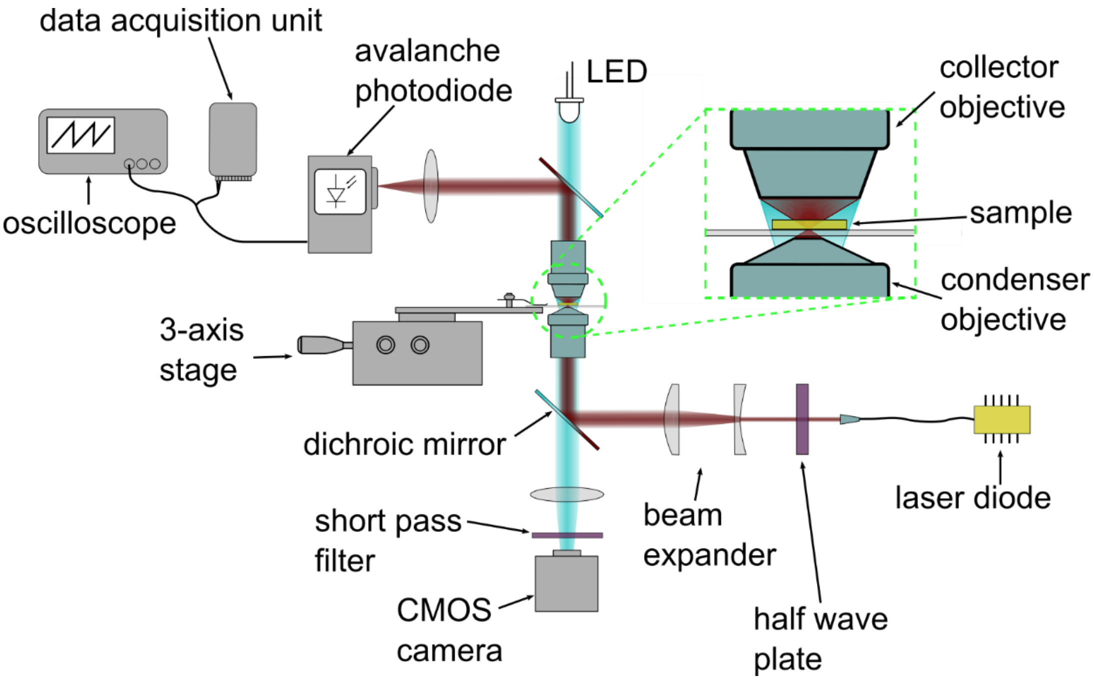

**Figure 17 -** The basic design of the optical trapping microscope used for the work in this thesis.

The trapping laser used has a wavelength in the visible or near-IR region to be able to be detected by the camera and to take advantage of the relatively low absorption by water at these wavelengths. The signal detected by the photodiode is visually monitored on an oscilloscope, while being recorded by a high frequency data acquisition unit for real-time and post analysis. Typical acquisition rates range from 1 kHz to 1 MHz depending on the acquisition length and time scale of the features to be resolved. The specifics of the trapping wavelength and condenser objectives used are discussed in later sections (see Section “4.3 Optical Trapping and Raman Integration” and Section “5.3 Optical Trapping and Magnetic Field Integration”).

### 3.3 Aperture Fabrication

For all of the work presented here, a dual nanohole (DNH) trapping aperture was used. In general, the trapping aperture has three primary functions:

1. Enhance the electric fields of the trapping laser
2. Confine the trapped particle within a suitably small region
3. Enable detection of trapping *via* change in transmission

The DNH aperture (see Figure 18) has been deemed suitable and is used in the majority of trapping based experiments performed by the nanoplasmonics group at UVic. The DNH aperture is advantageous for several reasons, both from the perspective of trapping efficiency and from a fabrication standpoint. With respect to confining the electric fields of the trapping laser, this is achieved *via* localized surface plasmon resonances which are concentrated on the cusps of the DNH aperture at the smallest gap width (Figure 19). This aperture feature addresses both primary functions 1 and 2, by making the trapping location coincide with the region where the trapped particle is most confined by the physical structure of the aperture. Additionally, the DNH trapping aperture exhibits a detectable change in transmission upon trapping.

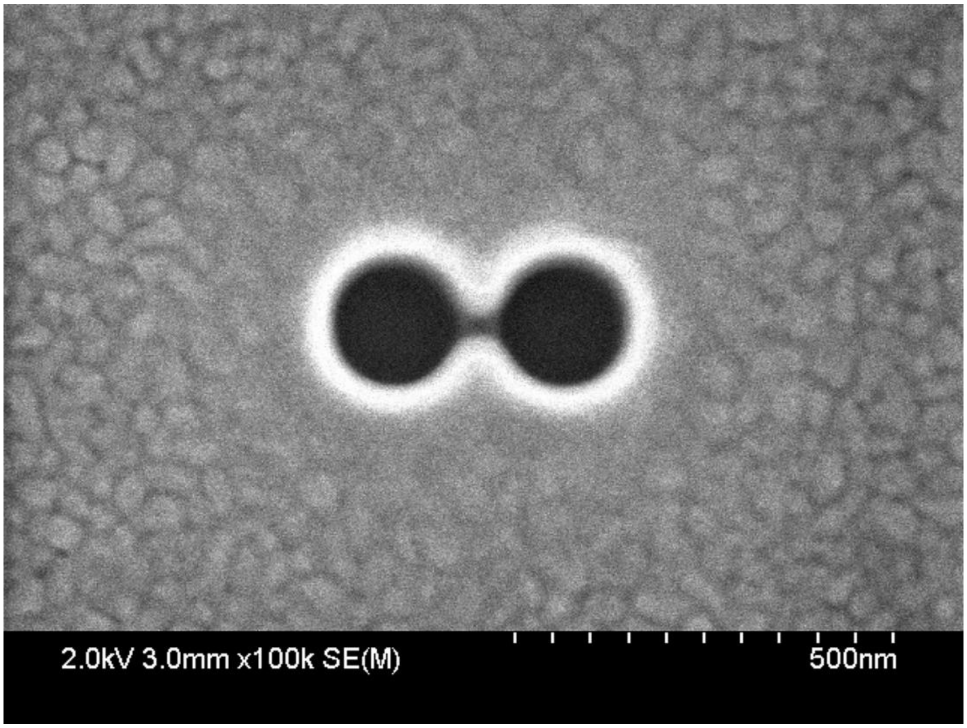

**Figure 18** – Scanning electron microscope image of a dual nanohole aperture used in trapping.

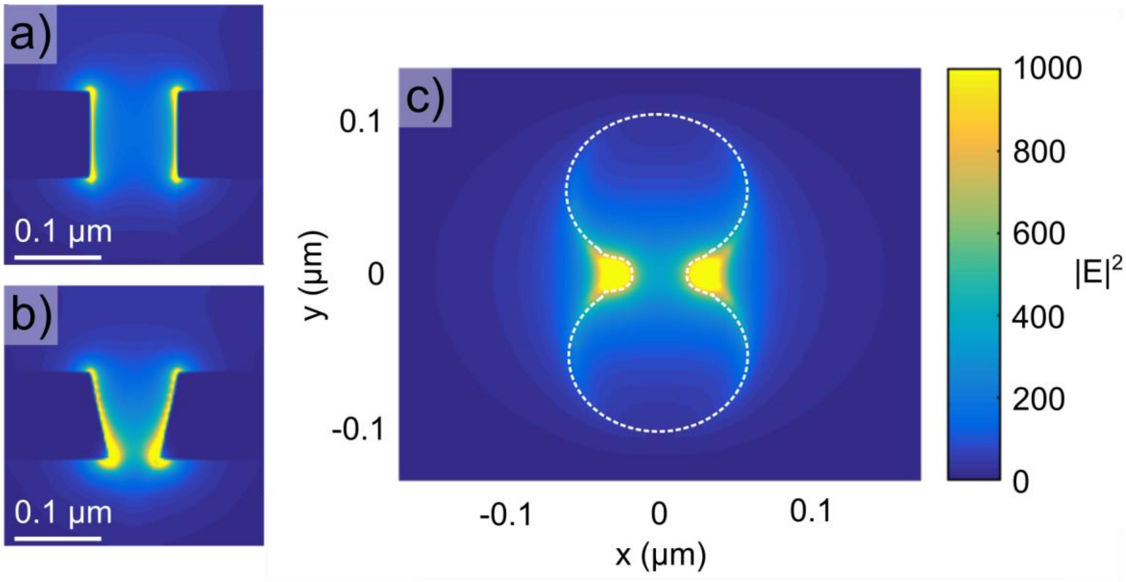

**Figure 19** – Simulation of electric field strength for a dual nanohole aperture. a) and b) show the z-profile of the aperture along the cusps ($y = 0$), while c) shows the xy-profile with the outline of the double nanohole aperture given by the dashed white line. Two different gradients for the z-profile are considered, a) for the case of a straight profile, and b) for a sloped cusp. Notice the large electric field enhancement at the cusps of the trapping aperture indicating the energetically favourable trapping location.

The DNH apertures fabricated for these experiments were made using a focused ion beam (FIB), specifically a Hitachi FB-2100 FIB[105], which uses a beam of gallium ions to mill the desired aperture into a gold film. The gold film used was 100 nm thick and was deposited onto a 5 nm titanium substrate on top of a glass slide. Because of the relatively simple structure of the DNH aperture, its features can be repeatedly fabricated to the same specifications within a high degree of tolerance. This “gap” distance can be reliably fabricated to be on the order of 20 nm, enabling effective trapping of nanoparticles on the order of tens of nanometres in diameter.  If we consider the desired DNH structure to be projected onto the x-y plane, then the z-axis indicates the depth of the aperture. The z-profile of the aperture is largely determined by the magnification (*i.e.* beam shape) used on the FIB during fabrication. The effects of different beam magnifications on the z-profile of the aperture is explored in “Appendix B”. Other trapping aperture shapes have also been explored, see “Appendix C”.

## 3.4 Sample Preparation

The basic procedure for preparing a nanoparticle sample for optical trapping is described here and summarized in Figure 20. To start, a suitable glass coverslide must be chosen; often a high NA microscope objective is required for trapping and therefore a thin coverslide must be used (typically #0, thickness = 80 – 130 µm). After the coverslide is cleaned, a microwell is created by applying a piece of double sided adhesive tape with a circular hole cut out of the middle. This adhesive spacer is approximately 100 µm thick and the circular cut out has a diameter of 9 mm, corresponding to a microwell volume of approximately 6.5 µL. Next, the nanoparticle solution must be added, typically the solution will have a concentration of nanoparticles to solvent on the order of $0.01 - 1 \times 10^{-4}\%$ weight/volume, however this will vary depending on the particular nanoparticle being used and its trapping affinity. A micropipette is used to administer the nanoparticle solution to the microwell. To avoid the formation of air bubbles in the cavity, a volume of solution $2 - 3 \times$ the microwell volume is used. Once the microwell is filled, the gold coated coverslide containing the trapping apertures is placed onto the adhesive microwell space to completely seal the microwell cavity such that the trapping aperture on the gold surface is in contact with the solution.

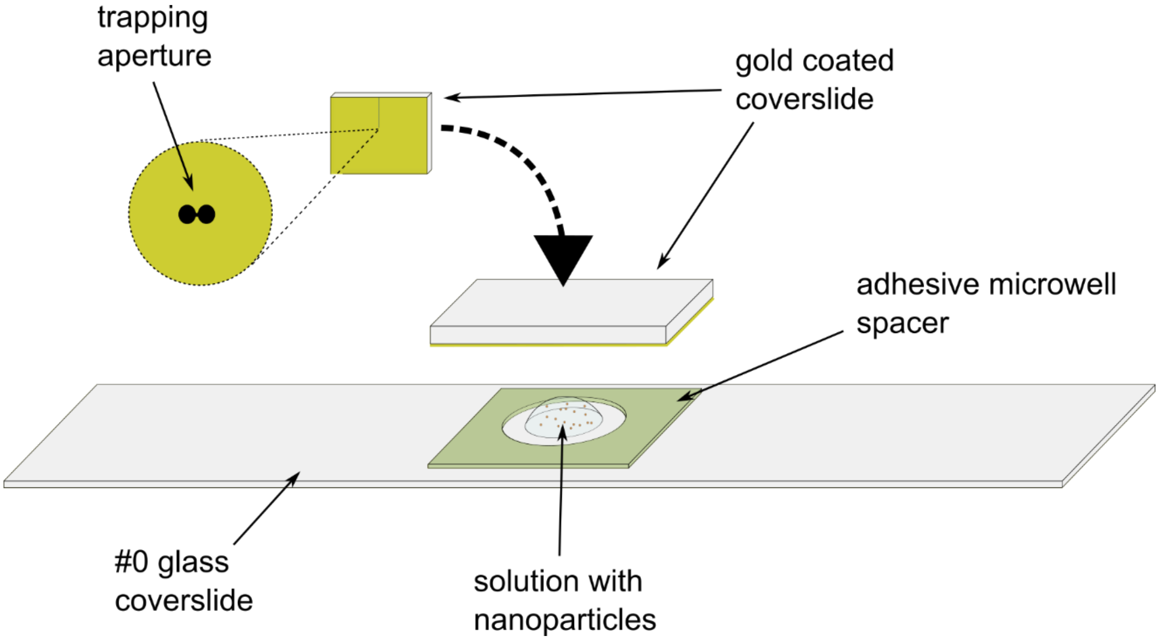

**Figure 20** – Overview of the procedure used to prepare a microscope slide for nanoparticle trapping. An adhesive microwell spacer is attached to a clean #0 glass coverslide. Next, the nanoparticle solution is inserted into the microwell, and finally the gold coated coverslide containing the trapping aperture is placed on top, creating a sealed microwell containing the nanoparticles.

From an experimental standpoint, it is important to consider the orientation of the trapping apertures with respect to the coverslide. This is because the dichroic mirror used to launch the trapping laser towards the sample is polarization sensitive, *i.e.* the power reflected by the dichroic varies depending on the ratio of s- to p-polarized light. Therefore, to get optimal trapping power at the aperture for a specific polarization angle (with respect to the trapping aperture), the orientation of the gold coated coverslide must be considered at the time of sample preparation.

## 3.5 Experimentation and Data Acquisition

After the sample has been prepared it is loaded onto the three axis stage and placed in between the microscope objectives. The LED light is turned on and the sample is viewed using a camera connected to a computer. The stage is moved until one of the fiduciary markers is located on screen (see Figure 21), once located the image is brought into focus and the trapping aperture is brought to the centre of the screen. At this point the laser is turned on and aligned for maximum transmission through the aperture using the piezoelectric controller attached to the three axis stage. Once the aperture and trapping laser are aligned, the laser is blocked and the system is left for 15-30 minutes. This time allows for the stage to settle and for the adhesive tape used in sample preparation to fully expand. Afterwards, the trapping laser and aperture are realigned, if needed, and trapping can begin.

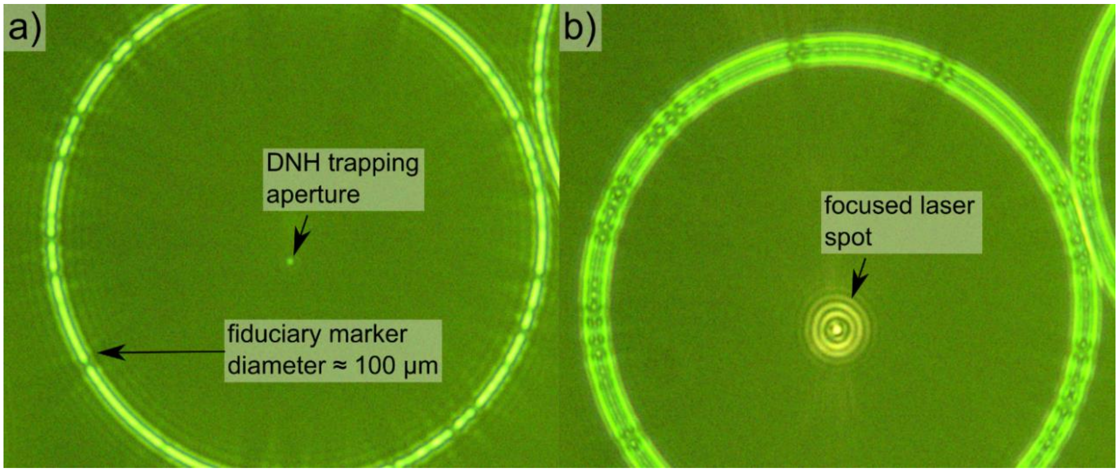

**Figure 21** – Screenshot showing the camera image of the sample during alignment. Figure a) shows the circular fiduciary marker that is used to locate the trapping aperture, the DNH trapping aperture is the bright spot in the centre of the ring. Figure b) shows the trapping laser aligned with the DNH aperture.

After the initial setup of the experiment, the transmission level as detected by the photodiode and acquired by the data acquisition unit (Advantech USB-4711a) is monitored. This information can also be seen on an attached oscilloscope. Different acquisition rates are used for different purposes; typically, if the transient data during the trap is required, acquisition rates of around 100 kHz or more are used. Conversely, acquisition rates as low a 1 kHz can be employed for more long term monitoring.

# Chapter 4 – Single Nanoparticle Raman Spectroscopy

## 4.1 Introduction

Past works in optical trapping have shown the ability of this method to localize and individually manipulate single nanoparticles[106–110]. Additionally, ultra-sensitive detection platforms with single nanoparticle sensitivity for dielectric analytes are currently being researched[111]. Several works have demonstrated single particle sensitivity using bowtie antennas,[112,113] whispering gallery modes,[114,115] and plasmonic resonance shifts[116,117]. These works often require *a priori* knowledge of the particle(s) and their surrounding environment; and lack the ability to actively isolate a single analyte particle. A platform which is capable of label free identification of a selectively isolated particle is therefore of great interest.

The integration of Raman spectroscopy with optical trapping shows great promise towards achieving this goal. Particle identification capabilities will enable the use of aperture assisted optical trapping on heterogeneous solutions, and to observe real time interactions in complex environments. Recently, a method of using two trapping lasers to electrostatically excite the ultra-low frequency vibrational modes has been demonstrated to have the potential for particle identification[54,87]. This method shows promise for investigating low frequency particle vibrations but so far has not been able to observe the conventional Raman spectra which is commonly used for identification. The concept of simultaneous trapping and Raman spectroscopy is currently being investigated by other groups[118–120].

In this work a scheme was developed to incorporate Raman spectroscopy into an optical trapping setup, using the trapping laser as the excitation source[121]. In addition to being able to isolate single nanoparticles and observe individual trapping events, the localized surface plasmons created at the trapping nanoaperture also enhanced the interaction of the analyte with the surrounding electric field causing SERS effects. The results presented here are the first published experimental observations of single 20 nm dielectric particle isolation with simultaneous Raman spectroscopy for particle identification. These results were published as a fast track communication, selected as “paper of the week”, “highlight of 2015”, and featured in a “labtalk” article by the Journal of Optics.

## 4.2 Contributions

In this experiment the author designed and built the optical trapping setup; prepared the nanoparticle solutions; acquired the trapping transmission time series; trapping integrated Raman data; and performed all data analysis. Ahmed A. Al Balushi acquired the Raman spectra for the bulk nanoparticle solutions and fabricated the trapping apertures. The published manuscript was written by the author and Reuven Gordon.

## 4.3 Optical Trapping and Raman Integration

A schematic diagram of the trapping setup, with integrated Raman capabilities, is presented in Figure 22. For the experiment presented here, a 671 nm solid-state free-space laser (Laserglow, LRS-0672-TSM-00200-10) was used for both trapping and as the Raman excitation source. The main difference in design between this configuration and that of a standard aperture based trapping setup, is the use of an additional dichroic mirror and an additional notch filter (Semrock, FF685-Di02; and Semrock, LL01-671 respectively). This allowed wavelengths longer than the trapping laser (Stokes peaks) to be transmitted to the spectrometer (Ocean Optics, QE Pro). The laser used in this instance had an output power of 100 mW which was attenuated so that there was on the order of 10 mW at the trapping site. One important note regarding the performance of the setup is that the dichroic mirror used for this setup attenuated signals out to approximately 600 cm$^{-1}$, significantly reducing the signal to noise ratio of the Stokes peaks in this region.

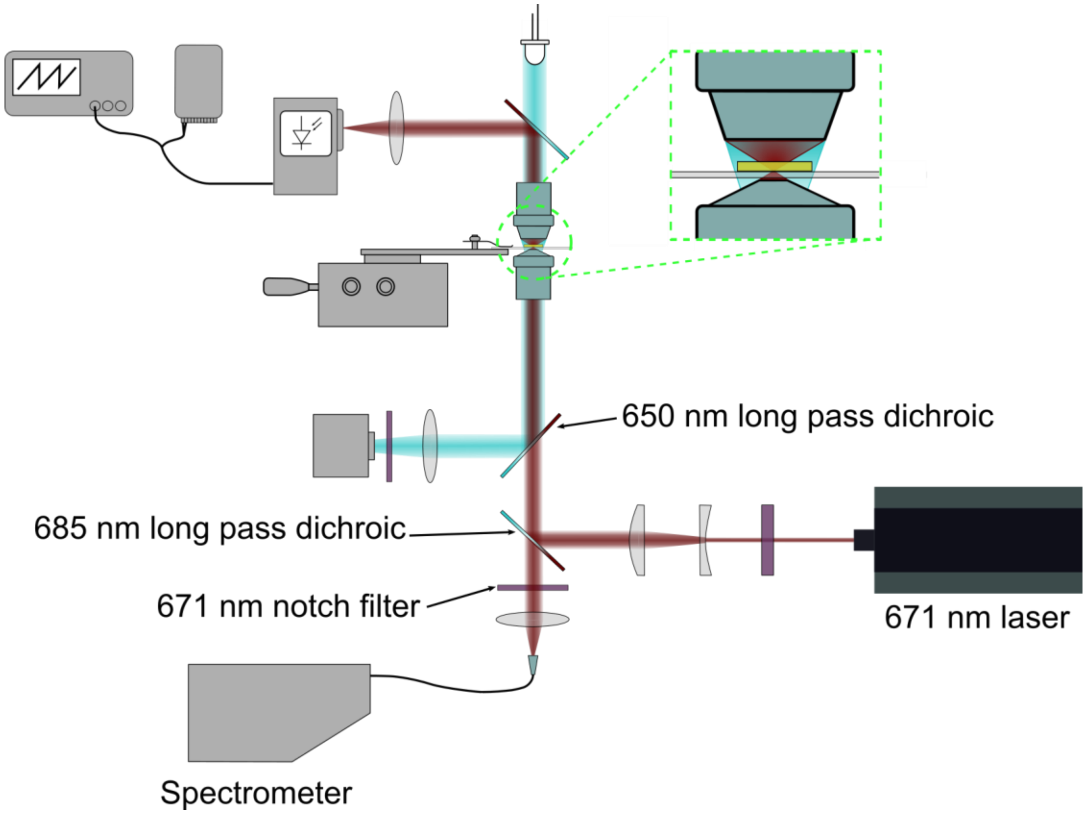

**Figure 22** – Schematic diagram of trapping setup used for integrated single particle Raman spectroscopy. The main modifications to the original setup (Figure 17) are labeled. This includes a 671 nm laser, 685 nm dichroic (long pass), a 671nm notch filter, and a spectrometer.

## 4.4 Results

The first step in performing single particle Raman spectroscopy is to isolate/trap the desired analyte (nanoparticle). In this work two types of dielectric nanoparticles were trapped and their Raman spectra observed: 20 nm titania ($TiO_2$) spheres, and 20 nm polystyrene spheres. Figure 23 shows a characteristic trapping event observed on this setup for a 20 nm polystyrene nanoparticle. To detect a trapping event, the transmission through the trapping aperture (double nanohole) must be continuously monitored. Upon trapping their will be a discrete increase in the transmission through the aperture (due to dielectric loading of the aperture) as well as a significant increase in the fluctuations in the transmission due to particle motion.

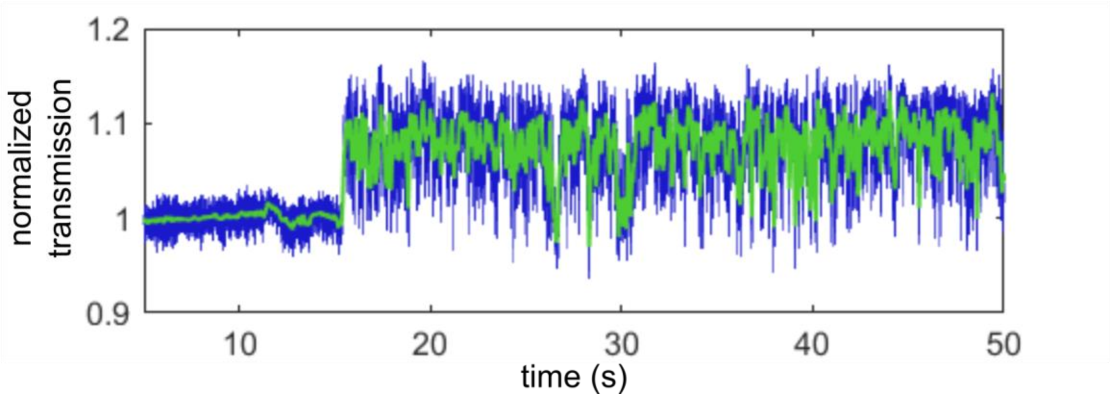

**Figure 23** – Characteristic trapping event of 20 nm polystyrene recorded with the Raman integrated trapping setup. Blue line indicates raw transmission data while the green line is the data with a Savitzky-Golay filter applied.

Before a particle is trapped, the light reflected from the aperture as seen by the spectrometer is recorded as the reference transmission spectra. These reference spectra were checked for the presence of characteristic Stokes peaks from the particles in solution. No characteristic peaks were observed. Upon trapping of a particle, the particle was required to stay in the trapped state without any additional trapping events while the Raman spectra was recorded.

For both titania and polystyrene, the raw spectrum recorded for the Raman signal in the trapped state did not show any characteristic Stokes peaks. However, when the untrapped/reference Raman spectra was subtracted from the trapped Raman spectra, the resultant difference-spectra clearly show the characteristic Stokes peaks for both titania and polystyrene (see Figure 24 and Figure 25). For the case of titania, shown in Figure 24, the low wavenumber of the characteristic Stokes peaks coincides with the wavelengths that are attenuated by the dichroic mirror just before the spectrometer. As a result, the lower wavenumber Stokes peaks are significantly more attenuated than those at larger wavenumbers. The attenuation for wavenumbers greater than 600 $cm^{-1}$ is approximately zero. Figure 24a) shows the Raman difference-spectra of the single trapped titania nanoparticle, compared to the Raman spectra for a bulk solution of titania nanoparticles. The Raman spectra of the bulk nanoparticle solution (both titania and polystyrene) was observed using a commercial Renishaw inVia, confocal Raman microscopy system using a 785 nm excitation laser. In Figure 24b) the single particle Raman spectrum has been numerically adjusted to account for the attenuation of the dichroic mirror; additionally, the slope of the background noise was removed to allow for better comparison between the single nanoparticle Raman difference-spectra, and bulk nanoparticle solution Raman spectra. As can be seen in Figure 24, the Raman difference-spectra for a single titania nanoparticle is in good agreement with that of the bulk solution, both in terms of spectral shift, and relative amplitudes of the Stokes peaks.

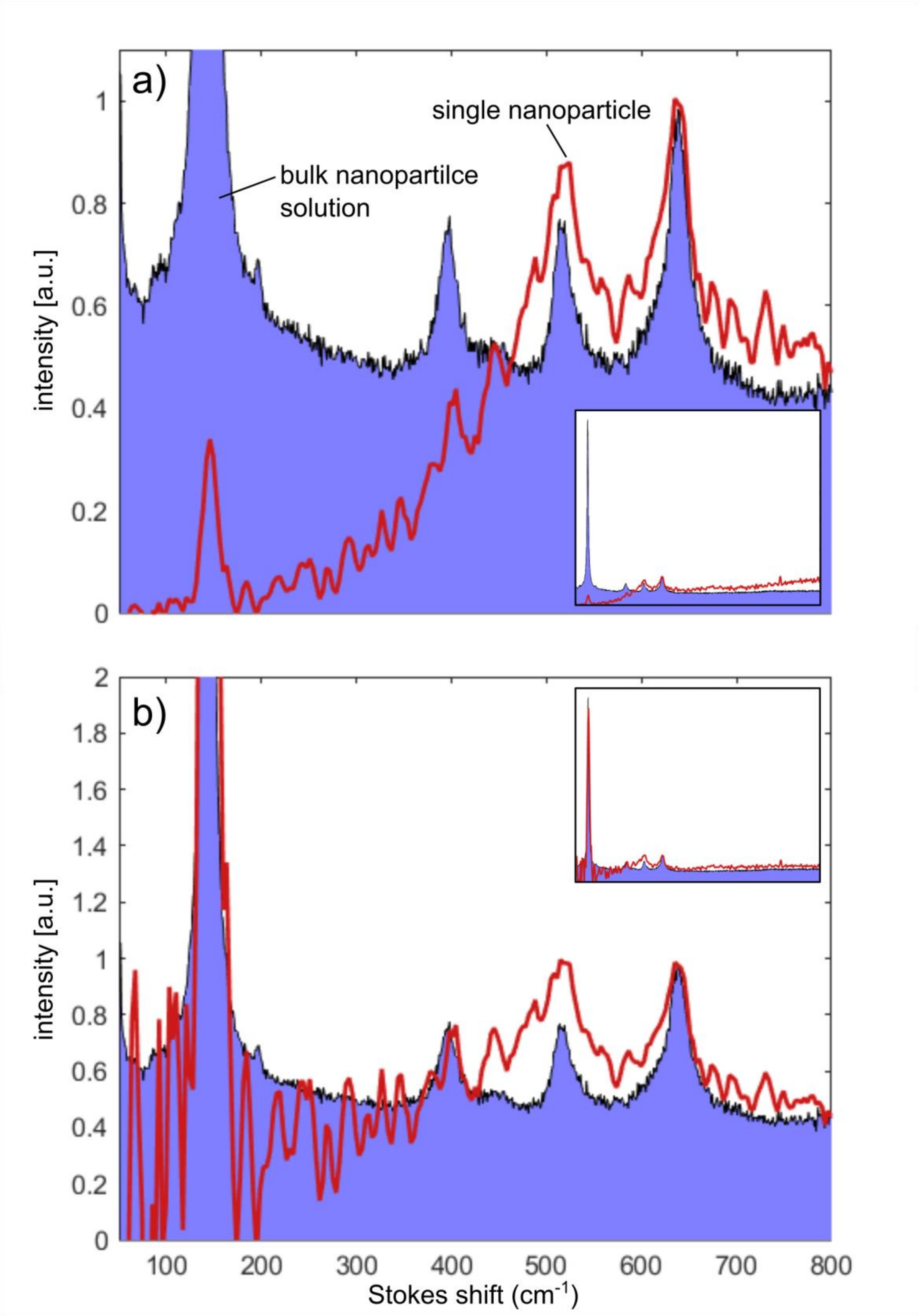

**Figure 24** – Comparison between single particle Raman spectra for single particle (red) and bulk (blue) 20 nm $TiO_2$ nanoparticles. a) shows the raw reference-subtracted Raman spectra observed

during trapping with an acquisition time of 1 minute, averaged over 18 spectra, with a Savitzky-Golay filter applied. b) is the same spectra as a) but numerically adjusted to account for attenuation in the original spectra due to the dichroic filter and to adjust the slope of the single particle spectra to match that of the bulk solution. Insets show the full spectrum from 50 to 1700 $cm^{-1}$.

The single particle Raman spectra of 20 nm polystyrene particles was also observed to demonstrate the nanoparticle identification capabilities (Figure 25). In this case the characteristic Stokes peaks of polystyrene are large enough in wavenumber that attenuation effects from the dichroic mirror are negligible. This result is in good agreement with previous published work by another group on larger polystyrene nanoparticles with significantly higher optical power[118].

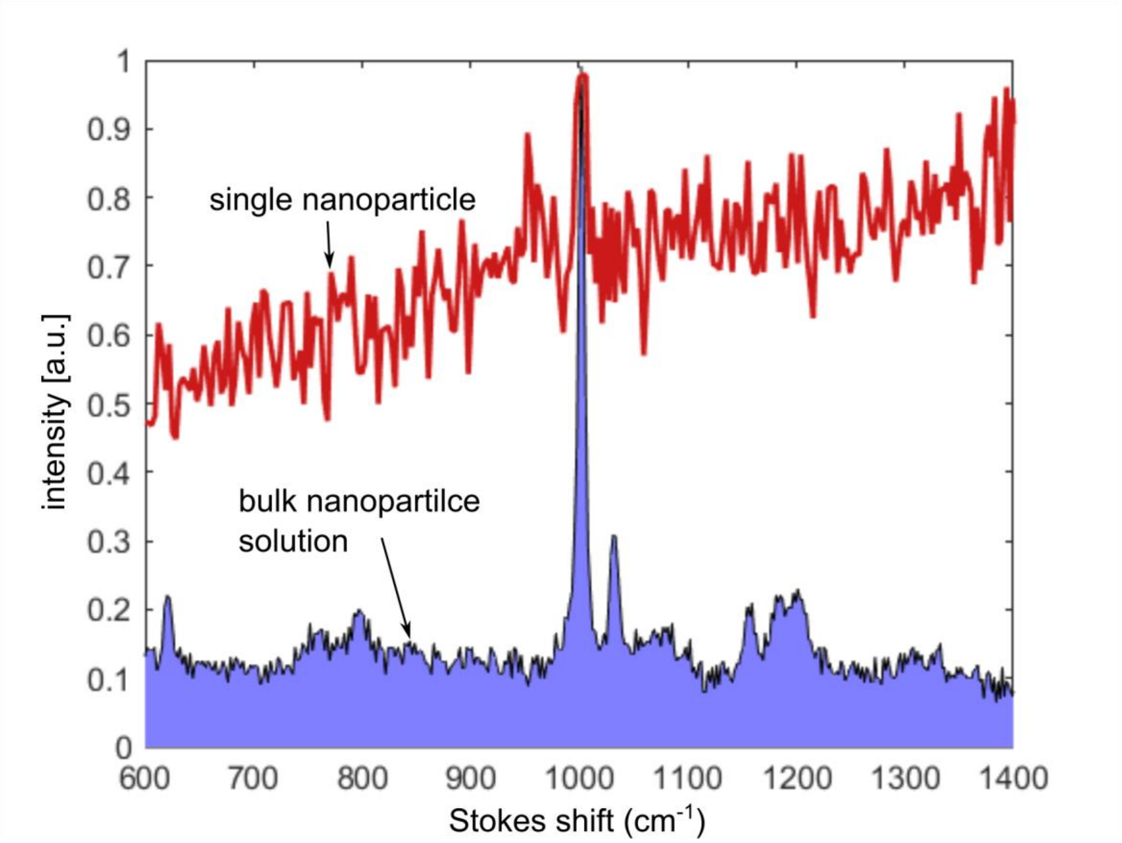

**Figure 25** – Single particle (red) and bulk (blue) Raman spectra for 20 nm polystyrene nanoparticles. The single particle spectrum is based on an average of 5 spectra with an acquisition time of 5 minutes each, and a Savitzky-Golay filter applied.

For the case of titania, where the high trapping affinity enabled multiple (and concurrent) trapping events, the Raman spectra for multiple trapped particles could be compared. The Raman difference-spectra for the untrapped, first trapping event, and second trapping event Raman difference-spectra were observed as shown in Figure 26. This result indicates the scaling of the Raman signal as multiple particles are trapped[118]. This is as expected due to the higher interaction between localized electric fields from the trapping aperture and the multiple trapped particles. Note that the first trapping event shown in Figure 26 (blue) corresponds to an entirely different trapping event on a different aperture than that shown in Figure 24 (red) and in both cases the observed single particle Raman spectra are consistent with that for the bulk nanoparticle solution.

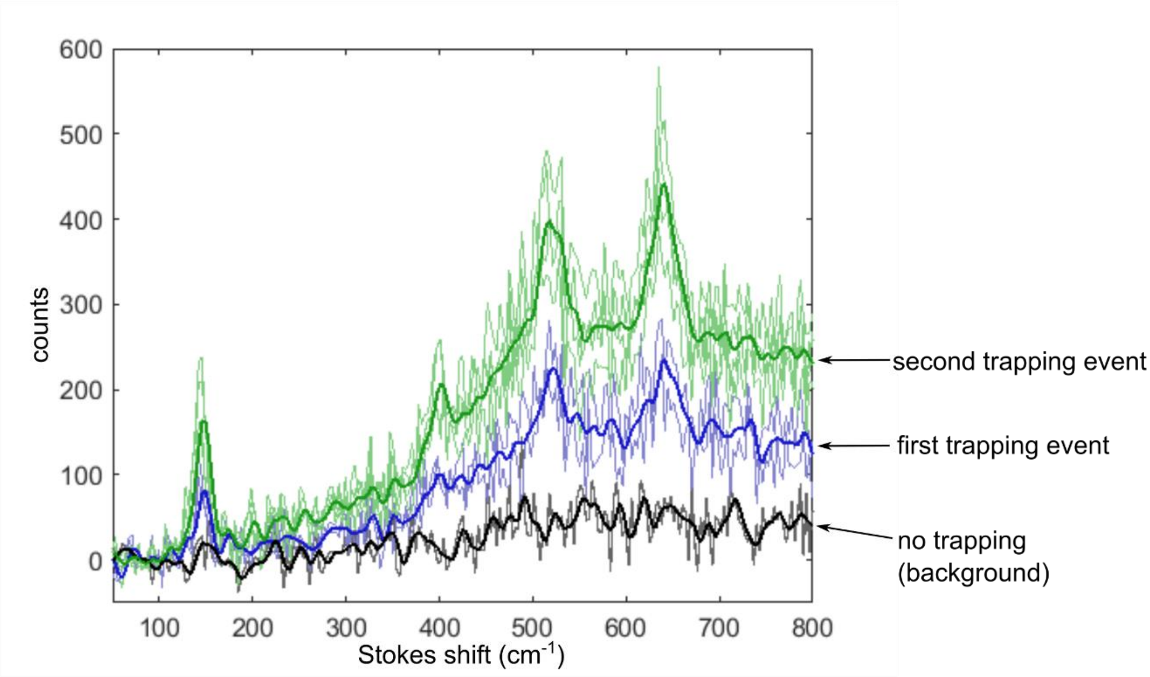

**Figure 26** – Raman difference-spectra for multiple trapping events of 20 nm $TiO_2$ nanoparticles. The black lines indicate the spectrum observed with no trapped particle. The blue lines are for the case of one trapped particle, and the green lines are for two trapped particles. Thin lines indicate raw spectra while bold lines are averaged and filtered.

## 4.5 Discussion

The results shown in Figure 24 and Figure 25 clearly indicate the resemblance of the characteristic Stokes peaks observed in conjunction with a trapping event, with those measured for the bulk nanoparticle solutions and found in literature[122,123]. These Stokes peaks correspond to unique vibrational modes of the molecules comprising the nanoparticles as discussed in Section “2.5 Raman Spectroscopy”. For instance, the Stokes peak at approximately 523 cm$^{-1}$ for titania is attributed to bending vibrations of O-Ti-O, while the peak at 150 cm$^{-1}$ is a result of symmetric stretching[124]. Similarly, for polystyrene the Stokes peak near 1000 cm$^{-1}$ is a result of the phenyl group breathing modes[125,126]. The ability to accurately determine the molecular structure of the trapped analyte, is of particular importance to nanoaperture based trapping, where the deeply subwavelength size of the analyte makes other means of identification difficult due to Abbe's diffraction limit.

Other optical trapping based methods of probing nanoparticles typically require ultra pure analyte solutions, and depend on repeatability of results to reliably give information about the trapped particle[127–129]. This is largely due to the fact that without an independent way of identifying the trapped particle, conclusions can only be made by correlating the observed phenomena to the trapping events associated with one pure analyte solution and not with a different solution. This limitation inhibits the ability of this method to be applied to heterogeneous mixtures which would be common in many biological applications. This issue can be partially overcome through the use of microfluidics but still presents a limitation to *ex vivo* use[127,128]. Conversely, the method demonstrated in this work can enable real time particle identification as well post-analysis confirmation, while permitting other methods of analysis to simultaneously be performed.

The ability for this method to have sensitivity enough to detect the intrinsically weak Raman scattering from a single dielectric nanoparticle, is due to plasmonic enhancement of the electric field in the trapping aperture. This enhancement, commonly known as SERS, is an inherent advantage of aperture based trapping where these same plasmonic hot spots are used as the trapping site. The method of aperture based trapping (see Section "2.4.3 Aperture Trapping") works to actively force the particle towards regions of higher electric field intensity. This gradient force works to automatically optimizes Raman scattering.

Using the $|E|^4$-approximation, outlined in Section "2.5.1 Surface Enhanced Raman Spectroscopy," with a typical value for the field enhancement simulated by a commercial-grade simulator based on the finite-difference time-domain method (see Figure 19), the expected Raman enhancement due to SERS is[130]

$$\text{Enhancement Factor} = \frac{|E_{\text{Loc}}|^4}{|E_{\text{Inc}}|^4} \approx (1000)^2 = 1 \times 10^6$$

For a $1 \times 10^{-4}\%$ weight per volume solution of titania in distilled water (as used in this experiment), this corresponds to an equivalent interaction volume of $1.77 \times 10^{-3}\text{cm}^3$ (in the case of no plasmonic enhancements). The laser interaction volume, is the volume which corresponds to the conical region of the solution that the laser interacts with, as defined by the NA of the microscope objective and depth of microwell. This setup used a $50 \times$ Mitutoyo infinity corrected objective was used as the condenser objective (NA = 0.75) and a $100$ μm microwell depth. Therefore, the laser interaction volume is approximately $0.5 \times 10^{-6}\text{cm}^3$. The equivalent interaction volume of the trapped particle (cause by plasmonic enhancements) is several orders of magnitude larger than the laser interaction volume. This simple calculation highlights the selectivity of the setup to observe the trapped analyte but not the surrounding solution.

### 4.6 Summary

Presented in this section was a method of incorporating Raman spectroscopy into an aperture assisted optical trapping setup. The trapping laser was simultaneously used as the excitation source for Raman scattering and a series of filters was used to isolate the Stokes peaks. Raman spectra for two different nanoparticles was obtained (titania and polystyrene, both 20 nm diameter) which was correlated to trapping events of individual nanoparticles. The Raman spectra obtained for the trapped nanoparticles correlates well with the conventional Raman spectra observed for the bulk nanoparticle solution. The sensitivity required to observe the Raman scattering from individual nanoparticles results from plasmonic enhancements which occur at the trapping aperture. This work demonstrates the ability for an aperture assisted optical trapping setup to independently identify the trapped particle, a functionality that is highly desirable for the implementation of this method on heterogeneous analyte solution.

# Chapter 5 – Characterization of Magnetic Nanoparticles

## 5.1 Introduction

In this experiment an aperture assisted optical trapping setup was integrated with an applied magnetic field (Optical Trapping with Magnetic Field – OTMF) to fully characterize magnetic nanoparticles in solution[131]. More information about magnetic nanoparticles is provided in "Appendix D". Quantitative analysis was performed to determine the complex refractive index, magnetic susceptibility, remanence, and ultimately an empirical size distribution of superparamagnetic magnetite ($Fe_3O_4$) nanoparticles. These results demonstrate the ability of an aperture assisted trapping platform to selectively analyze single nanoparticles *via* interactions external to the trapping mechanism. This work has applications in the study of heterogeneous solutions containing magnetic nanoparticles, including the ability to selectively isolate magnetic nanoparticles with the desired characteristics. The work presented here was published by the scientific journal Nano Letters.

## 5.2 Contributions

In this work the author fabricated the trapping apertures, assisted with setup modification, and imaged the nanoparticles with the scanning electron microscopy. Data acquisition and analysis was performed by Haitian Xu. The manuscript was written by Haitian Xu with assistance from the author, Byoung-Chul Choi, and Reuven Gordon.

## 5.3 Optical Trapping and Magnetic Field Integration

Only very slight modifications to the standard aperture assisted optical trapping setup were required to probe the magnetic properties of the nanoparticles (see Figure 27), illustrating the versatility of this trapping method. The optical trapping setup used here included a $100 \times$ oil immersions condenser objective ($NA = 1.25$), and an 855 nm trapping laser

(Eagleyard DFB-0855) with optical power of 8.25 mW at the trapping site. A current controlled non-saturating magnetic field was generated from a small external electromagnet with an applied field ranging from 0 to 27.85 kA/m. A double nanohole (DNH) aperture with a hole diameter of 200 nm and a cusp separation of around 35 nm was used for trapping. After trapping data acquisition, a sample of magnetic nanoparticles was spin-coated on a gold coverslide and imaged using scanning electron microscopy (Hitachi S-4800) to independently measure the size distribution. The magnetite nanoparticles used have a specified mean diameter of 30 nm (747408 Sigma-Aldrich) and were used with a concentration of $10^{-3}$ % wt/vol.

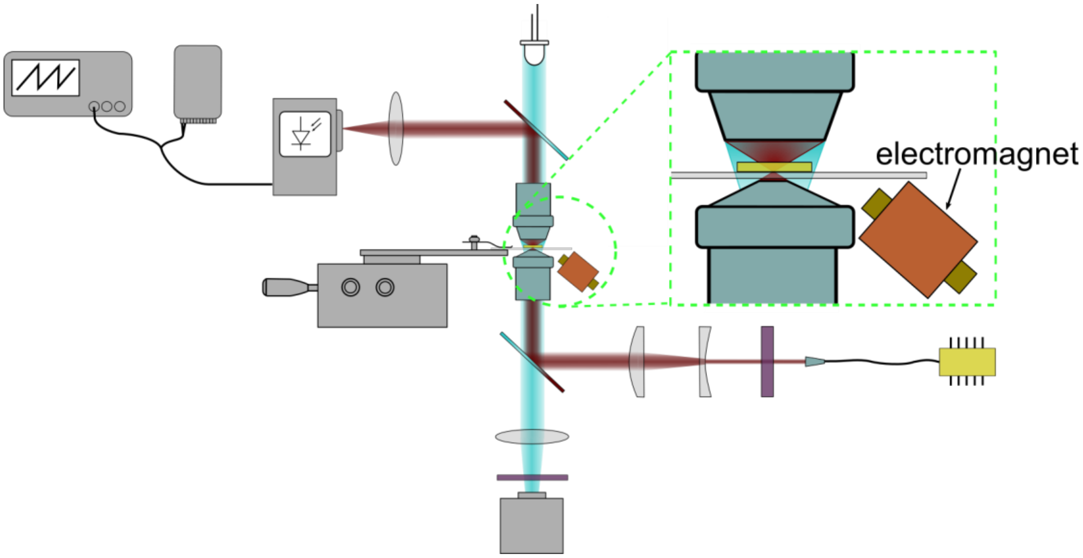

**Figure 27** – Optical trapping with magnetic field setup (OTMF). The electromagnet used to probe the nanoparticles was placed near the trapping site but external from the trapping setup. The orientation is such that the applied magnetic force works to pull trapped magnetic nanoparticle out of the trap, towards the microwell.

### 5.4 Results and Analysis

Figure 28 show the trapping time series for the magnetite nanoparticles including the trapping event ($t = 5$ s) and the application of a magnetic field once trapped ($t = 10$ s).

The effects of the applied magnetic field can clearly be seen as a significant increase in the range of the transmission intensity distribution (as measured by the APD).

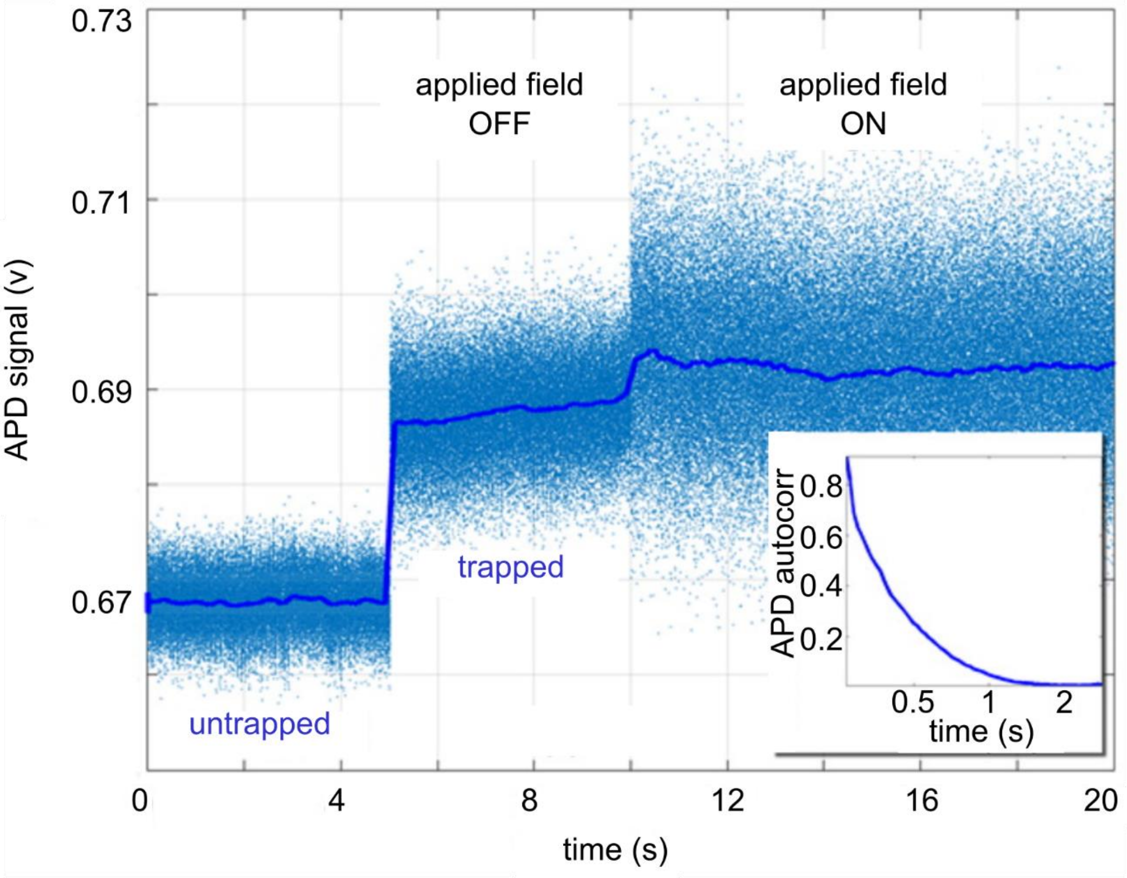

**Figure 28** – Transmission through DNH aperture over time as measured by the APD at 20 kHz acquisition rate. The untrapped, trapped, and trapped with applied magnetic field situations are shown. The solid blue line in the transmission time series is a moving average with a 2000-point window. Inset shows a typical autocorrelation curve of the transmission for a particle in the trapped state.

The real part of the refractive index can be found by comparing the transmission change upon trapping for the magnetite nanoparticles with trapping events for similarly sized polystyrene nanoparticles (mean diameter = 30 nm, Thermo Scientific 3030A). To first order, the transmission change through the nanoaperture upon trapping is linearly related to the Clausius-Mossotti factor as previously reported[129]. Simulations have shown the transmission change upon trapping to be negligibly affected by the imaginary part of the refractive index for magnetite particles, and the imaginary component for polystyrene is near zero[131]. Using the Clausius-Mossotti factor which determines the polarizability of a subwavelength sphere an empirical value for the magnetite refractive index can be obtained as

$$\text{Clausius-Mossotti factor} = \frac{\epsilon_{\text{particle}} - \epsilon_{\text{med}}}{\epsilon_{\text{particle}} + 2\epsilon_{\text{med}}}, \tag{5.1}$$

where $\epsilon_{\text{med}} = 1.77$ (water) and $\epsilon_{\text{particle}}$ is the relative permittivity of the trapped particle ($\epsilon_{\text{particle}} = 2.46$ for polystyrene)[132]. Under this approximation the refractive index of the trapped magnetite nanoparticles is found to be $\text{Re[n]} = \text{Re}[\sqrt{\epsilon_r}] = 1.89$ which is in reasonable agreement with other reported values[133,134].

The transmission fluctuations in the trapped state can give information about the motion of the trapped particle and hence the forces acting upon it. Due to Brownian motion, displacement of the trapped particle from the trapping site varies according to Boltzmann's distribution, *i.e.*[132]

$$\text{P} \propto \text{e}^{\frac{-U(x)}{k_B T}} \tag{5.2}$$

Where the potential energy of the trap is approximated by[135]

$$U(x) = \kappa\left(ax + \frac{x^2}{2} + bx^3 + cx^4\right) \tag{5.3}$$

Here, $\kappa$ is the trap stiffness calculated from autocorrelation analysis of the transmission with no applied magnetic field (see Figure 28 inset)[136]. The parameters $a, b,$ and $c$ are fitting constants. The voltage distributions for different applied magnetic fields, as well as the fit to the probability distribution are shown in Figure 29.

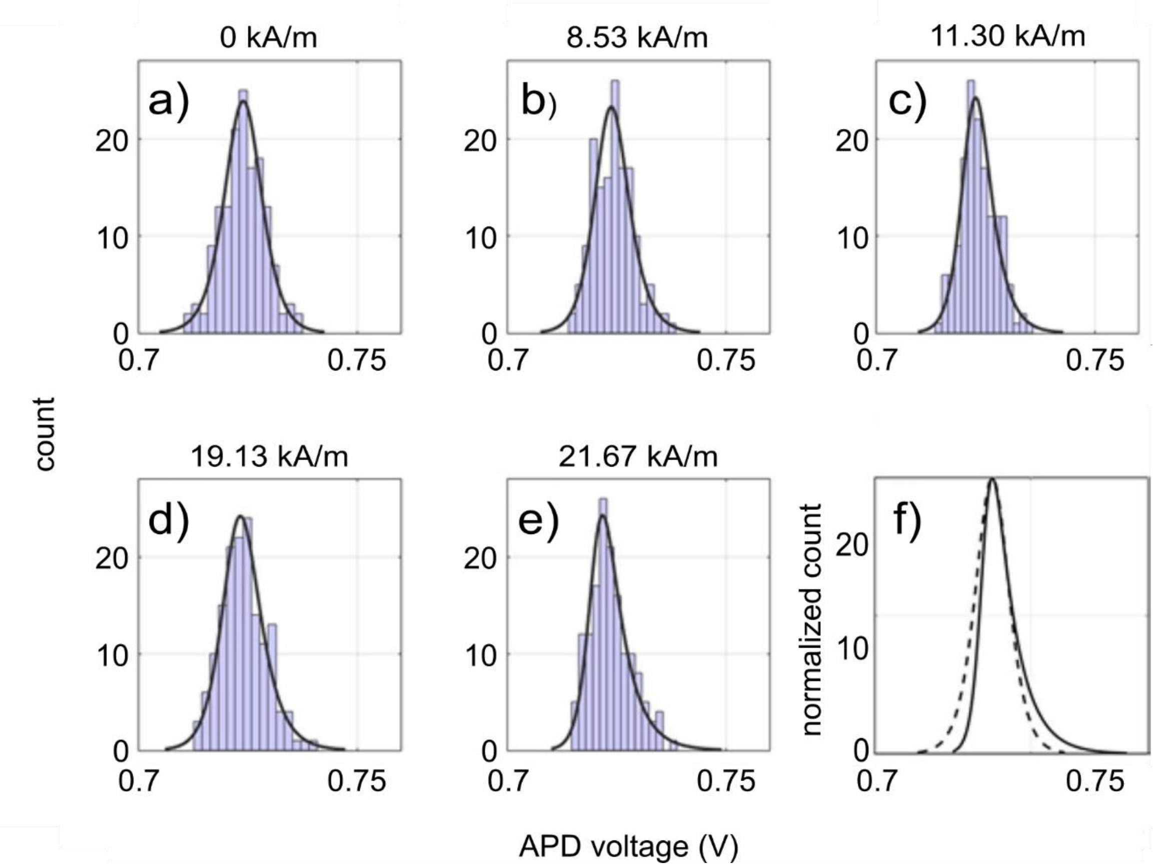

**Figure 29** – a) to e) voltage distribution as measured by APD for a single trapping event under various applied fields. f) normalized fitting curves for $H = 0$ kA/m (dotted) and $H = 24.16$ kA/m (solid line). Notice the skewness towards higher transmission values with increasing applied magnetic field.

For the case of a harmonic potential (*i.e.* no applied magnetic field), $a$ is taken as zero and the probability distribution is nearly Gaussian (Figure 29a). The constants $b,$ and $c$ are included to ensure a good fit to the experimental data.

The motion of the particle in the trap can be modelled by and over-damped Langevin equation, *i.e.*[137]

$$\frac{dx(t)}{dt} = -\frac{\kappa}{\gamma}x(t) + \left(\frac{2k_B T}{\gamma}\right)^{\frac{1}{2}}\eta(t) \tag{5.4}$$

The displacement from equilibrium is given by $x(t)$, $\kappa$ is the stiffness of the optical trap, $\gamma$ is the drag, and $\eta(t)$ is a noise term. By taking the autocorrelation of the transmission time series (when the particle is trapped), we can relate the time constant ($\tau$) to the stiffness of the trap according to[138]

$$\tau = \frac{\gamma}{\kappa} \tag{5.5}$$

The trap stiffness is proportional to the applied forces, and therefore also proportional to the complex Clausius-Mossotti factor. By taking the ratio of the trap stiffness for the 30 nm magnetite nanoparticle, and for the 30nm polystyrene sphere we can determine the imaginary component of the refractive index. The experimental value for the imaginary component of the refractive index for magnetite is $\mathrm{Im}[n] = 0.73$ at a wavelength of $855$ nm. This value is approximately 28% lower than the reference data. A possible explanation for this discrepancy is that the nanoparticles used have been suggested to be larger than specification ($\approx 31$ nm as suggested by Wheaton *et al.*[54]).

Due to the configuration of the trapping setup the applied magnetic field acts to pull the trapped magnetite particle out of the aperture causing the linear term in the trap potential to be less than zero ($a < 0$). The force on the trapped magnetite particle by the gradient of the applied magnetic field can therefore be approximated as

$$F_M = \kappa a \tag{5.6}$$

Using the values for the constant $a$ determined by fitting the distributions shown in Figure 29 the force exerted on the trapped nanoparticle due the applied field can be determined as shown in Figure 30.

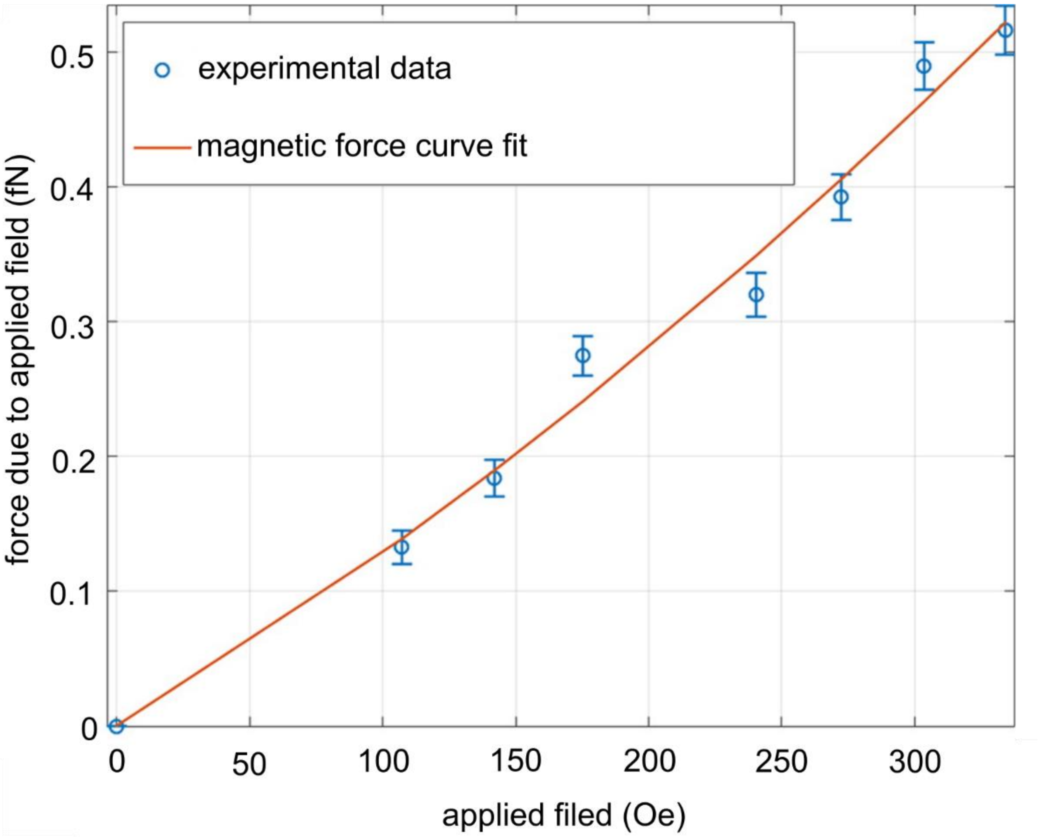

**Figure 30** – Magnetic force acting on the trapped magnetite nanoparticle as a function of the applied magnetic field.

The force on a magnetic particle due to an applied magnetic field is expressed as[139]

$$F_M = \frac{V\chi}{\mu_0}(B \cdot \nabla)B + \rho V \nabla (M_0 \cdot B) \tag{5.7}$$

Here, $V$ is the volume of the magnetic nanoparticle, $\chi$ is the susceptibility, $\rho$ is the density, and $M_0$ is the remanence of the nanoparticle. The z-component of the magnetic field was measured experimentally and determined to be linear, therefore the magnetic force on the particle along the z-direction can be written as

$$F_M = \frac{V\chi}{\mu_0}(B \cdot C_0 B) + \rho V M_0 (C_0 B) = C_1 B^2 + C_2 B \tag{5.7}$$

The curve fits shown in Figure 30 are based on the above equation, and results in experimental values of $C_1$ and $C_2$ allowing for the determination of the susceptibility ($\chi = 7.8$) and remanence ($M_0 = 13.1\ \mathrm{Am}^2/\mathrm{kg}$) of the nanoparticle which are comparable to published values that used vibrating sample magnetometry (see “Appendix E” for more information)[140–142]. Note that the mean diameter of 30 nm was used to determine the volume in this calculation.

This analysis was performed on 12 separate trapping events under a constant laser power for applied magnetic fields ranging from 8.53 kA/m to 26.58 kA/m. Using the calculated values for the susceptibility, remanence, and magnetic force, a size distribution was obtained for the trapped particles as shown in Figure 31. The size distribution obtained *via* this analysis is in good agreement with the distribution measured using a scanning electron microscope on a dilute solution of magnetite nanoparticle spin-coated onto a gold coverslide as shown in Figure 31.

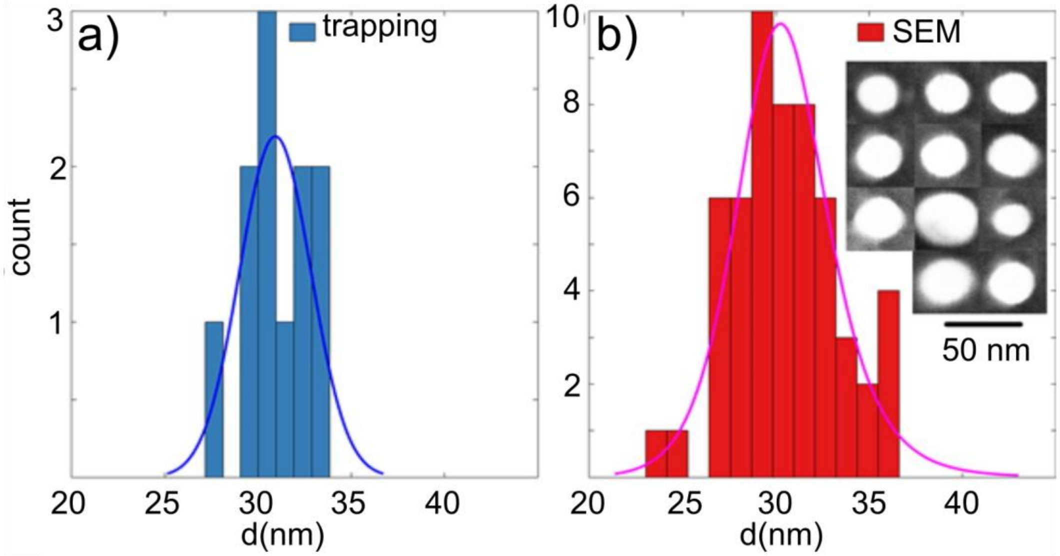

**Figure 31** – a) calculated size distribution for magnetite nanoparticles based on 12 trapping events. b) measured size distribution of magnetite nanoparticles using scanning electron microscope.

### 5.5 Summary

In this Chapter the method of optical trapping with magnetic field (OTMF) was demonstrated to characterize individual magnetite nanoparticles (30 nm diameter). Using this method, the complex refractive index, magnetic susceptibility, remanence, and size distribution were determined using only the average expected size of the nanoparticle a prior knowledge. The experimentally obtained values are in reasonable agreement with those reported in the literature. This work demonstrates the versatility of an optical trapping setup to probe the magnetic properties of materials in a label free environment.

# Chapter 6 – Conclusion

The method of optical trapping, specifically aperture assisted trapping, is an exciting technique that allows scientists an unprecedented ability to probe nanoscale particles. This method utilizes the minute but significant optical forces that are generated by spatially varying electric field intensities. Due to the extremely small scale of the particles being isolated, they are inherently below the diffraction limit. Additionally, dielectric particles on the nanoscale scatter light weakly.  Because of this, it is very difficult to *see* the properties of these dielectric nanoparticles. As a result, the method has thus far been limited in its use to extremely pure dilutions of the analyte, inhibiting its range of applications.

The work presented in this thesis was conducted with the goal of seeing what cannot be seen. To go beyond the diffraction limit and optically detect the properties of a deeply subwavelength nanoparticle. The ability to independently characterize a nanoparticle once trapped enables aperture assisted trapping to be performed on a much broader class of scientific experiments and lends greater credence to past results. To this end two experiments were performed: Raman spectroscopy on individual dielectric nanoparticles, and magnetic characterization of single superparamagnetic nanoparticles.

In the first experiment, an optical trapping setup was modified to incorporate Raman spectroscopy. The trapping laser was used as the excitation source, and the plasmonic fields generated at the trapping aperture were used to enhance the intrinsically weak Raman signal. Using a system of dichroic filters, the redshifted light scattered by the trapped analyte were able to be extracted and measured by a spectrometer. The spectra recorded while a particle was trapped, showed characteristic spectral peaks that are well known to correspond to the material of the particle being trapped. The correlation between these spectral peaks and a particle being trapped, and their absence otherwise, illustrates the extreme sensitivity of the aperture assisted trapping method to the particle localized at the trapping aperture.

During the characterization of magnetic nanoparticles, external magnetic fields were applied while a particle was trapped. The effects of this external field could be directly observed by fluctuations in the transmission of light through the aperture. By correlating these changes in the transmission distribution to the applied magnetic field, a relationship was observed enabling us to ascertain the susceptibility, remanence, and size of the trapped particles. Additionally, the refractive index of the particle was determined by comparing the trapping events to those of other dielectric nanoparticles.

These works contribute to the advancement of the field of optical trapping, and extend its capabilities at the nanometer scale.

# Chapter 7 – Future Outlook

Optical trapping, while showing great promise in its ability to probe nanoscale objects, is not without its limitations. The conventional optical trapping setup is essentially a modified inverted microscope, and as such presents a constraint on its size and portability. Additionally, the same sensitivity that enables it to probe single nanoparticles also makes it extremely susceptible to vibrations and other sources of noise, reducing its applicability outside of the laboratory. Potentially the most significant challenge this method faces, is its relatively low throughput and the associated cost/complexity of scaling up the device in its current form.

The integration of optical trapping with fibre optics has the ability to address all of these issues. By fabricating a trapping aperture on the tip of a fibre, the size and portability can be significantly improved, enabling the possibility of high throughput optical trapping setups. This method would also enable transportation of trapped particles while simultaneously characterizing their properties.

Several groups are currently working to transform optical trapping into a fibre integrated setup. In 2007 Liberale *et al*. demonstrated purely optical trapping of 10μm polystyrene beads using a bundle of four optical fibres to balance the optical forces[143]. The method of using tapered fibers has been used in biological trapping applications on the micrometer scale such as yeast and E-coli[144,145]. The integration of aperture assisted trapping with optical fibers has been demonstrated to enable the trapping of nanoscale particles using bowtie or double nanohole apertures[146,147].

# Bibliography

1. Chu, B. Laser Light Scattering. *Annual Review of Physical Chemistry* 21, 145–174 (1970).

2. Goldburg, W. I. Dynamic light scattering. *American Journal of Physics* 67, 1152 (1999).

3. Kulikov, K. G. & Koshlan, T. V. Measurement of Sizes of Colloid Particles Using Dynamic Light Scattering. *Theoretical and Mathematical Physics* 60, 26–32 (2015).

4. Pecora, R. Dynamic light scattering measurement of nanometer particles in liquids. *Journal of Nanoparticle Research* 2, 123–131 (2000).

5. Zakharov, P. & Scheffold, F. Advances in dynamic light scattering techniques. *Light Scattering Reviews 4* 433–467 (2009).

6. Borsali, R. & Pecora, R. *Soft Matter Characterization*. *Physics and Astronomy* (2008).

7. Maier, S. A. *Plasmonics: Fundamentals and applications*. *Plasmonics: Fundamentals and Applications* (2007).

8. Shalaev, V. M. & Kawata, S. *Nanophotonics with Surface Plasmons*. *Nanophotonics with Surface Plasmons* (2007).

9. Homola, J. *Surface Plasmon Resonance Based Sensors*. *Springer Series on Chemical Sensors and Biosensors* 04, (2006).

10. Homola, J. Present and future of surface plasmon resonance biosensors. *Anal Bioanal Chem* 377, 528–539 (2003).

11. Matsubara, K., Kawata, S. & Minami, S. A Compact Surface Plasmon Resonance Sensor for Measurement of Water in Process. *Applied Spectroscopy* 42, 1375–1379 (1988).

12. Zhang, L. M. & Uttamchandani, D. Optical chemical sensing employing surface plasmon resonance. *Electronics Letters* 24, 1469–1470 (1988).

13. Nylander, C., Liedberg, B. & Lind, T. Gas detection by means of surface plasmon resonance. *Sensors and Actuators* 3, 79–88 (1982).

14. Brockman, J. M., Nelson, B. P. & Corn, R. M. Surface plasmon resonance imaging measurements of ultrathin organic films. *Annu Rev Phys Chem* 51, 41–63 (2000).

15. de Mol, N. J., Plomp, E., Fischer, M. J. & Ruijtenbeek, R. Kinetic analysis of the mass transport limited interaction between the tyrosine kinase lck SH2 domain and

a phosphorylated peptide studied by a new cuvette-based surface plasmon resonance instrument. *Analytical biochemistry* 279, 61–70 (2000).

16. Fisher, R. D. *et al.* Structure and ubiquitin binding of the ubiquitin-interacting motif. *Journal of Biological Chemistry* 278, 28976–28984 (2003).

17. McDonnell, J. M. Surface plasmon resonance: towards an understanding of the mechanisms of biological molecular recognition. *Curr. Opin. Chem. Biol.* 5, 572–577 (2001).

18. Oshannessy, D. J., Brighamburke, M., Soneson, K. K., Hensley, P. & Brooks, I. Determination of Rate and Equilibrium Binding Constants for Macromolecular Interactions Using Surface Plasmon Resonance: Use of Nonlinear Least Squares Analysis Methods. *Analytical Biochemistry* 212, 457–468 (1993).

19. Halpern, A. R., Wood, J. B., Wang, Y. & Corn, R. M. Single-nanoparticle near-infrared surface plasmon resonance microscopy for real-time measurements of DNA hybridization adsorption. *ACS Nano* 8, 1022–1030 (2014).

20. Ferraro, J. R., Nakamoto, K. & Brown, C. W. *Introductory Raman Spectroscopy*. *Direct* (2003).

21. Baranska, M., Roman, M. & Majzner, K. *Optical Spectroscopy and Computational Methods in Biology and Medicine*. (Springer, 2014).

22. Sepúlveda, B., Angelomé, P. C., Lechuga, L. M. & Liz-Marzán, L. M. LSPR-based nanobiosensors. *Nano Today* 4, 244–251 (2009).

23. Lee, K. S. & El-Sayed, M. A. Gold and silver nanoparticles in sensing and imaging: sensitivity of plasmon response to size, shape, and metal composition. *Journal of Physical Chemistry B* 110, 19220–19225 (2006).

24. Nehl, C. L., Liao, H. & Hafner, J. H. Optical properties of star-shaped gold nanoparticles. *Nano Letters* 6, 683–688 (2006).

25. Pastoriza-Santos, I., Sánchez-Iglesias, A., De Abajo, F. J. G. & Liz-Marzán, L. M. Environmental optical sensitivity of gold nanodecahedra. *Advanced Functional Materials* 17, 1443–1450 (2007).

26. Burgin, J. *et al.* 3D morphology of Au and Au@Ag nanobipyramids. *Nanoscale* 4, 1299–1303 (2012).

27. Kreuzer, M. P., Quidant, R., Salvador, J. P., Marco, M. P. & Badenes, G. Colloidal-based localized surface plasmon resonance (LSPR) biosensor for the quantitative determination of stanozolol. *Analytical and Bioanalytical Chemistry* 391, 1813–1820 (2008).

28. Marinakos, S. M., Chen, S. & Chilkoti, A. Plasmonic detection of a model analyte in serum by a gold nanorod sensor. *Analytical Chemistry* 79, 5278–5283 (2007).

29. Frederix, F. *et al.* Biosensing based on light absorption of nanoscaled gold and silver particles. *Analytical chemistry* 75, 6894–6900 (2003).

30. Zybin, A. *et al.* Real-time detection of single immobilized nanoparticles by surface plasmon resonance imaging. *Plasmonics* 5, 31–35 (2010).

31. Gurevich, E. L., Temchura, V. V., Überla, K. & Zybin, A. Analytical features of particle counting sensor based on plasmon assisted microscopy of nano objects. *Sensors and Actuators, B: Chemical* 160, 1210–1215 (2011).

32. Shpacovitch, V. *et al.* Application of surface plasmon resonance imaging technique for the detection of single spherical biological submicrometer particles. *Analytical Biochemistry* 486, 62–69 (2015).

33. Wang, S. *et al.* Label-free imaging, detection, and mass measurement of single viruses by surface plasmon resonance. *Proceedings of the National Academy of Sciences of the United States of America* 107, 16028–32 (2010).

34. Sannomiya, T., Hafner, C. & Voros, J. In situ sensing of single binding events by localized surface plasmon resonance. *Nano Letters* 8, 3450–3455 (2008).

35. Le Ru, E. C. & Etchegoin, P. G. *Principles of Surface-Enhanced Raman Spectroscopy*. *Principles of Surface-Enhanced Raman Spectroscopy* (2009).

36. Neubrech, F. & Pucci, A. *Nanoantenna: Plasmon-Enhanced Spectroscopies for Biotechnological Applications*. (Pan Stanford Publishing Pte. Ltd., 2013).

37. Zhang, Y. *et al.* Coherent anti-Stokes Raman scattering with single-molecule sensitivity using a plasmonic Fano resonance. *Nature Communications* 5, 4424 (2014).

38. Ebbesen, T. W. *et al.* Extraordinary optical transmission through sub-wavelength hole arrays. *Nature* 86, 1114–7 (1998).

39. Genet, C. & Ebbesen, T. W. Light in tiny holes. *Nature* 445, 39–46 (2007).

40. Gao, H., Henzie, J. & Odom, T. W. Direct evidence for surface plasmon-mediated enhanced light transmission through metallic nanohole arrays. *Nano Letters* 6, 2104–2108 (2006).

41. Gordon, R., Sinton, D., Kavanagh, K. L. & Brolo, A. G. A New Generation of Sensors Based on Extraordinary Optical Transmission. *Accounts of Chemical*

*Research* 41, 1049–1057 (2008).

42. Brolo, A. G., Gordon, R., Leathem, B. & Kavanagh, K. L. Surface plasmon sensor based on the enhanced light transmission through arrays of nanoholes in gold films. *Langmuir : the ACS journal of surfaces and colloids* 20, 4813–4815 (2004).

43. Tetz, K. a, Pang, L. & Fainman, Y. High-resolution surface plasmon resonance sensor based on linewidth-optimized nanohole array transmittance. *Optics letters* 31, 1528–1530 (2006).

44. Brolo, A. G., Arctander, E., Gordon, R., Leathem, B. & Kavanagh, K. L. Nanohole-enhanced raman scattering. *Nano Letters* 4, 2015–2018 (2004).

45. Reilly, T. H., Chang, S.-H., Corbman, J. D., Schatz, G. C. & Rowlen, K. L. Quantitative Evaluation of Plasmon Enhanced Raman Scattering from Nanoaperture Arrays. *Journal of Physical Chemistry C* 111, 1689–1694 (2007).

46. Coe, J. V. *et al.* Metal films with arrays of tiny holes: Spectroscopy with infrared plasmonic scaffolding. *Journal of Physical Chemistry C* 111, 17459–17472 (2007).

47. Ashkin, A. Acceleration and Trapping of Particles by Radiation Pressure. *Physical Review Letters* 24, 156–159 (1970).

48. Maragò, O. M. *et al.* Femtonewton force sensing with optically trapped nanotubes. *Nano Letters* 8, 3211–3216 (2008).

49. Tong, L., Miljković, V. D., Johansson, P. & Käll, M. Plasmon hybridization reveals the interaction between individual colloidal gold nanoparticles confined in an optical potential well. *Nano Letters* 11, 4505–4508 (2011).

50. Okamoto, K. & Kawata, S. Radiation Force Exerted on Subwavelength Particles near a Nanoaperture. *Physical Review Letters* 83, 4534 (1999).

51. Shao, L., Yang, Z. J., Andrén, D., Johansson, P. & Käll, M. Gold Nanorod Rotary Motors Driven by Resonant Light Scattering. *ACS Nano* 9, 12542–12551 (2015).

52. Nakayama, Y. *et al.* Tunable nanowire nonlinear optical probe. *Nature* 447, 1098–101 (2007).

53. Ploschner, M., Čižmár, T., Mazilu, M., Di Falco, A. & Dholakia, K. Bidirectional optical sorting of gold nanoparticles. *Nano Letters* 12, 1923–1927 (2012).

54. Wheaton, S., Gelfand, R. M. & Gordon, R. Probing the Raman-active acoustic vibrations of nanoparticles with extraordinary spectral resolution. *Nature Photonics* 9, 68–72 (2015).

55. Al Balushi, A. A. & Gordon, R. A label-free untethered approach to single-molecule protein binding kinetics. *Nano Letters* 14, 5787–5791 (2014).

56. Agarwal, R. *et al.* Manipulation and assembly of nanowires with holographic optical traps. *Optics express* 13, 8906–8912 (2005).

57. Pauzauskie, P. J., Jamshidi, A., Valley, J. K., Satcher, J. H. & Wu, M. C. Parallel trapping of multiwalled carbon nanotubes with optoelectronic tweezers. *Applied Physics Letters* 95, (2009).

58. Stratton, J. A. *Electromagnetic Theory*. *Library* 14, (1941).

59. Kerker, M. *The Scattering of Light and Other Electromagnetic Radiation*. *Chap* 7, (1969).

60. Ashkin, a, Dziedzic, J. M., Bjorkholm, J. E. & Chu, S. Observation of a single-beam gradient force optical trap for dielectric particles. *Optics letters* 11, 288 (1986).

61. Harada, Y. & Asakura, T. Radiation forces on a dielectric sphere in the Rayleigh scattering regime. *Optics Communications* 124, 529–541 (1996).

62. Gordon, J. P. Radiation Forces and Momenta in Dielectric Media. *Physical Review A* 8, 14–21 (1973).

63. Griffiths, D. & College, R. *Introduction to electrodynamics*. *Zhurnal Eksperimental'noi i Teoreticheskoi Fiziki* (1999).

64. Kik, P. G. & Brongersma, M. L. Surface plasmon nanophotonics. *Springer Series in Optical Sciences* 131, 1–9 (2007).

65. Garnett, J. C. M. Colours in Metal Glasses, in Metallic Films, and in Metallic Solutions. II. *Philosophical Transactions of the Royal Society A: Mathematical, Physical and Engineering Sciences* 205, 237–288 (1906).

66. Ritchie, R. H., Arakawa, E. T., Cowan, J. J. & Hamm, R. N. Surface-plasmon resonance effect in grating diffraction. *Physical Review Letters* 21, 1530–1533 (1968).

67. Kreibig, U. & Zacharias, P. Surface plasma resonances in small spherical silver and gold particles. *Zeitschrift für Physik* 231, 128–143 (1970).

68. Otto, A. Excitation of nonradiative surface plasma waves in silver by the method of frustrated total reflection. *Zeitschrift für Physik* 216, 398–410 (1968).

69. Kretschmann, E. & Raether, H. Radiative decay of non-radiative surface plasmons excited by light. *Z. Naturforsch.* 23, 2135–2136 (1968).

70. Cunningham, S. L., Maradudin, A. A. & Wallis, R. F. Effect of a charge layer on the surface-plasmon-polariton dispersion curve. *Physical Review B* 10, 3342–3355 (1974).

71. Vaughan, A. Raman nanotechnology - The lycurgus cup. *IEEE Electrical Insulation Magazine* 24, 4 (2008).

72. Maier, S. a *et al.* Observation of coupled plasmon-polariton modes of plasmon waveguides for electromagnetic energy transport below the diffraction limit. *Proceedings of SPIE* 4810, 71–81 (2002).

73. Su, K. H. *et al.* Interparticle coupling effects on plasmon resonances of nanogold particles. *Nano Letters* 3, 1087–1090 (2003).

74. Lehmuskero, A., Ogier, R., Gschneidtner, T., Johansson, P. & Käll, M. Ultrafast spinning of gold nanoparticles in water using circularly polarized light. *Nano Lett.* 13, 3129–3134 (2013).

75. Maxwell, J. C. A Dynamical Theory of the Electromagnetic Field. *Philosophical Transactions of the Royal Society of London* 155, 459–512 (1865).

76. Poynting, J. H. On the Transfer of Energy in the Electromagnetic Field. *Philosophical Transactions of the Royal Society of London* 175, 343–361 (1884).

77. Nichols, E. F. & Hull, G. F. A preliminary communication on the pressure of heat and light radiation. *Physical Review (Series I)* 13, 307–320 (1901).

78. Lebedev, P. N. Untersuchungen uber die Druckkrafte des Lichtes. *Annalen der Physik* 6, 433 (1901).

79. Maragò, O. M., Jones, P. H., Gucciardi, P. G., Volpe, G. & Ferrari, A. C. Optical trapping and manipulation of nanostructures. *Nature nanotechnology* 8, 807–19 (2013).

80. Ashkin, A. History of optical trapping and manipulation of small-neutral particle, atoms, and molecules. *IEEE Journal on Selected Topics in Quantum Electronics* 6, 841–856 (2000).

81. Ashkin, A. & Dziedzic, J. M. Observation of radiation-pressure trapping of particles by alternating light beams. *Physical Review Letters* 54, 1245–1248 (1985).

82. Ashkin, A. & Dziedzic, J. M. Observation of optical resonances of dielectric spheres by light scattering. *Applied optics* 20, 1803–1814 (1981).

83. Dholakia, K., Reece, P. & Gu, M. Optical micromanipulation. *Chem. Soc. Rev.* 37,

42–55 (2008).

84. Twombly, C. W., Evans, J. S. & Smalyukh, I. I. Optical Manipulation of self-aligned graphene flakes in liquid crystals. *Optics Express* 21, 3998–4003 (2013).

85. Tong, L., Miljković, V. D. & Käll, M. Alignment, rotation, and spinning of single plasmonic nanoparticles and nanowires using polarization dependent optical forces. *Nano Letters* 10, 268–273 (2010).

86. Pauzauskie, P. J. *et al.* Optical trapping and integration of semiconductor nanowire assemblies in water. *Nature materials* 5, 97–101 (2006).

87. Kotnala, A., Wheaton, S. & Gordon, R. Playing the notes of DNA with light: extremely high frequency nanomechanical oscillations. *Nanoscale* 7, 2295–300 (2015).

88. Al Balushi, A. a *et al.* Label-Free Free-Solution Nanoaperture Optical Tweezers for Single Molecule Protein Studies. *The Analyst* 4760–4778 (2015).

89. Geiselmann, M. *et al.* 3D optical manipulation of a single electron spin. *ArXiv* 8, 1–16 (2012).

90. Wördemann, M. *Structured Light Fields - Applications in Optical Trapping, Manipulation, and Organization*. (2012).

91. Nieminen, T. A., Knöner, G., Heckenberg, N. R. & Rubinsztein-Dunlop, H. Physics of Optical Tweezers. *Methods in Cell Biology* 82, 207–236 (2007).

92. Bethe, H. A. Theory of diffraction by small holes. *Physical Review* 66, 163–182 (1944).

93. Jackson. Classical Electrodynamics 3rd edition.pdf. *American Journal of Physics* 67, 841 (1999).

94. Pozar, D. *Microwave Engineering Fourth Edition*. *Zhurnal Eksperimental'noi i Teoreticheskoi Fiziki* (2005).

95. Degiron, A., Lezec, H. J., Yamamoto, N. & Ebbesen, T. W. Optical transmission properties of a single subwavelength aperture in a real metal. *Optics Communications* 239, 61–66 (2004).

96. Blanco, L. A. & Nieto-Vesperinas, M. Optical forces near subwavelength apertures in metal discs. *Journal of Optics A: Pure and Applied Optics2* 9, 235–238 (2007).

97. Juan, M. L., Gordon, R., Pang, Y., Eftekhari, F. & Quidant, R. Self-induced back-action optical trapping of dielectric nanoparticles. *Nature Physics* 5, 915–919

(2009).

98. Neumeier, L., Quidant, R. & Chang, D. E. Self-induced back-action optical trapping in nanophotonic systems. *New Journal of Physics* 17, 123008 (2015).

99. Mestres, P., Berthelot, J. & Quidant, R. Unravelling the optomechanical nature of plasmonic trapping. *arXiv* 1–14 (2015).

100. Wang, K., Schonbrun, E., Steinvurzel, P. & Crozier, K. B. Trapping and rotating nanoparticles using a plasmonic nano-tweezer with an integrated heat sink. *Nature communications* 2, 469 (2011).

101. Wang, K. & Crozier, K. B. Plasmonic trapping with a gold nanopillar. *ChemPhysChem* 13, 2639–2648 (2012).

102. King, G. W. *Spectroscopy and Molecular Structure*. (Holt, Rinehart and Winston, 1964).

103. Eyring, H., Walter, J. & Kimball, G. E. *Quantum chemistry*. (Wiley, 1944).

104. Mandl, F. *Statistical physics*. (Wiley, 1971).

105. Kamino, T. *et al.* A newly developed FIB system for TEM specimen preparation. *Microscopy and Microanalysis* 8, 510–511 (2002).

106. Saleh, A. A. E. & Dionne, J. A. Toward efficient optical trapping of Sub-10-nm particles with coaxial plasmonic apertures. *Nano Letters* 12, 5581–5586 (2012).

107. Pang, Y. & Gordon, R. Optical trapping of a single protein. *Nano Letters* 12, 402–406 (2012).

108. Pang, Y. & Gordon, R. Optical trapping of 12 nm dielectric spheres using double-nanoholes in a gold film. *Nano Letters* 11, 3763–3767 (2011).

109. Kotnala, A. & Gordon, R. Double nanohole optical tweezers visualize protein p53 suppressing unzipping of single DNA-hairpins. *Biomedical optics express* 5, 1886–94 (2014).

110. Chen, C. *et al.* Enhanced optical trapping and arrangement of nano-objects in a plasmonic nanocavity. *Nano Letters* 12, 125–132 (2012).

111. Oh, Y. *et al.* Recent advances of nanostructure implemented spectroscopic sensors—A brief overview. *Applied Spectroscopy Reviews* 51, (2016).

112. Liu, N., Tang, M. L., Hentschel, M., Giessen, H. & Alivisatos, A. P. Nanoantenna-enhanced gas sensing in a single tailored nanofocus. *Nature Materials* 10, 631–636

(2011).

113. Tittl, A., Kremers, C., Dorfmüller, J., Chigrin, D. N. & Giessen, H. Spectral shifts in optical nanoantenna-enhanced hydrogen sensors. *Optical Materials Express* 2, 111 (2012).

114. Li, B.-B. *et al.* Single nanoparticle detection using split-mode microcavity Raman lasers. *Proceedings of the National Academy of Sciences of the United States of America* 111, 14657–62 (2014).

115. Shopova, S. I., Rajmangal, R., Holler, S. & Arnold, S. Plasmonic enhancement of a whispering-gallery-mode biosensor for single nanoparticle detection. *Applied Physics Letters* 98, (2011).

116. Zijlstra, P. & Orrit, M. Single metal nanoparticles: optical detection, spectroscopy and applications. *Reports on Progress in Physics* 74, 106401 (2011).

117. Slaughter, L. S. *et al.* Plasmonic polymers unraveled through single particle spectroscopy. *Nanoscale* 6, 11451–11461 (2014).

118. Ajito, K. & Torimitsu, K. Single nanoparticle trapping using a Raman tweezers microscope. *Applied Spectroscopy* 56, 541–544 (2002).

119. Kerman, S. *et al.* Raman Spectroscopy and Optical Trapping of 20 nm Polystyrene Particles in Plasmonic Nanopores. in *Nanophotonics V* (2014).

120. Kerman, S. *et al.* Raman Fingerprinting of Single Dielectric Nanoparticles in Plasmonic Nanopores. *Nanoscale* 7, 18612–18618 (2015).

121. Jones, S., Al Balushi, A. A. & Gordon, R. Raman spectroscopy of single nanoparticles in a double-nanohole optical tweezer system. *Journal of Optics* 17, (2015).

122. Balachandran, U. & Eror, N. G. Raman spectra of titanium dioxide. *Journal of Solid State Chemistry* 42, 276–282 (1982).

123. Anema, J. R., Brolo, A. G., Felten, A. & Bittencourt, C. Surface-enhanced Raman scattering from polystyrene on gold clusters. *Journal of Raman Spectroscopy* 41, 745–751 (2010).

124. Vasquez, G. *et al.* Influence of Fe and Al doping on the stabilization of the anatase phase in TiO2 nanoparticles. *Journal of Materials Chemistry C* 2, 10377–10385 (2014).

125. Asiala, S. M. & Schultz, Z. D. Label-free in situ detection of individual macromolecular assemblies by surface enhanced Raman scattering. *Chemical*

*communications (Cambridge, England)* 49, 4340–2 (2013).

126. Asiala, S. M. & Schultz, Z. D. Surface enhanced Raman correlation spectroscopy of particles in solution. *Analytical Chemistry* 86, 2625–2632 (2014).

127. Zehtabi-Oskuie, A. *et al.* Double nanohole optical trapping: dynamics and protein-antibody co-trapping. *Lab Chip* 13, 2563–8 (2013).

128. Al Balushi, A. a, Zehtabi-Oskuie, A. & Gordon, R. Observing single protein binding by optical transmission through a double nanohole aperture in a metal film. *Biomedical optics express* 4, 1504–11 (2013).

129. Kotnala, A., DePaoli, D. & Gordon, R. Sensing nanoparticles using a double nanohole optical trap. *Lab Chip* 13, 4142–6 (2013).

130. http://www.lumerical.com/tcad-products/fdtd/. Limerical Solutions, Inc.

131. Haitian, X., Jones, S., Choi, B.-C. & Gordon, R. Characterization of Individual Magnetic Nanoparticles in Solution by Double Nanohole Optical Tweezers. *Nano Letters* 16, 2639–2643 (2016).

132. Neuman, K. C. & Block, S. M. Optical trapping. *Rev Sci Instrum* 75, 2787–2809 (2004).

133. Schlegel, A., Alvarado, S. F. & Wachter, P. Optical properties of magnetite (Fe3O4). *Journal of Physics C: Solid …* 12, 1157 (1979).

134. Levitin, E. Y., Kokodiy, N. G., Timajuk, V. A., Vedernikova, I. O. & Chan, T. M. Measurements of the Size and Refractive Index of Fe3O4 Nanoparticles. *Inorganic Materials* 50, 817–820 (2014).

135. Dholakia, K. & Čižmár, T. Shaping the future of manipulation. *Nat. Photon.* 5, 335–342 (2011).

136. Kotnala, A. & Gordon, R. Quantification of high-efficiency trapping of nanoparticles in a double nanohole optical tweezer. *Nano Letters* 14, 853–856 (2014).

137. Reif, F. *Fundamentals of statistical and thermal physics*. (Waveland Oress, 1965).

138. Neuman, K. C. & Nagy, A. Single-molecule force spectroscopy: optical tweezers, magnetic tweezers and atomic force microscopy. *Nature methods* 5, 491–505 (2008).

139. Shevkoplyas, S. S., Siegel, A. C., Westervelt, R. M., Prentiss, M. G. & Whitesides, G. M. The force acting on a superparamagnetic bead due to an applied magnetic

field. *Lab on a chip* 7, 1294–1302 (2007).

140. Liu, Z. L. *et al.* Synthesis and Magnetic Properties of Fe3O4 Nanoparticles. *Journal of Material Synthesis adn Processing* 10, 83–87 (2002).

141. Zhao, D. L., Zeng, X. W., Xia, Q. S. & Tang, J. T. Preparation and coercivity and saturation magnetization dependence of inductive heating property of Fe3O4 nanoparticles in an alternating current magnetic field for localized hyperthermia. *Journal of Alloys and Compounds* 469, 215–218 (2009).

142. Sun, J. *et al.* Synthesis and characterization of biocompatible Fe3O4 nanoparticles. *Journal of Biomedical Materials Research - Part A* 80, 333–341 (2007).

143. Liberale, C. *et al.* Miniaturized all-fibre probe for three-dimensional optical trapping and manipulation. *Nature Photonics* 1, 723–727 (2007).

144. Liu, Z., Guo, C., Yang, J. & Yuan, L. Tapered fiber optical tweezers for microscopic particle trapping: fabrication and application. *Optics express* 14, 12510–12516 (2006).

145. Xin, H., Li, Y., Li, L., Xu, R. & Li, B. Optofluidic manipulation of Escherichia coli in a microfluidic channel using an abruptly tapered optical fiber. *Applied Physics Letters* 103, (2013).

146. El Eter, A. *et al.* Fiber-integrated optical nano-tweezer based on a bowtie-aperture nano-antenna at the apex of a SNOM tip. *Optics Express* 22, 10072 (2014).

147. Gelfand, R. M., Wheaton, S. & Gordon, R. Cleaved fiber optic double nanohole optical tweezers for trapping nanoparticles. *Optics letters* 39, 6415–6417 (2014).

148. Beiser, A. *Concepts of Modern Physics*. (McGraw-Hill, 1963).

149. Sellmyer, D. & Skomski, R. *Advanced magnetic nanostructures*. *Advanced Magnetic Nanostructures* (2006).

150. Jiles, D. *Introduction to Magnetism and Magnetic Materials*. *Solid State Physics* 1, (1991).

151. Foner, S. Versatile and sensitive vibrating-sample magnetometer. *Review of Scientific Instruments* 30, 548–557 (1959).

# Appendix

## Appendix A – Quantum Harmonic Oscillator

The harmonic oscillator potential well is a useful and commonly made approximation in physics. This approximation is typically valid for small perturbations from equilibrium where the restoring force is approximately linear. In Section "2.5 Raman Spectroscopy" of this thesis, it was stated that for a diatomic molecule, the potential well for vibrational motion is given by a Morse potential as shown in Figure 13. For low energy states within the Morse potential, the shape of the potential well is approximately quadratic ($U \sim x^2$) and therefore solutions to the quantum harmonic oscillator are in good agreement with the quantum mechanical low-energy vibrational states of a diatomic molecule. Provided here is a brief derivation illustrating how the wavefunction, and energy states can be determined for this system. For a broader range of quantum mechanical potential wells refer to[148].

To start, recall that in the harmonic potential approximation, the restorative force must have the following form:

$$F = -kx$$

The potential of this system can therefore be defined as:

$$U(x) = -\int_0^x F(x')dx' = k\int_0^x x'dx' = \frac{1}{2}kx^2$$

In order to determine the quantum mechanical representation of this system, the Schrödinger equation must be solved with the quadratic potential defined above.

$$\frac{d^2\psi}{dx^2} + \frac{2m}{\hbar^2}\left(E - \frac{1}{2}kx^2\right)\psi = 0$$

For convenience, the following simplifications are made which simplify the algebra in later steps:

$$\text{let} \quad y = \left(\frac{1}{\hbar}\sqrt{km}\right)^{1/2} x = \sqrt{\frac{\omega m}{\hbar}}\, x$$

$$\text{and} \quad \alpha = \frac{2E}{\hbar\omega}$$

The above simplifications effectively replace $x$, and $E$ with dimensionless parameters $y$, and $\alpha$. The value $\omega$ is the characteristic frequency of the system which can be classically obtained as $\omega = \sqrt{k/m}$. The Schrödinger equation can thus be simplified to:

$$\frac{d^2\psi}{dy^2} + (\alpha - y^2)\psi = 0$$

From the above equation, it can bee seen that the second derivative of the wave function must produce a term proportional to $y^2$, using this knowledge the following ansatz for the form of the waveform is taken

$$\psi = \mathrm{e}^{-\frac{y^2}{2}} f(y)$$

Substituting this into the simplified Schrödinger equation results in a differential equation that defines $f(y)$.

$$\frac{d^2 f}{dy^2} - 2y\frac{df}{dy} + (\alpha - 1)f = 0$$

To solve for $f(y)$, a series solution is attempted where $f$ has the following form:

$$\text{let} \quad f(y) = \sum_{v=0}^{\infty} a_v y^v$$

$$\therefore \quad f'(y) = \sum_{v=0}^{\infty} v a_v y^{v-1}$$

$$f''(y) = \sum_{v=0}^{\infty} v(v-1)a_v y^{v-2} = \sum_{v=0}^{\infty} (v+2)(v+1)a_{v+2} y^v$$

After inserting the series solution form of $f(y)$ into the defining differential equation, the following recursion relation can be obtained:

$$a_{v+2} = \frac{2v+1-\alpha}{(v+1)(v+2)} a_v$$

Therefore, the wavefunction can be written as $\psi = \mathrm{e}^{-y^2/2} \sum_{v=0}^{\infty} a_v y^v$ where $a_v$ is defined by the above recursion relation. Analysis of this form of the wavefunction indicates that in general, the function is divergent and therefore not normalizable. In order for the wave function to describe a real system, it must go to zero at infinity. Under this constraint, the function $f(y)$ cannot have an infinite number of terms, and there must be some value of $v$ such that $a_{v+2} = 0$, *i.e.*

$$2v + 1 - \alpha = 0$$

$$\alpha = \frac{2E}{\hbar\omega} = 2v + 1$$

$$E = \hbar\omega\left(v + \frac{1}{2}\right)$$

Shown above if the restriction of energy levels that can be obtained in this system, and correspond to energy eigenstates as defined by the Schrödinger equation. The explicit form of the wavefunction for this system is nontrivial to derive, but has been intensely studied over the years. The well known solution to the waveform is:

$$\psi_v = \left(\frac{2m\omega}{h}\right)^{\frac{1}{4}} \frac{1}{\sqrt{2^v v!}} H_v(y) \mathrm{e}^{-y^2/2}$$

The term $H_v(y)$ is known as a Hermite polynomial. Hermite polynomials are well known class of orthogonal polynomials that can be defined according to:

$$H_v(y) = (-1)^v \mathrm{e}^{y^2} \frac{d^v \mathrm{e}^{-x^2}}{dx^v}$$

The wavefunctions for the lowest six energy states of a quantum harmonic oscillator are shown in Figure 32 and the corresponding probability distributions are given in Figure 33.

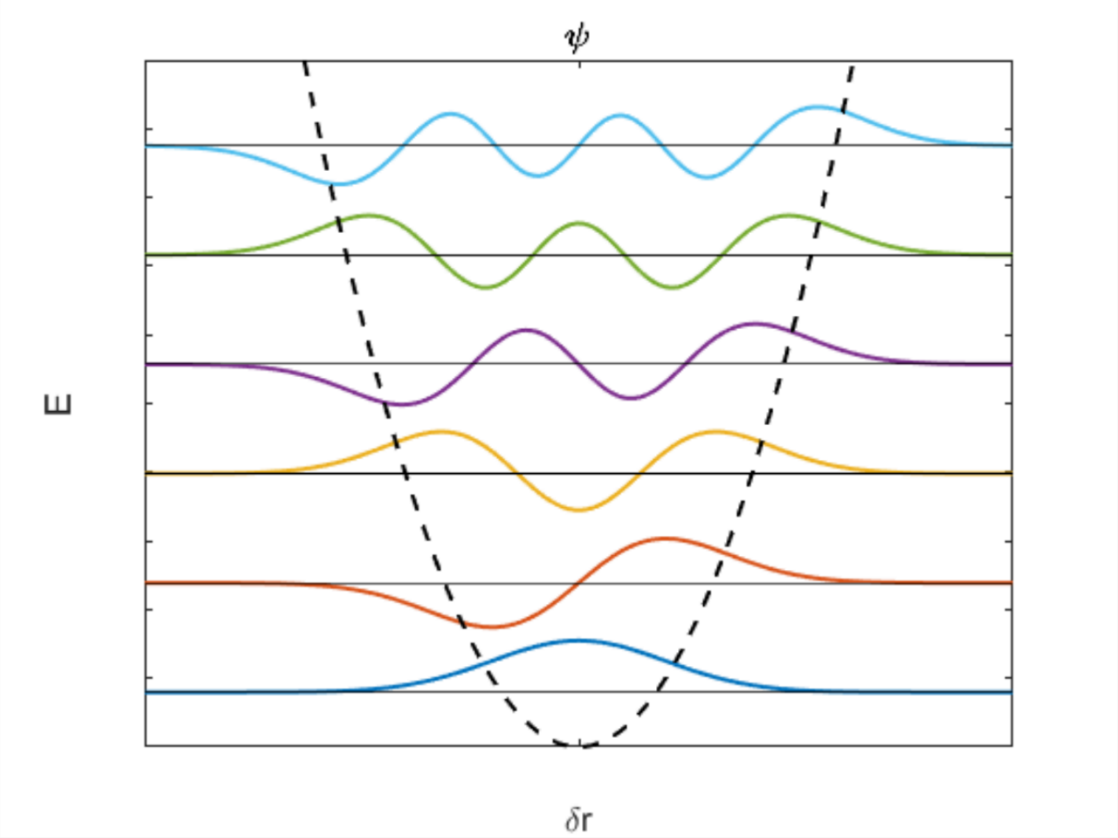

**Figure 32** – Wavefunctions of quantum harmonic oscillator corresponding to the lowest 6 energy states. The dashed black line indicates the potential well.

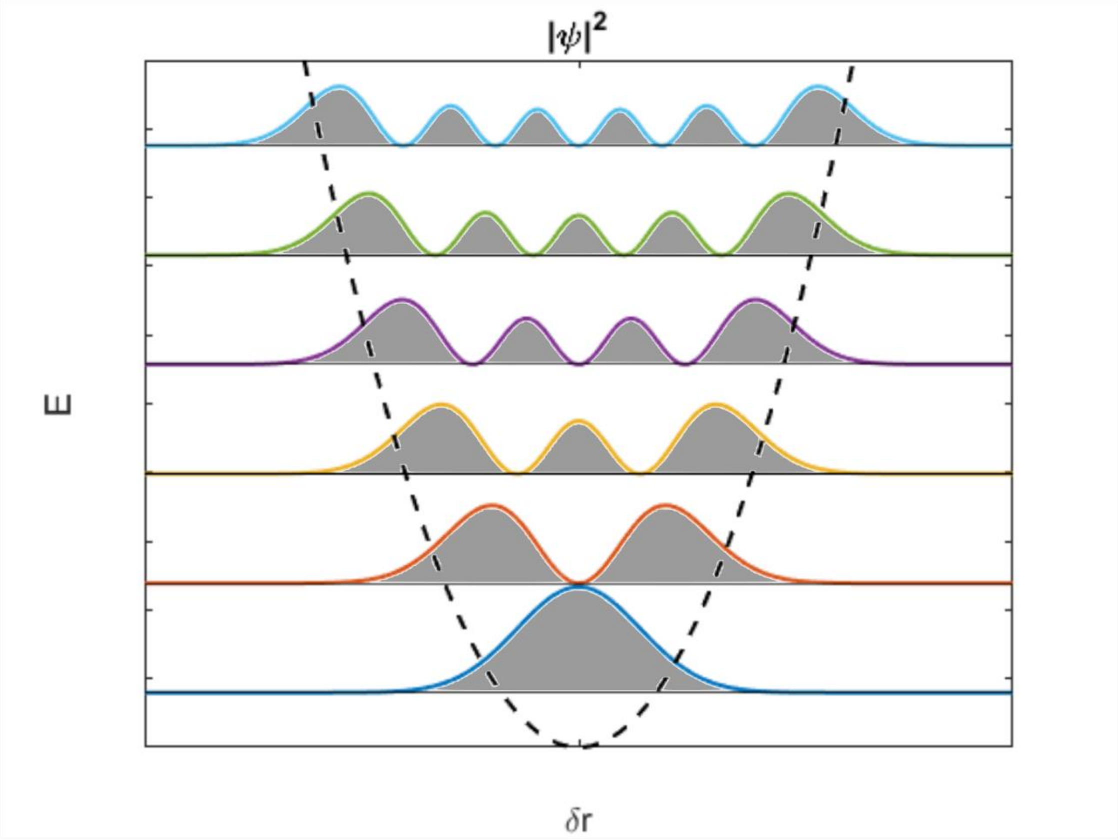

**Figure 33** – Probability distributions of the vibrational states in a quadratic potential well as defined by the wavefunction.

## Appendix B – Fabrication of DNH at Different FIB Magnifications

Provided here are several scanning electron microscope images showing the effect of focused ion beam milling at different imaging magnifications. The apertures presented here were all milled into the same sample of 100 nm thick gold deposited on a 5 nm titanium substrate overtop of a glass coverslide. The focused ion beam used gallium ions accelerated at 40 kV and a beam limiting aperture of 5 μm to mill into the gold. For all apertures shown here the aperture design parameters (Figure 34) were kept constant and the same beam alignment was used. The dwell time at each pixel was set to ten microseconds, and the number of passes was 35.

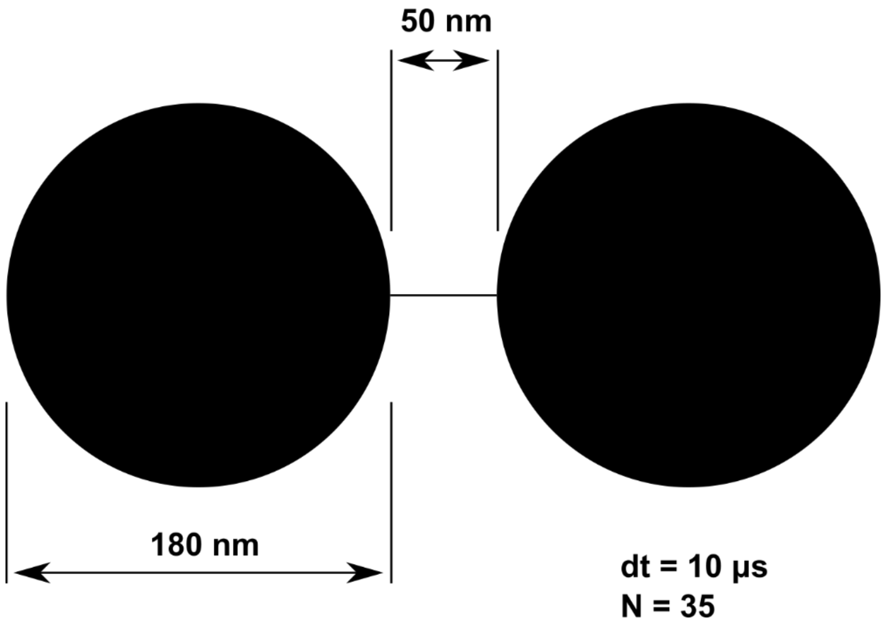

**Figure 34 –** Typical double nanohole fabrication parameters. The black regions indicate the area that is exposed to the focused ion beam. The dwell time (dt) and number of passes (N) are 10 μs and 35 respectively. A 1-pixel × 50 nm line is drawn between the adjacent spheres to connect them.

The SEM images shown in Figure 35 - Figure 39 are for beam magnifications of 20 000, 40 000, 60 000, 80 000, and 100 000 time respectively. The aperture design parameters are not optimized for all fabrication magnifications. The interesting result shown here is that as the FIB beam magnification in increased, the slope of the aperture also increases. This observation indicates that the fabrication magnification has a significant affect on the z-profile of the trapping aperture. Research is currently being conducted into the effect that the z-profile of an aperture has on trapping. Initial FDTD simulations indicate that the z-profile has a pronounced effect on the resonance of the aperture which in turn determines the sensitivity of the aperture to a trapped particle.

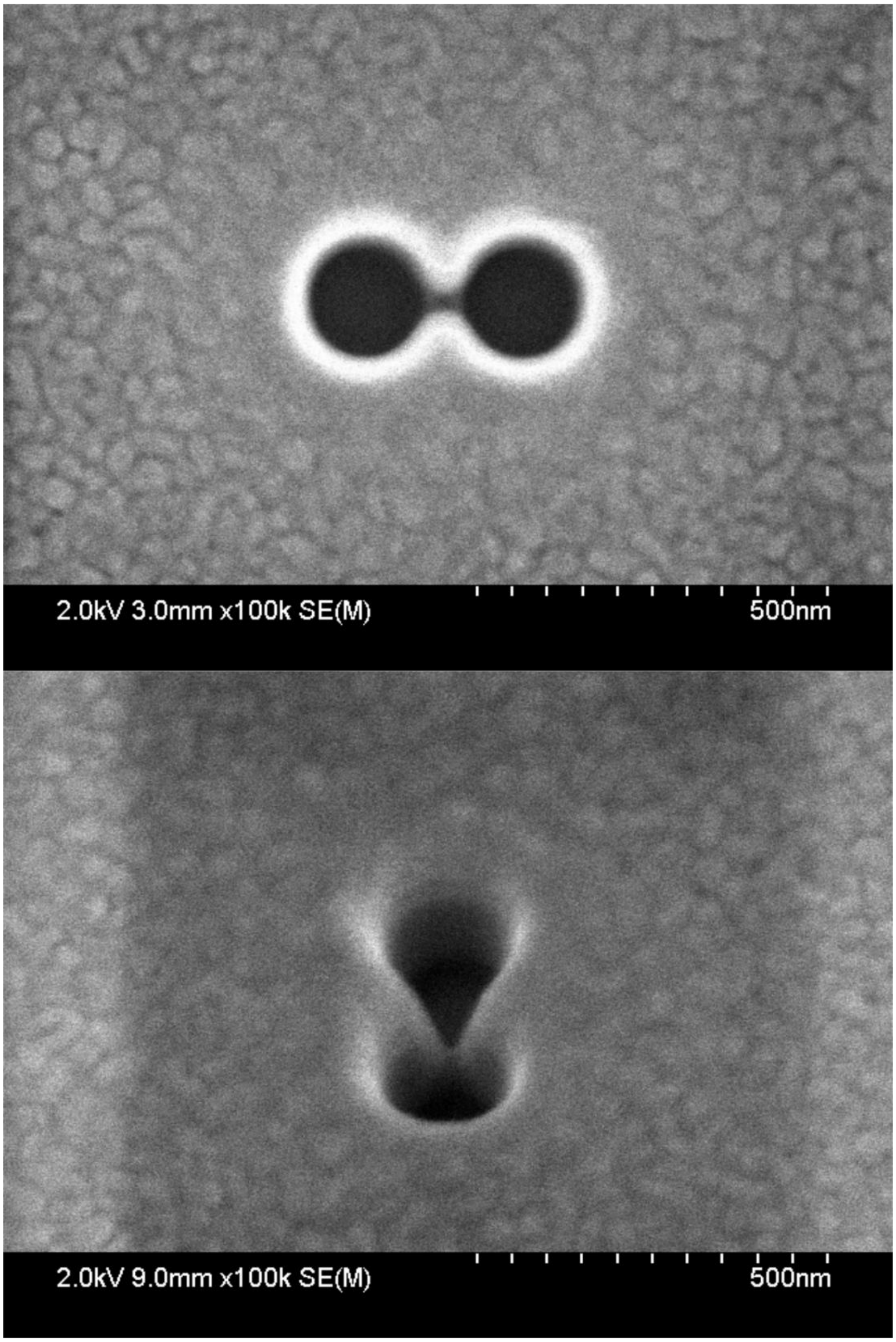

**Figure 35 –** Double nanohole aperture fabricated with focused ion beam at 20 000 times magnification. Top: SEM image of DNH, imaging plane is perpendicular to surface normal. Bottom: tilted image of same aperture, imaging plant is tilted 30° to surface normal.

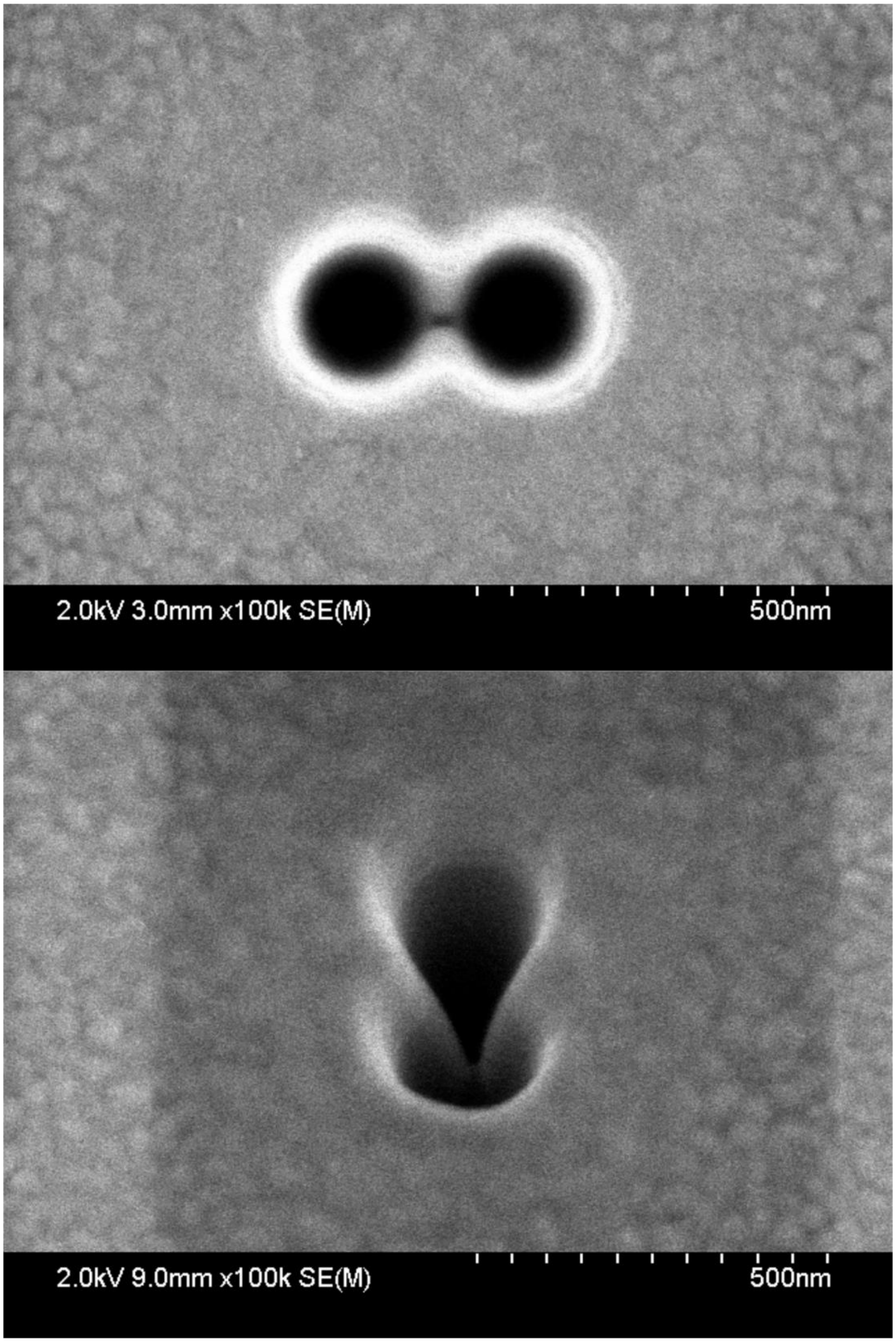

**Figure 36 –** Double nanohole aperture fabricated with focused ion beam at 40 000 times magnification. Top: SEM image of DNH, imaging plane is perpendicular to surface normal. Bottom: tilted image of same aperture, imaging plant is tilted 30° to surface normal.

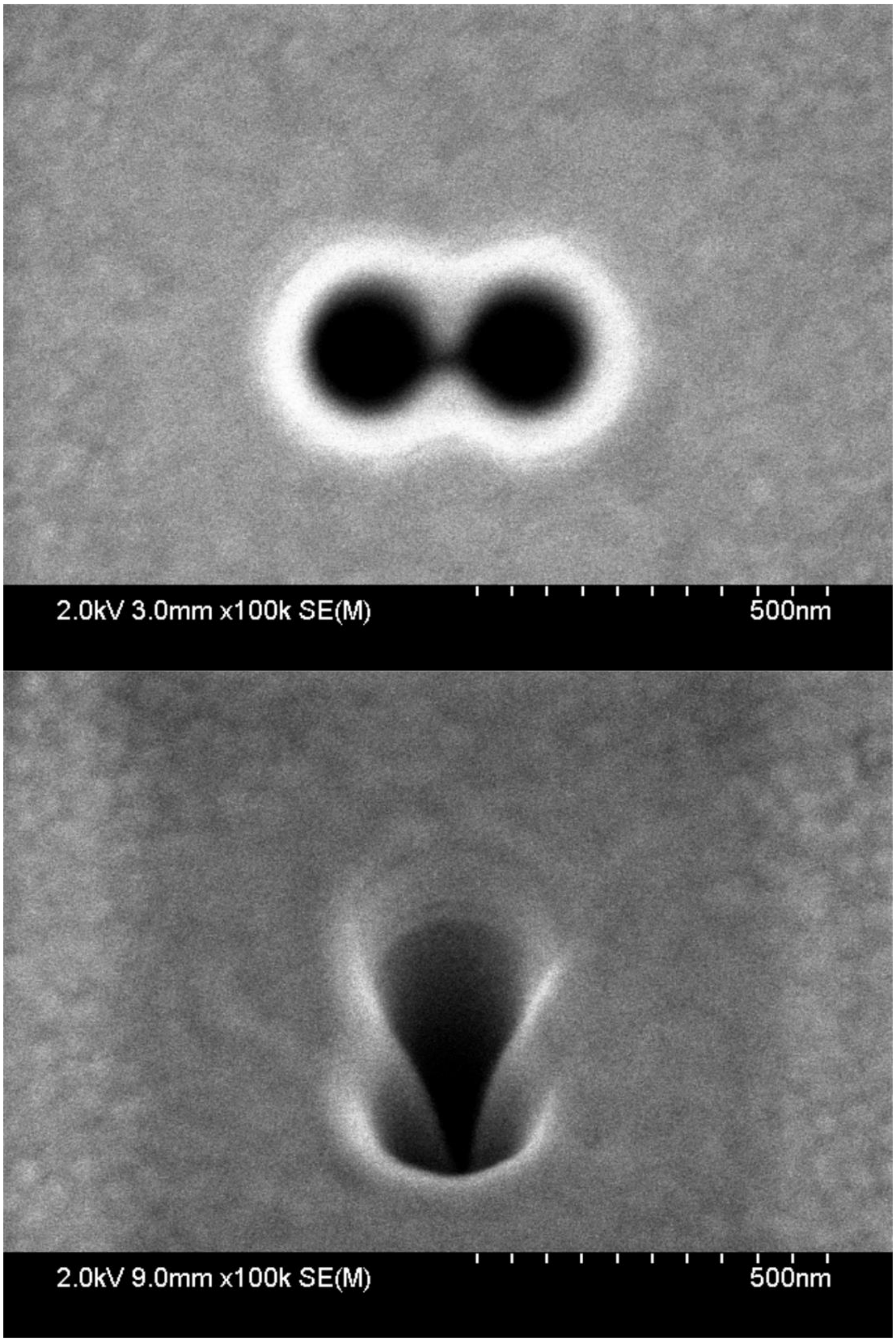

**Figure 37 –** Double nanohole aperture fabricated with focused ion beam at 60 000 times magnification. Top: SEM image of DNH, imaging plane is perpendicular to surface normal. Bottom: tilted image of same aperture, imaging plant is tilted 30° to surface normal.

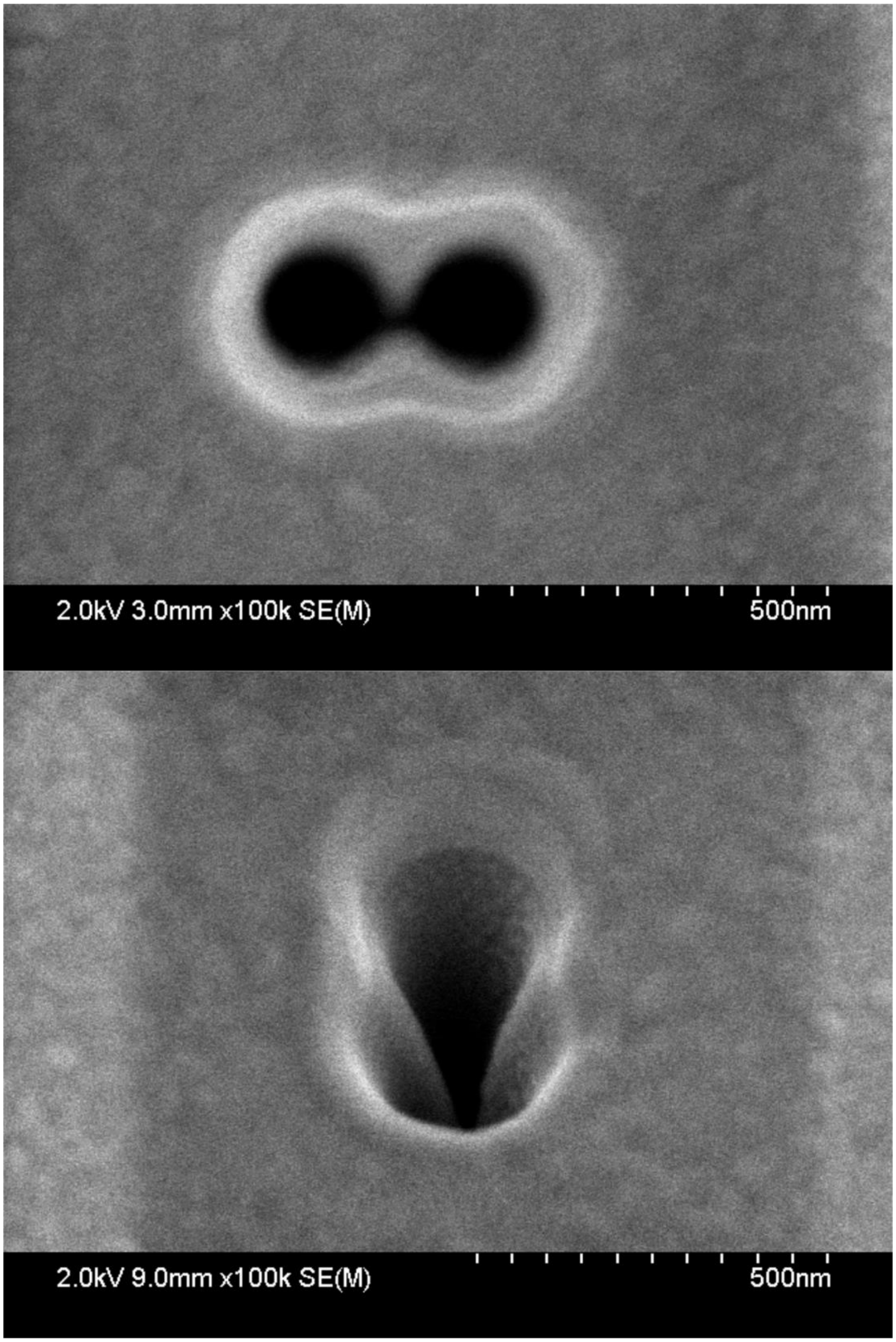

**Figure 38 –** Double nanohole aperture fabricated with focused ion beam at 80 000 times magnification. Top: SEM image of DNH, imaging plane is perpendicular to surface normal. Bottom: tilted image of same aperture, imaging plant is tilted 30° to surface normal.

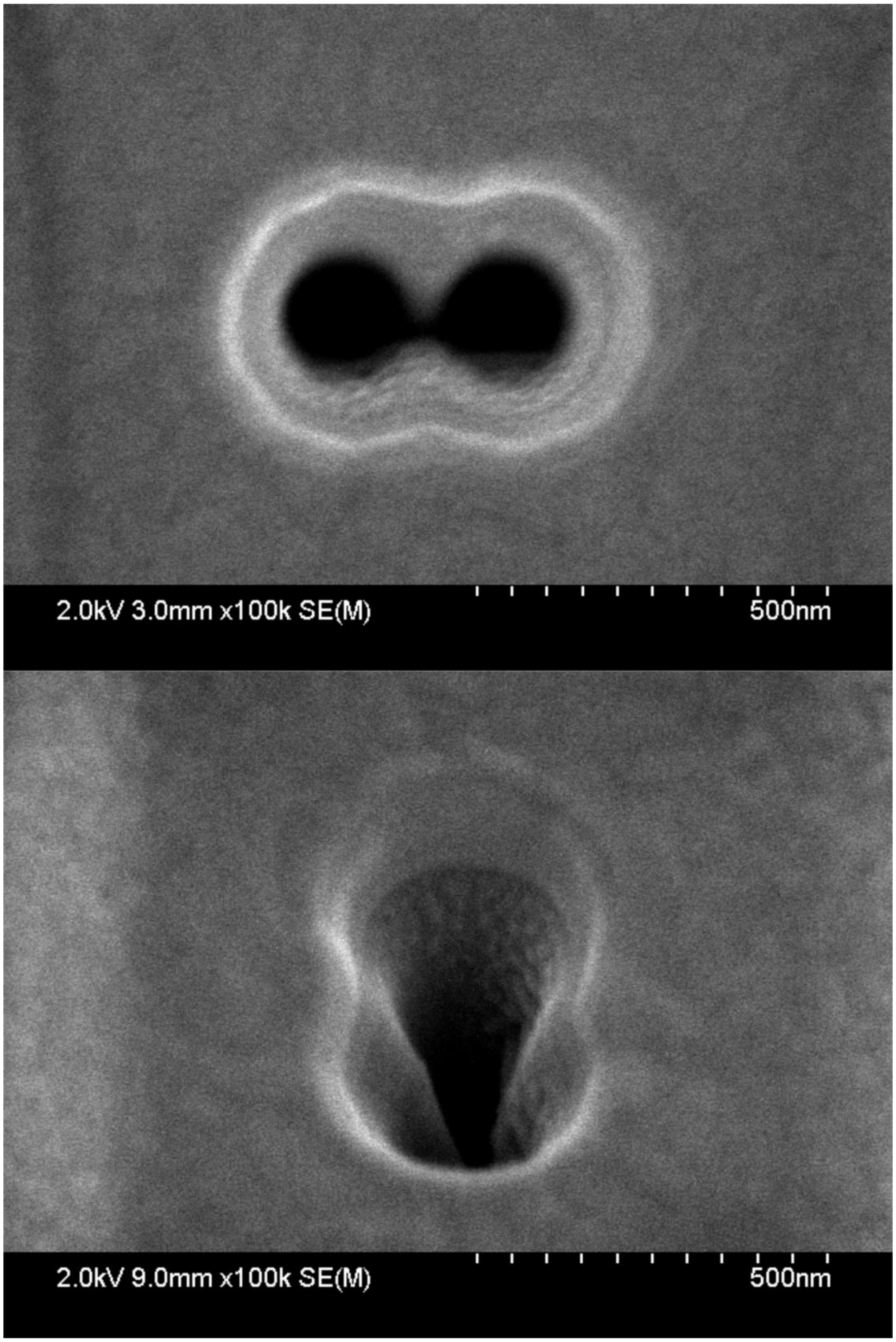

**Figure 39 –** Double nanohole aperture fabricated with focused ion beam at 100 000 times magnification. Top: SEM image of DNH, imaging plane is perpendicular to surface normal. Bottom: tilted image of same aperture, imaging plant is tilted 30° to surface normal.

# Appendix C – C-shaped Trapping Aperture

In addition to the dual nanohole aperture, other trapping apertures have been investigated. One such aperture is the C-shaped aperture. The basic design of this aperture is shown in Figure 40 and electron microscope images are given in Figure 41. These apertures were thought to show promise due to the potential for smaller minimum feature sizes, and a higher degree of flexibility in the design. The transmittance characteristics for such apertures are shown for Figure 42. For the case of parallel polarization, the transmittance curves indicate that at the trapping wavelength of 853 nm, the laser line with respect to the cut off wavelength is such that upon trapping the dielectric loading of the aperture would cause an increase in transmission. Trapping events were observed for the C-shaped aperture and were comparable to those observed with the DNH. Because of the increased complexity of the design, fabrication was less reliable, and therefore the C-shaped aperture was taken to be less advantageous than the DNH.

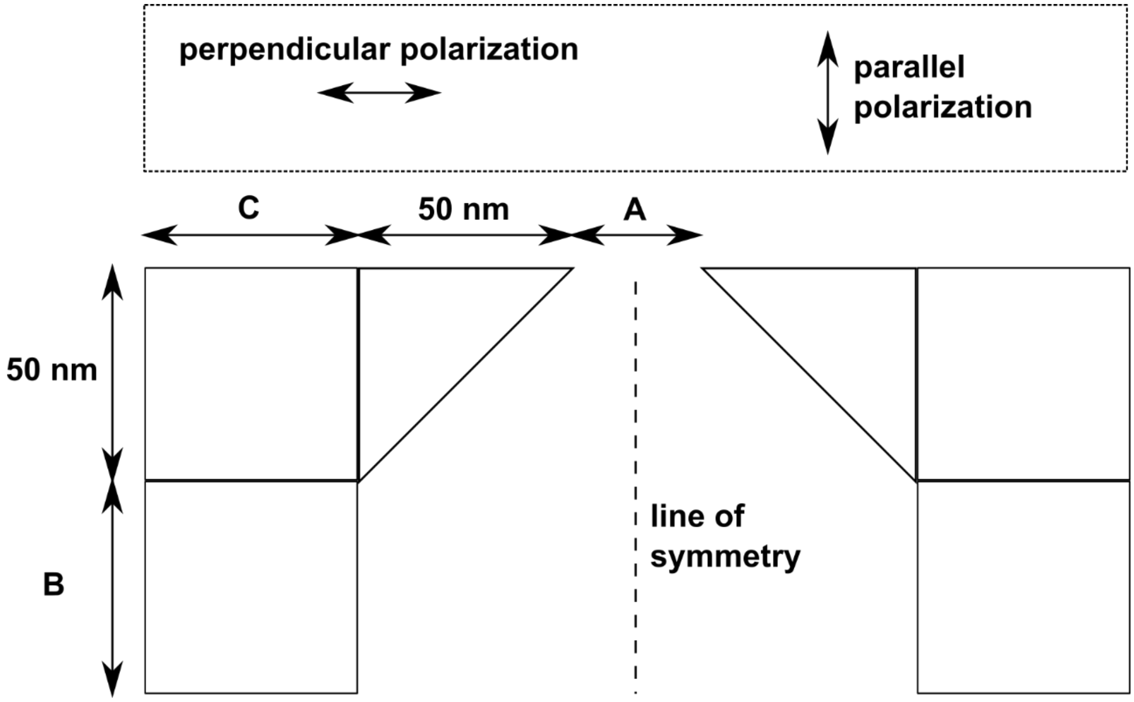

**Figure 40** – Design parameters for C-shaped trapping aperture.

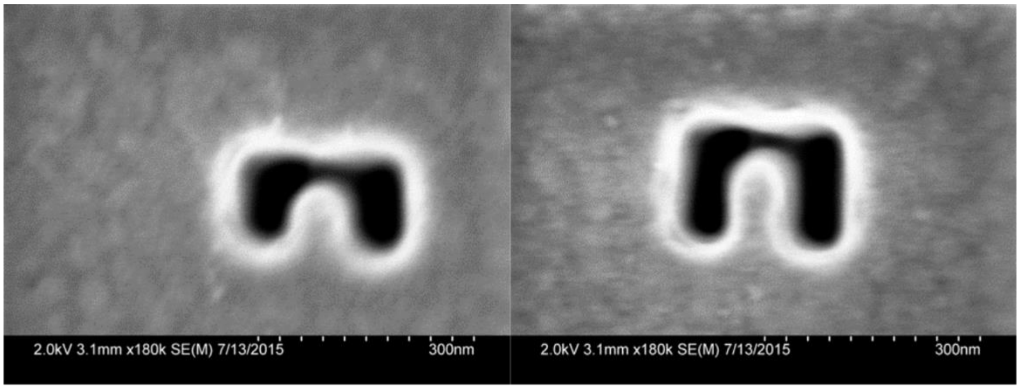

**A = 10 nm**
**B = 50 nm**
**C = 50 nm**

**A = 10 nm**
**B = 100 nm**
**C = 50 nm**

**Figure 41** – Scanning electron microscope images of C-shaped trapping apertures. The size parameters for each aperture are given below the figures and correspond to the parameters set in Figure 40. The FIB parameters are the same as those described in "Appendix B – Fabrication of DNH at Different FIB Magnifications" with a beam magnification of 80 000 times.

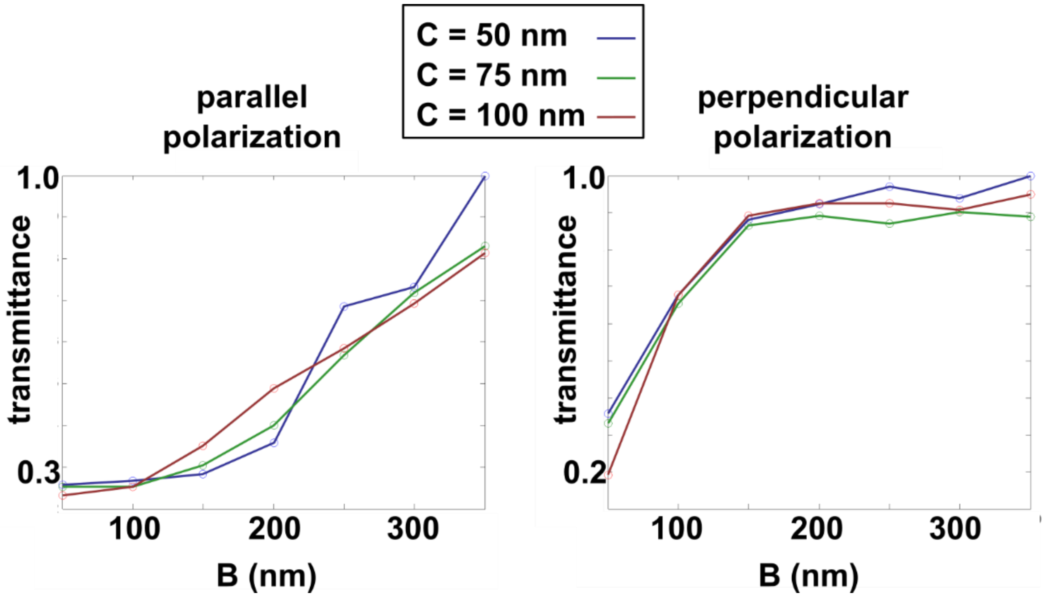

**Figure 42** – Normalized transmittance for parallel (left) and perpendicular (right) polarization, through a set of 21 C-shaped trapping apertures. Parameters A = 30 nm. Laser wavelength = 853 nm.

## Appendix D – Magnetic Nanoparticles

For large ferromagnetic objects, the material consists of an abundance of magnetic domains that result from the material structure arranging itself to minimize the magnetostatic energy of the material. As the size of a ferromagnetic object is reduced to the size scale of an individual magnetic domain, an interesting phenomena known as superparamagnetic emerges. Superparamagnetism is the situation where a magnetic particle consists of only a single magnetic domain; as a result, there is a reduced inclination for the magnetic domain to remain in its current orientation, as thermal forces or external fields can cause the alignment to easily switch due to the absence of other magnetic domains.

Figure 43 (left) illustrates the hysteresis curves for ferromagnetic, paramagnetic, and superparamagnetic particles. As the number of magnetic domains in a particle is reduced, this causes the coercivity of the object to diminish, approaching zero at the single domain limit. The relation between the coercivity of an object and the size is given qualitatively in Figure 43 (right). The transition to superparamagnetism typically occurs on the nanometer scale.

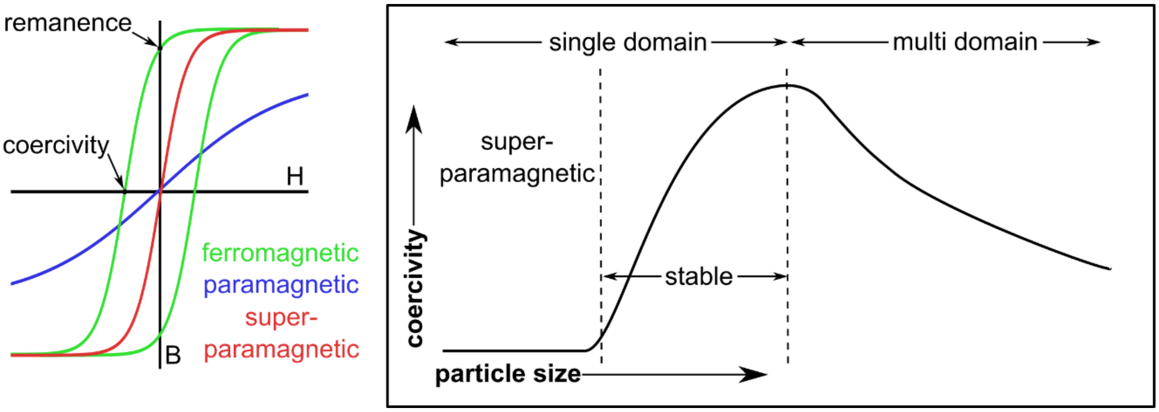

**Figure 43** – Left: diagram illustrating the magnetization of a material (B) due to an applied magnetic field (H) for ferromagnetic, paramagnetic, and superparamagnetic materials. Right: material property domains for ferromagnetic particles as the size dimension approaches 0.

The frequency at which a superparamagnetic particle changes its magnetic orientation in the absence of an external magnetic field is given by:

$$f_M = f_0 e^{-\frac{K_u V}{k_B T}}$$

In this equation $f_0$ is a material dependent proportionality constant, $K_u$ is the anisotropy energy density, and $V$ is the volume of the magnetic particle. The anisotropic energy density ($K_u$) is a measure of how much energy it takes to magnetize a material in a given direction. As the volume is reduced the energy associated with magnetization along a direction ($K_u V$) becomes comparable to the thermal energy ($k_B T$) and the rate at which the magnetic orientation of the particle changes increases. This process can be visualized as the magnetic state of a particle being in a double potential well as shown in Figure 44.

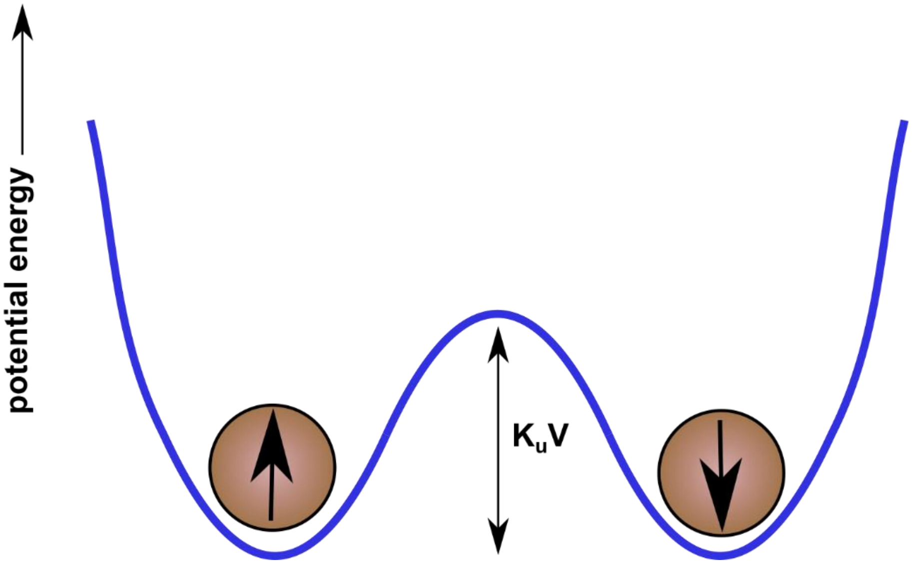

**Figure 44** – Double potential well of a superparamagnetic state[149].

## Appendix E – Vibrating Sample Magnetometry

A common and sensitive method for experimentally determining the magnetic properties of a substance is known as vibrating sample magnetometry (VSM)[150]. This method was first developed by Simon Foner, and published in 1959[151]. The basic concept for this design (shown in Figure 45), is that a magnetic sample is held within an externally applied magnetic field. The sample is then vibrated (typically simple harmonic motion). Currents due to the motion of the magnetic sample are formed in detector coils placed near the sample. The amplitude of these currents is proportional to the magnetic moment of the sample. In practice a lock-in amplifier is often used with the motion of the sample as a reference signal to remove noise from outside the setup.

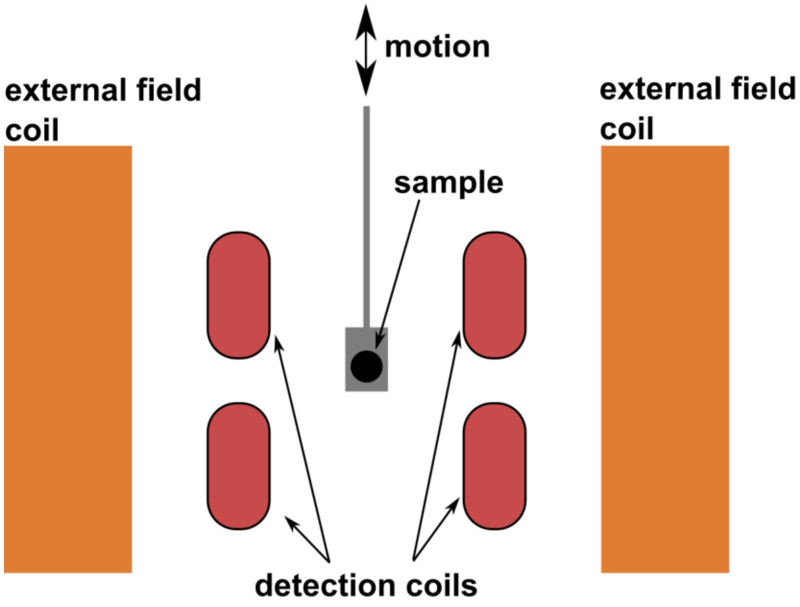

**Figure 45** – Vibrating sample magnetometer design. Sample is held in place within external magnetic field. Sample moves (vibrates) in sinusoidal fashion. The signal of vibrating sample is detected by coils and results in an AC current with amplitude proportional to the magnetic moment of the sample.